Engineering the Landau–Zener Tunneling of Ultracold Atoms in Tilted Potentials

Inaugural dissertation

by

Ghazal Tayebirad

Dissertation
submitted to the
Combined Faculties of the Natural Sciences and Mathematics
of the
Ruperto-Carola-University of Heidelberg, Germany
for the degree of
Doctor of Natural Sciences

Put forward by
Ghazal Tayebirad, M.Sc.
born in Ahvaz, Iran

Oral examination: 24 January 2011

Engineering the Landau–Zener Tunneling of Ultracold Atoms in Tilted Potentials

Referees: Dr. Sandro Wimberger
Prof. Dr. Ulrich Schwarz

Out of the cradle
onto dry land...
here it is standing...
atoms with consciousness
...matter with curiosity.
Stands at the sea...
wonders at wondering... I...
a universe of atoms...
an atom in the universe

Richard Feynmann

Abstract

A comprehensive study of the time-resolved Landau–Zener tunneling of a Bose–Einstein condensate in a tilted periodic potential is presented in this thesis. Several ways are discussed how to control the tunneling. In the first collection of our results, the tunneling from the ground band to the continuum is shown to depend crucially on the initial condition and system parameters, and also on the strength of atom-atom interactions. The use of different protocols enables us to access the tunneling probability in two different bases, namely, the adiabatic basis (eigenstates of the Hamiltonian with the potential) and the diabatic basis (free-particle momentum eigenstates). The structure of the survival probability and the measure of the tunneling time depend on the chosen basis. All these possibilities have been checked and proved in experiments. We go also beyond and propose a possibility to manipulate the tunneling probability of ultracold atoms in the tilted time-dependent stochastic potentials. Our theoretical and numerical results show that the tunneling in such a potential can be controlled by adding different types of colored noise. A scaling law is introduced for these results, which effectively reduces the parameter-dependence of the tunneling and leads to a better understanding of dynamics in the proposed noisy system.

Kurzzusammenfassung

In dieser Arbeit wird das zeitaufgelöste Landau-Zener-Tunneln eines Bose-Einstein-Kondensates in einem gekippten periodischen Potential umfassend studiert. Verschiedene Möglichkeiten das Tunneln zu kontrollieren werden diskutiert. Im ersten Teil unserer Ergebnisse zeigt sich, dass das Tunneln vom Grundband ins Kontinuum entscheidend von den Anfangsbedingungen, den Systemparametern und auch von der Stärke der Atom-Atom-Wechselwirkungen abhängt. Das Verwenden verschiedener Protokolle erlaubt uns auf die Tunnelwahrscheinlichkeit in zwei verschiedenen Basen zuzugreifen: zum einen in der adiabatischen Basis (Eigenzustände des Hamiltonoperators mit Potential) und zum andern in der diabatischen Basis (Impulseigenzustände der freien Teilchen). Die Struktur der Überlebenswahrscheinlichkeit und das Maß der Tunnelzeit hängen von der gewählten Basis ab. All diese Möglichkeiten sind in Experimenten überprüft und nachgewiesen worden. Darüber hinausgehend schlagen wir eine Möglichkeit vor, die Tunnelwahrscheinlichkeit ultrakalter Atome in gekippten zeitabhängig stochastischen Potentialen zu manipulieren. Unsere theoretischen und numerischen Ergebnisse zeigen, dass das Tunneln in solchen Potentialen durch das Hinzufügen verschiedener Arten farbigen Rauschens kontrolliert werden kann. Für diese Ergebnisse wird ein Skalierungsgesetz eingeführt, das die Parameterabhängigkeit des Tunnelns reduziert und zu einem besseren Verständnis der Dynamik in dem vorgeschlagenen rauschenden System führt.

Acknowledgment

It is a pleasure to thank those who made this thesis possible. First of all I owe my great gratitude to my supervisor Dr. Sandro Wimberger, whose supervision and support from the preliminary to the concluding level enabled me to develop an understanding of the subject. I thank him for introducing me to many researchers in the interesting field of ultracold atoms, especially for the great opportunity of collaboration with experimentalists in Pisa. I visited the department of physics in Pisa several times during the last three years, for that I am greatly thankful to Dr. Sandro Wimberger and the Heidelberg Graduate School of Fundamental Physics.

I am very grateful to Professor Riccardo Mannella in Pisa for his precious guidance in theoretical calculations concerning stochastic processes. I appreciate his patience to answer my many questions and his hospitality each time I visited him in Pisa during the last three year. It is an honor for me to acknowledge Professor Ennio Arimondo, who allowed a fruitful collaboration between us and his experimental group in Pisa. It was a great pleasure to collaborate with his group. Especially I would like to thank Dr. Oliver Morsch for his fruitful and motivating discussions, and also other members of the group who without their efforts this collaboration would not have been possible. I also thank Niels Lörch and Anton Ivanov for our rich collaborations within our group. Niels helped us with the Landau–Zener model and Anton in his bachelor thesis studied the interplay between interatomic interactions and noise.

I would like to thank Professor Ulrich Schwarz for being the second referee of my thesis. I also wish to express my gratitude to the Graduate School of Fundamental Physics in Heidelberg and in particular to Professor Sandra Klevansky and Gesine Heinzelmann for their kind supports and encouragements.

I am indebted to many of my colleagues and friends to support me in this work. I greatly thank Sean McConnell, Matthias Kronenwett, Dr. Remy Dubertrand, Benedikt Probst, Vera Spillner, Mohammad Siahatgar, Roman Hennig, David Lamb and Alexej Weber for proofreading parts of my thesis and for their helpful comments. Especially, I would like to show my gratitude to Patrick Plötz, my supportive colleague and friend for all his helps and comments.

I deeply thank my lovely and encouraging parents who gave me the moral support in all levels of my life. Especially for supporting me to come to Germany – far from home – to do my PhD. I am heartily grateful to them for the person I am today.

Ghazal Tayebirad

Heidelberg, November 20, 2010

Contents

1 Introduction **1**

2 Ultracold atoms and optical lattices **7**
2.1 Bose–Einstein condensation . . . 7
2.1.1 Non-interacting dilute Bose–gas . . . 8
2.1.2 Interacting Bose gas in the mean-field limit . . . 11
2.2 Optical lattices . . . 14
2.2.1 Connection to solid state physics . . . 14
2.2.2 Interaction of atoms and light . . . 14
2.2.3 Non-periodic optical lattices . . . 17
2.2.4 Tilted optical lattices . . . 21
2.3 Bloch oscillations . . . 23
2.4 Wannier–Stark problem . . . 25
2.4.1 Resonantly enhanced tunneling . . . 27
2.5 Tunneling in the presence of nonlinearity . . . 30

3 Models under consideration **33**
3.1 Landau–Zener model . . . 33
3.1.1 Transition times in the Landau-Zener model . . . 35
3.2 Noise algorithms . . . 40
3.2.1 Exponentially correlated noise . . . 41
3.2.2 Harmonic noise . . . 44
3.2.3 Deterministic phase . . . 48
3.2.4 Averaging and ensembles . . . 50

4 Numerical methods **53**
4.1 Implicit integration scheme in one-dimension . . . 53
4.1.1 Expansion over the grid basis . . . 55
4.1.2 Predictor–Corrector method . . . 58
4.1.3 Imaginary time propagation . . . 59
4.2 Integration scheme in three-dimension . . . 61

4.3 Integration scheme in cylindrical coordinates 63

5 Landau–Zener tunneling in tilted lattices 67
5.1 Landau–Zener limit of Wannier–Stark problem 68
5.2 Deviation from Landau–Zener limit 71
5.3 Survival probability in the ground band 75
5.4 Coherent control of Landau–Zener tunneling 81
5.4.1 Impact of lattice depth and the Stark force 81
5.4.2 Impact of initial condition 84
5.4.3 Calculation in different bases 86
5.5 Impact of atom-atom interactions 90
5.6 Summary 92

6 Time-dependent stochastic potentials 93
6.1 Hamiltonian with a time-dependent stochastic potential 93
6.2 Effective potential 95
6.3 Impact of exponentially correlated noise 97
6.3.1 Impact of the correlation time τ on tunneling 98
6.3.2 Impact of the Stark force on tunneling 102
6.3.3 Impact of the noise parameter D 103
6.4 Impact of harmonic noise 106
6.4.1 Harmonic noise in the exponentially correlated limit . . . 106
6.4.2 Impact of the oscillation frequency ω_0 108
6.4.3 Impact of the damping frequency Γ of harmonic noise . . 112
6.4.4 A scan over the noise parameters Γ and ω_0 113
6.4.5 Impact of $\langle\phi(t)^2\rangle$ on tunneling 114
6.4.6 Impact of T on the tunneling rate 116
6.4.7 Summary of the results 120
6.5 Time-dependent deterministic phase 122
6.5.1 Effective model 122
6.5.2 Impact of ω_d and amplitude A_d on the tunneling 124
6.5.3 One tilted lattice with a time-dependent deterministic phase 126

7 Conclusions and perspectives 131
7.1 Conclusion 131
7.2 Open questions 132
7.3 Future outlook 135

A Gauge transformation 137

Chapter 1

Introduction

The exciting phenomenon of tunneling is one of the most striking manifestations of quantum behavior and has been the subject of intense research since the beginning of the 20th century [1]. Quantum tunneling is a microscopic phenomenon where a particle can penetrate and in most cases pass through a potential barrier, even though it lacks the energy to reach the peak of the barrier. Such a motion is not allowed by the laws of classical dynamics. A fascinating aspect of the tunneling process is that the "tunneling" particles not only penetrate a classically forbidden area of any size, but also show an interesting time behavior. While tunneling *probabilities* can be calculated accurately even for complex quantum systems and have an intuitive interpretation as statistical mean values of experimental outcomes, the concept of tunneling *time* – the time required for a state to evolve into an orthogonal state – and its computation are still the subject of debate even for simple systems [2].

In quantum mechanical systems having two discrete energy levels, there is a possibility of a transition between the energy levels. A quantum system tunnels across an energy gap at an avoided crossing of the system's energy levels. This phenomenon, which is a well-known example of the tunneling problem, is known as *Landau–Zener* tunneling. Landau–Zener theory was developed in the early 1930's in the context of atomic scattering processes and spin dynamics in time-dependent fields [3, 4, 5, 6]. During the past decades, Landau–Zener transitions have been investigated for Rydberg atoms [7], molecular nanomagnets [8], field-driven superlattices [9], current-driven Josephson junctions [10], Cooper-pair box qubits [11], for using light waves in coupled waveguides [12, 13, 14] and just recently for coupled one-dimensional Bose liquids [15].

Unstable quantum systems exhibit exponential decay of the particle survival probability in the initial energy level, but deviations from this law at short and long times have been predicted [16]. In recent years, Landau–Zener tunneling

has been used in the observation of deviations from a purely exponential decay of a quantum system consisting of a few energy levels. An example for the latter was investigated by Raizen and co-workers [17], where clear evidence of short-time deviation from exponential decay was observed in the survival probability of ultracold atoms in an accelerating optical lattice. Moreover, Landau–Zener tunneling provides a building block for the quantum control of complex many-body systems [18].

Quantum transport is an essential topic in solid state physics and electronic applications. The physics of transport of electrons in a metal relies very much on the periodicity of the lattice. Bloch oscillations, Landau–Zener tunneling, and Wannier–Stark ladders [19, 20, 21, 22, 23, 24, 25] are fundamental quantum effects occurring in a system of electrons moving in a periodic potential and a static electric field. However, due to complications such as impurities, lattice vibrations, and multiparticle interactions clean observations of these effects have been difficult. Ultracold atoms and Bose–Einstein condensates [26] in optical lattices provide an extremely effective tool for engineering simple quantum systems with a broad tunability of the parameters [27], thus serving as "quantum simulators" [28] to reproduce the physics of different systems. The striking advantage offered by such atomic systems resides in the unprecedented possibility to work with perfectly isolated samples at quasi-zero temperature and to have experimental control on most of the system parameters, e.g., the lattice depth, the lattice constant or the strength of the atom-atom interactions, which can be precisely tuned. This high degree of control makes atomic systems attractive as model systems for crystal lattices.

When crystaline solids are studied on a sufficiently small length scale, one realizes that impurities and defects are always present, which can affect the transport of particles. Disorder is indeed an intrinsic property of all real systems. Even a small amount of disorder can cause dramatic changes in the physical properties of the system. Optical lattices are nowadays easy to realize in the laboratory, and their parameters can be perfectly controlled both statically and dynamically. More complicated potentials can be build up by adding further lattices [29, 30]. In fact, by superimposing laser beams from different directions and with slightly different wave-lengths, it is possible to generate many different three-dimensional lattice geometries [27]. From the theoretical point of view, a variety of phenomena is expected to occur in these systems, such as Anderson localization [31] and the quantum transition to the Bose glass phase originating from the interplay of interaction and static spatial disorder [32, 33, 34]. The question arises of how to control the dynamics of particles in quasiperiodic potentials (possibly time-dependent or even stochastic ones).

This thesis

In this thesis, our results on the Wannier–Stark system are presented. This system is realized with ultracold atoms forming a Bose–Einstein condensate in an optical lattice subjected to a static tilting force [27]. The tilt is experimentally implemented by accelerating the optical lattice [21, 22, 35]. We investigate the coherent control of the transport and of the decay of Bose-Einstein condensates from the ground band in a lattice structure with both periodic and with time-dependent stochastic potentials. To this respect, we compute the time dependence of the tunneling probability of the Bose–Einstein condensate atoms out of the ground band in which they were originally prepared. We demonstrate that by changing the initial condition and system parameters, and also by tuning the strength of atom-atom interactions, it is possible to control the tunneling rate of the Bose–Einstein condensate to higher bands. Finally, a controlled noise will be shown to be a further handle to engineer tunnelings.

The detailed outline of this thesis is as follows:

Chapter 2: This chapter provides the necessary tools for our studies. It starts with a short review on the bosonic system of ultracold atoms and the formation of Bose–Einstein condensate in section 2.1. In the first part of this section, the non-interacting dilute Bose-gas and in the second part, the interacting Bose–gas in the regime of weak atom-atom interactions are shortly reviewed. The dynamics of Bose–Einstein condensates in such a regime is very well described in a mean-field regime based on the so-called Gross–Pitaevskii equation. This nonlinear Hamiltonian to describe the dynamics of condensate atoms, that are trapped in a three-dimensional harmonic oscillator potential, is presented in the second part of section 2.1. Loading Bose–Einstein condensates in optical lattices is used to simulate solid state systems. Section 2.2 presents how the optical lattices can be created theoretically and experimentally through the interaction between atoms and light. In chapter 5, we study the dynamics of Bose–Einstein condensate in such a lattice structure. Later in section 2.2, it is described that more complex and non-periodic optical lattices can be generated easily by superimposing more laser beams with arbitrary frequency difference. This leads to our time-dependent stochastic potential that is used in chapter 6.

Due to the Stark force (external field), it is possible to make optical lattices tilted. Particles in periodic potential and in the presence of the external field perform oscillatory movements. The so-called Bloch oscillation phenomenon is described in section 2.3. The problem of finding the eigenstates of the periodic system under the influence of an external field, the so-called Wannier–Stark problem is introduced in section 2.4. Depending on system parameters, one can tune into a special condition for which the rate of tunnelings is enhanced or

suppressed. This effect appears in the Wannier–Stark system when the energy induced by the Stark force matches the energy difference between the initial and the final energy states. In such a condition, the tunneling probability is enhanced and a deviation from Landau–Zener tunneling prediction is observed. The so-called resonantly enhanced tunneling, which has been predicted theoretically [36] and has also been observed in experiments [37, 38], is described in section 2.4. Section 2.5 presents the theoretical background on tunneling of interacting Bose–Einstein condensate atoms in tilted optical lattices. A theoretical effective model based on perturbation theory was introduced by Niu [39] to describe the dynamics in such a nonlinear system. This model and its validity limits are reviewed in this section.

Chapter 3: The models which are used in this thesis are presented in this chapter. Section 3.1 collects the necessary theoretical background to describe the probability and transition times for Landau–Zener tunnelings. The dynamics of the system can be measured in different bases, diabatic and adiabatic. The diabatic basis is the eigenbasis of the bare states of the system when there is no coupling between the two states. The adiabatic basis, on the other hand, is the basis of a system with a finite coupling between the two states. The Landau-Zener model describing the transition at an avoided crossing is defined in the first part of this section, followed by analytical estimates for the Landau–Zener transition times which have been derived by Vitanov in [24, 40] using the two-state model. Vitanov calculated the time-dependent tunneling probability at finite times and in a given basis, e.g., adiabatic or diabatic, he obtained different transition times [40]. We study the Landau–Zener tunneling in various engineered potentials in chapter 5 and 6.

The potential which is used in chapter 6 is a time-dependent stochastic potential with its stochasticity arising from the time-dependent random phase in the secondary lattice. Section 3.2 focuses on the definition of different types of noise which are used as a time-dependent phase. Two algorithms are presented to generate colored noise: the exponentially correlated noise algorithm and the harmonic noise algorithm. Exponentially correlated noise, with a finite correlation time of fluctuations and Lorentzian spectral distribution, is a standard example of time-correlated noise. Comparing the correlation time of the noise to the characteristic time scale of the system, we distinguish two different regimes: slowly varying noise, and fast noise. Another type of colored noise is defined by using a noisy damped oscillator. The spectral distribution of this type of noise peaks at a finite frequency, and therefore allows the consideration of resonance phenomena. Different regimes of parameters are also defined for this type of noise. In the slowly varying regime, where the oscillation frequency of the harmonic noise is very small compare to the characteristic time scale of the system, the harmonic

noise recovers the exponentially correlated noise with Lorentzian spectral distribution. In the fast oscillating regime, the spectral distribution of the harmonic noise has a peak at a finite frequency. We also introduce a third type of a time-dependent phase in this section. We call it the deterministic phase and we define it by a sinusoidal function which has a delta function spectral distribution. The deterministic noise can be comparable to the harmonic noise when they have similar spectral distributions (i.e., with a very narrow peak at a finite frequency).

Chapter 4: In order to describe the dynamics of our systems, we need to integrate the Schrödinger or the Gross–Pitaevskii equation. Our numerical integration methods are presented in chapter 4. In order to prepare the initial state, we use an imaginary time method to integrate the Hamiltonian. Firstly, we discuss these methods for a one-dimensional system, then later in section 4.2 and 4.3, we generalize our technique to a general three-dimensional system and the cylindrical system, respectively.

Chapter 5: The Landau–Zener tunneling between the Bloch bands of a Bose-Einstein condensate in accelerated lattices is explored in this chapter. The lattice depth controls the tunneling barrier, while the tilt effectively controls the time dependence of the Hamiltonian. At large Stark forces, Landau–Zener tunnelings lead to significant interband transitions for the condensate [27, 41]. Section 5.1 presents the Wannier–Stark Hamiltonian which describes the dynamics of our system. It is shown how our original Hamiltonian is connected to the Landau–Zener model. The limits one faces in applying Landau–Zener theory to the Wannier–Stark system are presented in section 5.2. The tunneling process is detected by computing the atomic momentum distributions. The essential theoretical and numerical tools to describe our time-resolved computations are reported in section 5.3. There, it is described how we measure the time dependence of the survival probability by performing a projective quantum measurement on the eigenstates in a given basis of the Hamiltonian. Our calculation resolves the step-like time dependence of the survival probability. Section 5.4 presents our numerical results and the experimental data done in the group of Professor Ennio Arimondo in Pisa on the time evolution of the survival probability of the Bose–Einstein condensate in the ground band. These results demonstrate that by changing the system parameters such as lattice amplitude, Stark force and the initial condition, it is possible to manipulate the tunneling probability of the condensate. Using different numerical as well as experimental protocols (in the group of Professor Ennio Arimondo in Pisa), it is possible to perform our calculations and experiments both in the adiabatic basis of the lattice eigenstates and in the diabatic basis of the free-particle momentum eigenstates. We present the-

oretical and experimental results which clearly show that the time dependence of the transition probability exhibits a step-like structure with a finite transition time and oscillations with a finite damping time, all of them depending on the choice of the measurement basis. Finally, in section 5.5, it is shown that by introducing atom-atom interactions into the system, and tuning its strength, we are able to control the tunneling rate of the condensate to higher bands. To describe the dynamics of interacting condensate atoms, we perform a mean-field calculation based on the three-dimensional Gross–Pitaevskii equation. The presented results in chapter 5 on the time-resolved calculations and experimental observations – obtained in collaboration with Professor Ennio Arimondo's experimental group in Pisa – of Landau–Zener tunneling were published in [42, 43, 44].

Chapter 6: Finally in chapter 6, new results – yet to be tested experimentally – on the tunneling probability in the time-dependent disorder system are presented. Using the bichromatic lattice defined in section 2.2, and combining it with different time-correlated types of noise presented in section 3.2, we define a time-dependent stochastic potential. The aim of this chapter is to engineer the tunneling of the Bose–Einstein condensate in such a time-dependent stochastic potential which is tilted due to the Stark force. The results show that a controlled time-dependent noise is a further handle to engineer the interband transitions. The exponentially correlated noise (which was defined in section 3.2.1) is used in section 6.3, and the harmonic noise defined in section 3.2.2 is employed in section 6.4 as the time-dependent phase. The impact of different regimes of noise parameters are investigated on the tunneling rate of condensates. Our results show that depending on its parameters and its strength, the noise can enhance or suppress the tunneling compared with the reference system (as defined by the Wannier–Stark Hamiltonian in chapter 5) in a systematic way. We calculate analytically an effective model which can be used as a benchmark to describe our results in the regime of fast oscillating noise. Finally, section 6.5 focuses on the deterministic time dependent phase defined in section 3.2.3. This case acts as a further benchmark of generally noise-driven dynamics, and we study the impact of fast and slow oscillating function on the tunneling probability of the system.

Finally, we conclude our studies and results in the last chapter. We present some of the open questions which allow for further studies. We also give an outlook to possible extensions which can be considered for the presented work.

Chapter 2

Ultracold atoms and optical lattices

2.1 Bose–Einstein condensation

At the beginning of the 20th century, following the work of Bose on the statistics of photons [45], Einstein considered a gas of non-interacting, massive particles, and concluded that, below a critical temperature of about one hundred nano Kelvin a finite fraction of the total number of particles would occupy the lowest energy single-particle state [46]. Such a system undergoes a phase transition and forms a Bose–Einstein condensate, where a macroscopic number of particles occupy the lowest energy state. The experimental discovery of Bose–Einstein condensation in ultracold trapped atomic clouds for rubidium [47], sodium [48], and lithium [49], opened up the exploration of quantum phenomena in a qualitatively new regime [26].

According to the theory of an ideal quantum gas of particles with mass M conform to Bose–Einstein statistics, at temperature T, a phase transition occurs when the de Broglie wavelength of characteristic thermal motions, $\lambda_{\mathrm{dB}} = (2\pi\hbar^2/Mk_BT)^{1/2}$, becomes comparable to the mean inter-particle separation, $r = n^{-1/3}$. The parameter k_{B} is the Boltzmann constant, and n the atom number density. The particle density at the center of a Bose–Einstein condensed atomic cloud is typically $10^{13} - 10^{15}\ \mathrm{cm}^{-3}$ [50]. This density, on one hand, is much less than the density of molecules in air at room temperature ($10^{19}\ \mathrm{cm}^{-3}$). On the other hand, in order to observe quantum phenomena at such a low density, the temperature of the system must be of the order of $10^{-5}\ \mathrm{K}$ or less which is in contrast to the critical temperatures in solids and liquids (e.g., the Fermi temperature which is typically $10^4 - 10^5\ \mathrm{K}$, or the Debye temperature which is typically of the order of $10^2\ \mathrm{K}$).

Laser cooling methods are used to cool down alkali metal atoms but since these techniques alone cannot produce sufficiently high densities and low temperatures for condensation, it is followed by an evaporative cooling stage. During the latter stage, more energetic atoms are removed from the trap, and as a result the remaining atoms are cooled further. A microscopic population of atoms in the ground state of the system is achieved at such a low temperature [27].

Every realistic Bose gas shows some level of particle-particle interaction. Therefore, the system of an ideal gas consisting of non-interacting Bosons is a fictitious system. Nevertheless, this model provides the simplest example for the realization of Bose–Einstein condensation. At zero temperature, a non-interacting Bose gas is fully condensed and all N particles are described by identical single particle wave functions [50]. The many-body ground-state wave function is then given by the product of N identical ground-state wave functions

$$\Psi(\mathbf{r}_1, \mathbf{r}_2, ..., \mathbf{r}_N) = \prod_{i=1}^{N} \psi(\mathbf{r}_i). \tag{2.1}$$

This so-called condensate wave function is a normalized macroscopic wave function. For a non-interacting Bose gas and an inhomogeneous system, this single-particle state is simply the single particle ground-state of the confining potential. In a harmonic trap, for example, the ground state wave function is a Gaussian wave function, and for a periodic potential the ground state single particle wave function is a Bloch wave function with a quasi-momentum $q = 0$ (see chapter 5) [27]. In section 2.1.1, the non-interacting Bose gas and some basic concepts such as the critical temperature T_c of the condensation, the condensate fraction N_0/N[1], as well as the issue of dimensionality will be addressed.

When weak interactions between particles are included in the problem, the ground-state many-body wave function is still, to a very good approximation, a product of N single-particle wave functions. These wave functions are now obtained from the solution of a nonlinear Schrödinger equation [27]. This equation is known as Gross–Pitaevskii equation, which will be derived in section 2.1.2, and describes the dynamics of weakly interacting bosons.

2.1.1 Non-interacting dilute Bose–gas

For non-interacting bosonic atoms in thermal equilibrium the mean occupation number of the single-particle state s is given by the Bose distribution

$$f(\epsilon_\mathrm{s}) = \frac{1}{e^{(\epsilon_\mathrm{s}-\mu)/k_\mathrm{B}T} - 1}. \tag{2.2}$$

[1] N_0 is the number of the atoms in condensate and N is the total number of the atoms.

where $\epsilon_{\rm s}$ is the energy of the single-particle state s for the particular trapping potential under consideration, and μ being the chemical potential.

Density of states

The energy density of states varies as a power of energy according to

$$g(\epsilon) = C_\alpha \epsilon^{\alpha-1}, \tag{2.3}$$

where the parameter C_α is a constant and α is half the number of classical degrees of freedom per particle. For a gas confined in an anisotropic three-dimensional harmonic oscillator potential with oscillation frequencies ω_i in three directions (as in standard Bose–Einstein condensate experiments), the parameter $\alpha = 3$ [2], and the density of states is given by

$$g(\epsilon) = C_3 \epsilon^2 = \frac{\epsilon^2}{2\hbar^3 \omega_1 \omega_2 \omega_3}. \tag{2.4}$$

For a uniform Bose gas in a three-dimensional box, where $\alpha = 3/2$ [3], the density of states is given by [50]

$$g(\epsilon) = C_{3/2} \epsilon^{1/2} = \frac{V m^{3/2} \epsilon^{1/2}}{\sqrt{2}\pi^2 \hbar^3}. \tag{2.5}$$

Transition temperature

The critical temperature $T_{\rm c}$ is defined as the highest temperature at which the lowest energy-state acquires a macroscopic occupation. The number of the particles in excited states given by

$$N_{\rm ex} = \int_0^\infty d\epsilon g(\epsilon) f(\epsilon), \tag{2.6}$$

which has its greatest value for the zero chemical energy. Considering zero chemical energy $\mu = 0$ at temperature $T = T_{\rm c}$ and vanishing number of particles in the condensate $N_0 \approx 0$, i.e., all particles ($N = N_0 + N_{\rm ex}$) being accommodated in excited states, leads to the equation

$$N = N_{\rm ex}\left(T_{\rm c}, \mu = 0\right) = \int_0^\infty d\epsilon g(\epsilon) \frac{1}{e^{\epsilon/k_{\rm B}T_{\rm c}} - 1}. \tag{2.7}$$

[2] A harmonic oscillator has two *vibrational* degrees of freedom along each direction: $\bar{E}_{vib,x} = \frac{p_x^2}{2M} + \frac{m\omega_x^2 x^2}{2}$.

[3] There are three independent degrees of freedom for a *linear motion* along the x, y, and z coordinates : $\bar{E}_{Lin} = \frac{p_x^2}{2M} + \frac{p_y^2}{2M} + \frac{p_z^2}{2M}$.

Using Eq. (2.7) for atoms trapped in a three-dimensional harmonic oscillator potential, with $g(\epsilon)$ given in Eq. (2.4), the transition temperature $T_{\rm c}$ acquires the form

$$k_{\rm B}T_{\rm c} = \hbar\bar{\omega}\left(\frac{N}{\zeta(3)}\right)^{1/3} \approx 0.94\hbar\bar{\omega}N^{1/3}, \tag{2.8}$$

where $\bar{\omega} = (\omega_1\omega_2\omega_3)^{1/3}$ is the geometric mean of the three frequencies of the oscillator and $\zeta(\alpha)$ is the Riemann zeta function [50].

For a uniform Bose gas in a three-dimensional box, with $g(\epsilon)$ given in Eq. (2.5), the transition temperature is given by $k_{\rm B}T_{\rm c} \approx 3.31\hbar^2 n^{2/3}/M$, where $n = N/V$ is the number density [50].

Density profile

One of the quantities that can be measured experimentally is the density profile $n(\mathbf{r}) = N_0|\psi_0(\mathbf{r})|^2$, with N_0 being the number of atoms in the condensate. It reflects the shape of the ground-state wave function, $\psi_0(\mathbf{r})$, for a particle in the trap. The density profile for the ground-state wave function of the condensate in an anisotropic harmonic trap is given by

$$n(\mathbf{r}) \equiv N_0|\psi_0(\mathbf{r})|^2 = N_0\left(\frac{M\bar{\omega}}{\pi\hbar}\right)^{3/2} e^{-\frac{M}{\hbar}\left(\omega_1 x^2+\omega_2 y^2+\omega_3 z^2\right)}. \tag{2.9}$$

The widths of the wave function in the three directions are given by $a_i^2 = \hbar/M\omega_i$ (cf. Thomas–Fermi limit in section 2.1.2). This density profile is used as the initial state of the system under consideration which will be presented in chapter 5. The density profile given in Eq. (2.9) may be contrasted with the corresponding expressions when the gas obeys classical statistics. Then, at temperatures above the critical temperature $T > T_{\rm c}$, the corresponding density distribution is

$$n(\mathbf{r}) = N\left(\frac{M\bar{\omega}^2}{2\pi k_{\rm B}T}\right)^{3/2} e^{-\frac{M}{2k_{\rm B}T}\left(\omega_1^2 x^2+\omega_2^2 y^2+\omega_3^2 z^2\right)}. \tag{2.10}$$

The widths are given by $R_i^2 = 2k_{\rm B}T/M\omega_i^2$ and depend on the temperature. The ratio $R_i/a_i = \sqrt{2k_{\rm B}T/\hbar\omega_i} \gg 1$ for $T > T_{\rm c}$. Therefore, the thermal cloud is much broader than the condensate. Taking the Fourier transforms one can obtain the momentum distribution of the condensate, this can be easily measured experimentally [50].

2.1.2 Interacting Bose gas in the mean-field limit

The condensate typically consists of a few thousands to millions of atoms which are confined by a trapping potential. The macroscopic behavior of the Bose–Einstein condensate is affected by the internal interactions between the atoms, and by the shape of the external trapping potential. The atom-atom interaction in a cold dilute gas of bosonic atoms is dominated by elastic binary collisions and can be treated in the framework of scattering theory. At very low temperature, given the fact that the thermal de Broglie wavelength λ_{dB} is much larger than the mean inter-particle separation, only s-wave collisions are important. For a dilute gas the interaction can be modeled by a zero-range potential whose strength is proportional to the s-wave scattering length a_{s}. The interatomic potential can be replaced by an effective contact interaction [50]

$$V_{\mathrm{int}}(\mathbf{r}) = \frac{4\pi\hbar^2 a_{\mathrm{s}}}{M} \cdot \delta(\mathbf{r}) = g \cdot \delta(\mathbf{r}), \tag{2.11}$$

where $\mathbf{r}$ is the relative coordinate between two atoms, M is the mass of the atoms, a_{s} is the s-wave scattering length and $g = 4\pi\hbar^2 a_{\mathrm{s}}/M$ is the coupling constant [50]. The strength of two-body interactions ($\propto a_{\mathrm{s}}$) in the ultracold atomic gas can be tuned by means of Feshbach resonances [51]. It is possible to create attractive interactions, for a negative a_{s}, repulsive interactions when $a_{\mathrm{s}} > 0$, or even non-interacting gases.

Gross–Pitaevskii equation

For a dilute gas, the system can be described by a mean field description. The diluteness of the gas is characterized by the ratio of the scattering length a_{s} and the inter-particle spacing. This ratio can be expressed as a gas parameter na_{s}^3 and is typically less than 10^3. In this limit, due to the mean-field of all other atoms in the condensate, each atom feels an additional potential. Therefore, the interaction potential is proportional to the local atomic density $|\psi(\mathbf{r},t)|^2$. The dynamic properties of a Bose–Einstein condensate at temperatures $T < T_c$ are usually well modeled by a general nonlinear Schrödinger equation for the macroscopic wave function [50]. This equation is known as the time-dependent Gross–Pitaevskii equation [52]

$$i\hbar\frac{\partial\psi(\mathbf{r},t)}{\partial t} = -\frac{\hbar^2}{2M}\nabla^2\psi(\mathbf{r},t) + V_{\mathrm{ext}}(\mathbf{r})\psi(\mathbf{r},t) + gN_0|\psi(\mathbf{r},t)|^2\psi(\mathbf{r},t). \tag{2.12}$$

This equation contains the trap potential $V_{\mathrm{ext}}(\mathbf{r})$, typically a three-dimensional harmonic oscillator potential, as well as the atom-atom interactions in the form of the nonlinear term. The coefficient of the nonlinear term consists of the

coupling constant g which specifies the strength of the atom-atom interaction, N_0 the number of the atoms in the condensate, and the local atomic density $|\psi(\mathbf{r},t)|^2$.

In this weakly interacting regime, the many-particle wave function $\psi(\mathbf{r})$ is still the product of identical single particle wave functions as is the case for the ideal Bose gas (as in Eq. (2.1)). Contrary to the non-interacting case, the weakly interacting gas does not condense into the ground state of the single particle problem but instead into a state which is determined through the Gross Pitaevskii equation as given in Eq. (2.12). This equation is also valid in the quasi-1D and quasi-2D regimes where the gas is tightly confined in the transverse directions by means of a harmonic trap. To obtain the lower-dimensional equations one assumes separability of the condensate wave function in its transverse coordinates and projects onto the mean-field ground state in the transverse directions [53]. Then, ∇^2 becomes the appropriate d-dimensional Laplacian, and the coupling constant g becomes dependent on the transverse confinement. Specifically, in d-dimensions, one finds :

$$g_{1\mathrm{D}} = 2\hbar\omega_\perp a_\mathrm{s},\ g_{2\mathrm{D}} = \sqrt{\frac{8\pi\hbar^3\omega_\mathrm{z}}{M}};\ \text{and}\ \ g_{3\mathrm{D}} = \frac{4\pi\hbar^2 a_\mathrm{s}}{M}, \tag{2.13}$$

where $\omega_\perp$ and ω_z are the transverse harmonic oscillator frequencies of the confinement in one-dimension and two-dimension, respectively. The three-dimensional $g_{3\mathrm{D}}$ is included for completeness and everywhere in this thesis it is represented by g. The quasi-1D (-2D) regime is obtained: (i) if the transverse confinement length $l_\perp \equiv \sqrt{\hbar/M\omega_\perp}$ ($l_z \equiv \sqrt{\hbar/M\omega_z}$) is on the order of the condensate healing length $\xi_\mathrm{h} = 1/\sqrt{8\pi\bar{n}a_\mathrm{s}}$ [50], where $\bar{n}$ is the mean particle density, and (ii) if the trapping is sufficiently strong in the transverse directions so that $\omega_\perp \gg \omega_x$ ($\omega_z \gg \omega_x, \omega_y$), where x is assigned as the longitudinal direction in one-dimension and the $x-y$ plane the two-dimensional plane for two-dimension.

Stationary solution of the Gross–Pitaevskii equation

The ground-state can be easily calculated from Eq. (2.12), using the ansatz $\psi(\mathbf{r},t) = \exp(i\mu t/\hbar)\phi(\mathbf{r})$, where μ is the chemical potential and $\phi(\mathbf{r})$ is the many-particle wave function which is a real and normalized function. Therefore, the equilibrium structure of the condensate is described by the time-independent Gross–Pitaevskii equation

$$\mu\phi(\mathbf{r}) = \left(-\frac{\hbar^2}{2M}\nabla^2 + V_\mathrm{ext}(\mathbf{r}) + gN_0|\phi(\mathbf{r})|^2\right)\phi(\mathbf{r}). \tag{2.14}$$

Thomas–Fermi limit

Comparing the kinetic energy with the mean-field energy, one can distinguish between the weak and the strong interaction regimes. In the so-called Thomas–Fermi limit the nonlinear interaction energy is much greater than the kinetic energy, hence the kinetic energy can be neglected. From Eq. (2.14) in the Thomas–Fermi limit, an algebraic solution for the density profile of the condensate is obtained

$$n^{TF}(\mathbf{r}) \equiv |\phi(\mathbf{r})|^2 \approx \frac{\mu - V_{\text{ext}}(\mathbf{r})}{N_0 g}. \tag{2.15}$$

For a Bose–Einstein condensate in a three-dimensional harmonic confinement the dimension-less parameter $N_0|a_{\text{s}}|/a_{\text{ho}}$, where $a_{\text{ho}} = \sqrt{\hbar/M\bar{\omega}}$ is the harmonic oscillator length scale, fixes the effective strength of the inter-atomic forces in the Gross–Pitaevskii equation given in Eq. (2.12). When $N_0|a_{\text{s}}|/a_{\text{ho}} \gg 1$ then the repulsive interactions makes the system wider than the non-interacting case. In this condition, the equilibrium arises from a balance between the external potential $V_{\text{ext}}(\mathbf{r})$ (here the harmonic trap) and the repulsive atom-atom interaction and since the kinetic energy play a minor role one can neglect it. This leads to the Thomas–Fermi approximation and therefore the density profile is given by:

$$n^{TF}(\mathbf{r}) = \frac{\mu}{N_0 g}\left[1 - \sum_{i=1}^{3}\left(\frac{r_i}{R_i^{\text{TF}}}\right)^2\right], \tag{2.16}$$

which is an inverted paraboloid, with the Thomas-Fermi radii $R_i = \sqrt{2\mu/M\omega_i^2}$. The Thomas–Fermi condition implies that $\mu \gg \hbar\bar{\omega}$ and $R_i \gg a_{\text{ho}}$ [50]. The Normalization of the density to one ($\int n^{TF}(\mathbf{r})d\mathbf{r} = 1$) leads to a fixed chemical potential μ [54]:

$$\mu = \frac{1}{2}\left(\frac{15}{4\pi}\bar{\omega}^3 N_0 g M^{3/2}\right)^{0.4}, \tag{2.17}$$

where $\bar{\omega} = (\omega_x\omega_y\omega_z)^{1/3}$. The expressions given in Eqs. (2.15) and (2.17) will be used in section 2.5 to calculate the effective potential in the presence of atom-atom interactions and an analytical expression for the dimensionless coupling constant.

2.2 Optical lattices

2.2.1 Connection to solid state physics

Following the classical experiments which showed the mechanical action of light on neutral atoms [55], proving the theoretical prediction of Maxwell that electromagnetic waves carry momentum, the development of the laser made it possible to realize resonant light forces on neutral particles. It was only in 1970s that the first scattering measurements were done using both traveling and standing waves [56]. In 1998 Anderson and Kasevich loaded a Bose-Einstein condensate in a standing light wave [23] which was the beginning point to study the Bose-Einstein condensate dynamics in periodic potentials [27].

Optical lattices are periodic potentials created by light-atom interactions. When an atom interacts with an electromagnetic field, the energy of its internal states depends on the light intensity. Therefore, a spatially dependent intensity induces a spatially dependent potential energy [57]. The system of a particle in a periodic optical potential is the textbook model of an electron in a crystal lattice. Optical lattices have several advantages with respect to solid state systems. The optical systems can be made free from defects, resulting in a larger mean free path of particles. Defects prevented for example the observation of the theoretically predicted coherent phenomenon such as Bloch oscillations[4]. The lattice depth and geometry can be be controlled easily by optical means. Using multiple-beam interference makes it possible to realize two-dimensional and three-dimensional lattices, superlattices, ratchets or more complex structures. In optical systems the relaxation time can be made much larger than the coherent timescale. In addition, the possibility to dynamically control the interaction potential in real time during the experiment allowed recent experiments to observe many of the coherent effects, such as Bloch oscillation and Wannier-Stark ladders, which are hardly accessible in solid state systems [19, 22, 27, 35, 58, 59, 60].

2.2.2 Interaction of atoms and light

Neutral atoms interact with a light field in both a dissipative and a conservative way. The conservative interaction comes from the interaction of the light field with the light induced dipole moment of the atom. It causes a shift in the potential energy – the so-called Stark shift. The dissipation arises due to the absorption of photons followed by spontaneous emissions. It results in a dissipative force on the atoms caused by the momentum transfer of the absorbed and spontaneously

[4] Bloch oscillation is one of the resulting coherent effects in a system of a periodic potential under the influence of externally applied fields in crystalline solids which was only observed in 1992 [19]

emitted photons. This light force is widely used for laser cooling and magneto optical traps. [61] For a large detuning of the light from atomic resonances, spontaneous emission processes can be neglected and the energy shift can be used to create a conservative trapping potential for neutral atoms [61, 62].

Periodic optical potentials are created by superimposing two laser beams with the same frequency ω_L (see Figure 2.1). The resulting electric field is of the form

$$\mathbf{E}(\mathbf{r},t) = \frac{1}{2}E_0(e^{i(\mathbf{k}_1\cdot\mathbf{r}+\omega_L t)} + e^{i(\mathbf{k}_2\cdot\mathbf{r}-\omega_L t)}) + c.c., \tag{2.18}$$

where E_0 is the amplitude, $k_i = 2\pi/\lambda_i$ is the wave vector, with $i = 1, 2$, and λ_i being the laser wavelength. The atom-field interaction energy reads [63]

$$H_{int} = -\mathbf{d}\cdot\mathbf{E}\left(\mathbf{r},t\right). \tag{2.19}$$

For a sufficiently large detuning from resonance [64], the potential seen by the particle can be written as [63]

$$H_{int} = \frac{\hbar\Omega_R^2}{4\Delta_L}\left(e^{i\mathbf{k}\cdot\mathbf{r}} + e^{-i\mathbf{k}\cdot\mathbf{r}}\right), \tag{2.20}$$

where Ω_R is the resonant Rabi frequency and $\Delta_L = \omega_L - \omega_0$ is the average detuning from resonance. The frequency difference between the two beams is vanishing and the wavenumber difference is $\mathbf{k} = \mathbf{k}_2 - \mathbf{k}_1$. Using two laser beams with an equal absolute value of wavenumbers as $\mathbf{k}_L \equiv \mathbf{k}_1 = -\mathbf{k}_2$, then $\mathbf{k} \equiv 2\mathbf{k}_L$. This leads to an effective Hamiltonian for an atom in the ground state

$$H = \frac{\mathbf{p}^2}{2M} + \frac{V_0}{2}\cos(2\mathbf{k}_L\cdot\mathbf{r}). \tag{2.21}$$

The amplitude of the periodic potential is $V_0 = \frac{\hbar\Omega_R^2}{\Delta_L}$. The expression for the well depth V_0 contains the resonant Rabi frequency Ω_R which can be written in terms of laser intensity I. The lattice depth can be expressed in terms of measurable quantities [21, 27] as

$$V_0 = \zeta\hbar\frac{I}{I_s}\frac{\Gamma_s^2}{\Delta_L}, \tag{2.22}$$

where I_s is the saturation intensity, ζ is a correction which depends on the level structure of the atom and Γ_s is the photon scattering rate [65]. The usual quantities related to the lattice are defined starting from the recoil momentum, $p_{\rm rec} = \hbar k_L$ that an atom acquires, when absorbing or emitting a single photon of light. Typically the lattice depth V_0 is expressed in units of recoil energy $E_{\rm rec}$ exchanged by an atom and a photon

$$E_{\rm rec} = \frac{\hbar^2 k_L^2}{2M}. \tag{2.23}$$

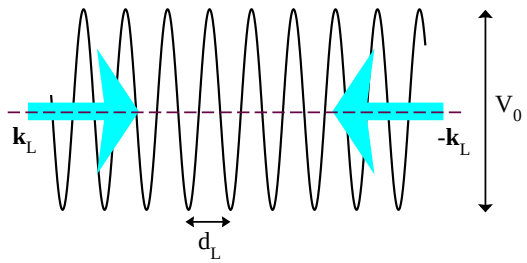

Figure 2.1: A one-dimensional optical lattice created from counterpropagating laser beams. The parameters V_0 is the lattice depth and $d_L = \lambda/2$ the lattice spacing.

Considering two counter-propagating laser beams along the x-axis as depicted in Figure 2.1, the resulting one-dimensional periodic potential can be written as $V(x) = V_0 \sin^2(k_L x)$. This one-dimensional optical lattice along the x-axis is used for the problem under consideration in this thesis.

Bloch's theorem states that eigenfunctions of the periodic system take the form of a plane wave envelope function multiplied by a periodic function $u_{nk}(x)$ with the same periodicity $d_L = \lambda/2 = \pi/k_L$ as the optical lattice, i.e.,

$$\psi_{nk}(x) = e^{ikx}\, u_{nk}(x). \tag{2.24}$$

The parameter k is the allowed wavevector of the particle which is restricted to the Brillouin zone $[-k_L, k_L]$ in the quasimomentum space. The energy eigenvalues $E_n(k) = E_n(k+K)$ are continuous periodic functions of the wavevector k, with periodicity K. They create the energy bands, the so-called band structure. The parameter n labels the energy bands and is known as the band index. Therefore, the solutions to a periodic Hamiltonian are Bloch waves with the band structure.

In the absence of the optical lattice i.e., the free particle problem, every positive value of energy as a function of momentum is allowed and hence the dispersion of the energy versus quasimomentum k is a parabolic function $E(k) = \hbar^2 k^2/2M$ (dashed line in Figure 2.2). In the presence of the periodic lattice with a finite depth V_0, however, the lowest crossing points of the free energy parabolas at $k = \pm k_L$ develop a level repulsion due to the coupling of the levels by the potential term. The coupling term $V_0 \sin^2(k_L x)$ connects only states with a difference in momentum of $2\hbar k_L$. Consequently, as seen in Figure 2.2, ranges of forbidden or allowed energies (so-called band structure) are introduced. The mean velocity of a particle in a particular Bloch state ψ_{nk} is determined by the energy dispersion relation

$$v_n(k) = \frac{1}{\hbar}\frac{\partial E_n(k)}{\partial k}. \tag{2.25}$$

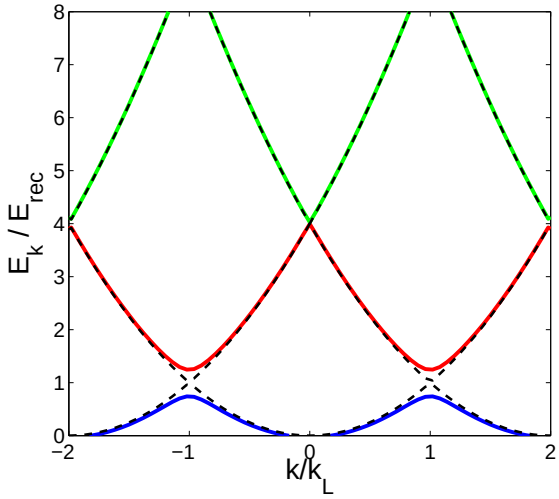

Figure 2.2: Energy dispersion curves of a particle in a sinusoidal potential are shown for the depth $V_0 = 0$ (black dashed lines) and for $V_0 = 1\,E_{\rm rec}$ (colored solid lines).

2.2.3 Non-periodic optical lattices

Since no real system is fee of defects, disorder in quantum systems has been the subject of intense theoretical and experimental activity over the past decades. Although in many situations the effect of disorder is weak and can be ignored, in some cases even an arbitrarily weak disorder may have spectacular effects on the physical properties of these systems and result in a variety of non-intuitive phenomena, especially in one-dimensional quantum systems [66]. The most famous phenomenon is the localization and absence of diffusion of noninteracting quantum particles [67].

One possibility to create disorder potentials is provided by using speckle patterns [68, 69]. The speckle field is a light field with highly disordered intensity and phase distributions but is nevertheless stationary and coherent. The speckle field can be easily generated in experiments by introducing a diffuser in the path of a coherent light beam or by reflecting a laser beam against a surface that is rough on the scale of the laser wavelength [69]. Another possibility to produce quasi-disordered potentials is by using multi-chromatic incommensurate optical lattices [33, 70, 71]. The spectral properties and the amount of disorder in both the above mentioned methods are known with a very good accuracy and can be easily controlled by optical means.

In addition to optical methods, there exist other techniques to create disorder potentials. For instance, atomic mixtures [72] resembles the presence

of impurities in solid disorder, or inhomogeneous magnet fields [73] are two other ways to produce disorder in the system. In the present work, the disorder created by incommensurate bichromatic optical lattice is studied.

Optical lattices are easy to realize in the laboratory, and their parameters such as lattice depth and spatial period can be perfectly controlled by optical means. More complicated optical potentials can be realized by adding further lattice beams [33, 70, 71]. In fact, by superimposing laser beams from different directions and with different frequencies, it is possible to generate a huge variety of lattice geometries in a very controlled way. This suggests the idea that by combining several optical standing waves with different incommensurate spacing, it is possible to produce complex potentials with very small lattice constants ("grain size") which is the advantage of multichromatic lattices over speckle fields that are often too coarse-grained. The so-called quasi-disorder optical lattices in one, two and three dimensions have been investigated [74, 75].

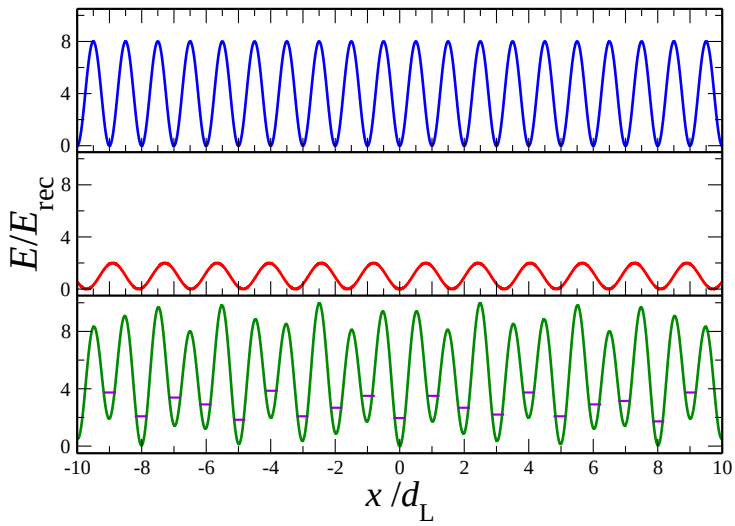

Figure 2.3: Upper panel shows the original optical lattice $V_1 \sin^2(k_1 x)$, the middle panel is an example for the secondary lattice $V_2 \sin^2(k_2 x)$ with $V_1 \ll V_2$ and the lower panel is the superposition of the two lattices resulting in a quasiperiodic potential $V(x) = V_1 \sin^2(k_1 x) + V_2 \sin^2(k_2 x)$ with random site-to-site energy differences. Amplitudes of the potentials are expressed in the unit of recoil energy $E_{\rm rec} = \hbar^2 k_1^2/2M$ associated with the first lattice.

An experimentally accessible way to create quasi-disorder in a lattice (main lattice) is to add a second lattice (disordering lattice) with an incommensurate wavelength. One expects that in a finite system, this non-periodic modulation

can produce the same qualitative effects as the ones induced by a truly random potential [70, 71]. The one-dimensional bichromatic potential resulting from the superposition of the two lattices can be written as

$$V(x) = V_1 \sin^2(k_1 x) + V_2 \sin^2(k_2 x + \phi). \tag{2.26}$$

The height of the two lattices are V_i $(i = 1, 2)$, where $k_i = 2\pi/\lambda_i$ give the lattice wavenumbers and ϕ is an arbitrary phase. The condition of incommensurability implies the ratio of the two lattice wavenumbers, $\beta = k_2/k_1$, being an irrational number. The potential of wavelength λ_1 creates the primary lattice of period $d_{\mathrm{L1}} = \lambda_1/2$, that in the limit of $V_1 \ll V_2$, is weakly perturbed by the secondary lattice of wavelength λ_2 [33]. The effect of the secondary lattice reduces to an inhomogeneous and non-periodic shift of the potential energy at the bottom of the lattice wells. Therefore, the presence of weak disorder introduces random site-to-site energy differences [33] (see Figure 2.3).

Another technique which is proposed in the current work to create random potentials is using a time-dependent bichromatic potential. This type of optical potential can be generated by imposing an additional optical lattice with comparable amplitude but incommensurate wavelength and with the time–dependent random phase on an already existing periodic potential:

$$V(x,t) = V_1 \sin^2(k_1 x) + V_2 \sin^2(k_2 x + \phi(t)). \tag{2.27}$$

$\phi(t)$ is the time–dependent random phase which is introduced to shift the second lattice randomly and time-dependently with respect to the other one. Different types of stochastic noise to generate $\phi(t)$ are addressed in section 3.2 of chapter 3. Therefore, such a disordered potential is not only spatially, but also temporally random. More details on the effects of such time-dependent random potentials will be presented in chapter 6.

Finite size effect and incommensurability

The bichromatic incommensurate lattices are quasi-periodic potentials, since their spectrum is made up of a set of discrete frequencies. However, because of the lack of any translational invariance, they can be used to study the physics of finite-sized disordered systems. One should also be more careful with the concept of incommensurability when dealing with finite-sized atomic samples. From an experimental point of view, the measurement of the ratio λ_2/λ_1 always gives a rational number, since the lattice wavelengths are only known with finite precision. From a theoretical point of view, however, it is important to consider that the finite size of the systems releases the constraints on the incommensurability: even a periodic potential (resulting from a commensurate ratio) does not show any

periodicity if the system size is smaller than the period. The bichromatic lattice is thus effectively incommensurate provided that the ratio between the wavelengths is far from a ratio between simple integer numbers. More precisely, a bichromatic lattice can be considered incommensurate whenever the resulting periodicity (if any) is larger than the system size. The effective correlation length in the system consisted of bichromatic lattices is given by $\lambda_s = \lambda_1\lambda_2/|\lambda_1 - \lambda_2|$ (considering the realistic situation for the bulk physics), i.e., the non-periodic modulation of the energy minima with length scale $d = \lambda_s/2$. $\lambda_1, \lambda_2 \ll \sqrt{\hbar/(M\omega)}$, where ω is the harmonic trap frequency.

Realization of disorder in ultracold atomic gases

The atomic-optical disordered systems provide the best possible ground to test theoretical predictions. Loading the Bose–Einstein condensation in disordered potentials leads to various phenomena. One of these interesting phenomena is the Anderson localization predicted by Anderson in 1950s [67]. According to this prediction the extended Bloch waves, for strong enough disorder, become localized with an exponentially decaying envelope $|\psi| \sim \exp(|\mathbf{r} - \mathbf{r}_i|/\xi)$, with the localization length ξ [67, 76, 77]. Only in 2008, Anderson Localization was observed experimentally by localization of a Bose-Einstein condensate in a 1D disordered optical potential [31]. Bose-Glass transition is another phenomenon which results from the presence of disordered potentials in the system of Bose-Einstein condensation. This transition originates from the interplay of interaction and disorder [32, 33, 70, 71]. Disorder causes also a damping of Bloch oscillations of Bose–Einstein condensates in optical lattices [29, 78]. Effects of disorder have also been observed for Bose–Einstein condensates in microtraps as a consequence of intrinsic defects in the fabrication of the microchip [79, 80].

In the case of non-interacting Bose–Einstein condensate, the axial and transverse degrees of freedom are separable. Along the direction of the bichromatic lattice, the system is described by the single-particle Hamiltonian $H_{1\mathrm{D}} = -\hbar^2\nabla_x^2/(2M) + V(x)$. In the tight-binding limit this system can be mapped to the Aubry-André model [81] by expanding the particle wavefunction ψ over a set of maximally localized Wannier states $|w_j\rangle$ at the lattice site j. The resulting Hamiltonian is

$$H = -J\sum_j \left(|w_j\rangle\langle w_{j+1}| + |w_{j+1}\rangle\langle w_j|\right) + 2\Delta\sum_j \sin^2\left(\pi\beta j + \phi\right)|w_j\rangle\langle w_j|, \tag{2.28}$$

where J is the tunneling amplitude between adjacent sites, that depends on the height of the main lattice. The strength of the disorder Δ can be written as $\Delta \simeq V_2\beta^2/2$ [82], where $\beta = \lambda_1/\lambda_2$ is the ratio of the two lattice wavenumbers.

In experiments, the two relevant energies J and Δ can be controlled independently by changing the heights of the primary and secondary lattice potentials respectively. The bichromatic potential can display features of quasidisorder when β is irrational. A common choice in the study of the Aubry-André model is the inverse of the golden ratio, $\beta = \left(\sqrt{5}-1\right)/2$ [81].

Our disordered system, which is defined in chapter 6, is similar to the model above in the sense that it consists of a bichromatic lattice. But in our case there is a time-dependence in the second lattice which makes it different from the static model introduced above.

2.2.4 Tilted optical lattices

As mentioned in section 2.2.1, ultracold atoms in optical lattices can model the solid-state systems of electrons in a crystal in the presence of applied fields. The force induced by an external field is necessary to observe phenomena like Bloch oscillations (these will be introduced in section 2.3). Such a force can be implemented easily in optical lattices by introducing an appropriate time dependence of the optical lattice, i.e., by a frequency difference between the two laser beams forming the lattice. A constant acceleration of the standing wave is generated by linearly chirping the frequency difference. An instantaneous frequency difference $\Delta\omega_L(t) = \omega_{L1} - \omega_{L2} = d\phi(t)/dt$ leads to

$$V(x,t) = V_0 \sin^2(k_L x - \phi(t)), \tag{2.29}$$

where the time-dependent phase $\phi(t)$ can be written as $k_L a t^2$ with a being the acceleration. Inserting Eq. (2.29) into the Hamiltonian given in Eq. (2.21) and applying a unitary transformation, one can transform the resulting Hamiltonian to the frame of reference accelerated with the above potential [21] and arrive at the following time-independent Hamiltonian

$$H = \frac{p^2}{2M} + V_0 \sin^2(k_L x) + Fx. \tag{2.30}$$

This Hamiltonian presents the so-called Wannier–Stark system (see section 2.4). The last term in the Hamiltonian is an inertial force $F = Ma$. It mimics the role of the interaction potential eEx between the electric field E and the electron of charge e in the crystals. This force is considered theoretically as a tilt of the optical lattice as seen in Figure 2.4. In the next chapter the spectrum of the Wannier-Stark system will be studied and the coherent phenomena resulting from this Hamiltonian will be introduced.

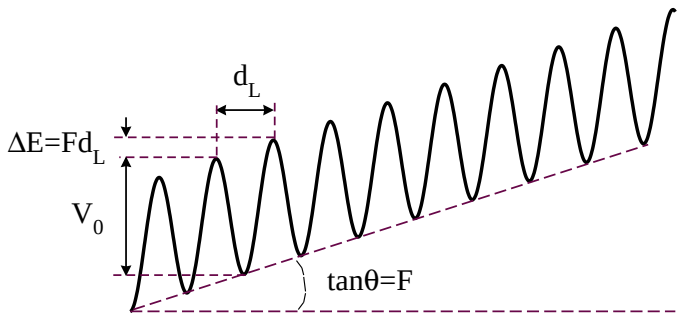

Figure 2.4: A tilted optical lattice (accelerated optical lattice). The lattice depth V_0, the lattice spacing d_L, and the Stark force F are defined in the text.

Another way to introduce a time-dependence of the optical lattice is by a time-periodic driving force. Technically, it is applied as a backwards and forwards motion of the periodic potential, which is equivalent to a periodic force applied to the atoms in the lattice. A sinusoidal motion of the lattice [83] can be introduced in the Hamiltonian as

$$H = \frac{p^2}{2M} + V_0 \sin^2(k_L x) + F x \cos(\omega t), \tag{2.31}$$

where F is the modulation amplitude as explained above and ω its frequency. Quantum particles tunneling between the sites of a periodic lattice can be made to slow down, stop or turn around by shaking the lattice back and forth [84]. These simple methods suggest a new kind of quantum control of cold atoms. The latter control mechanism has not been used in this thesis, however it is analogous to the time-dependent deterministic phase in the lattice as will be presented in section 3.2.3 and is later applied in section 6.5. The Hamiltonian in Eq. (2.31) is transformed by Kramers–Henneberger gauge to the one with the potential of Eq. (6.10) (see the appendix). The former control mechanism presented in Eq. (2.30) will be used as the reference system in this thesis. Our results will show how to control the transport of particles in tilted lattices by changing system characteristic parameters (see chapter 5) and also by introducing an appropriate time-dependence (see chapter 6).

2.3 Bloch oscillations

In solid–state physics, the temporal dynamics of an electron facing an electric field is a fundamental quantum-mechanical problem. The so-called acceleration theorem

$$\hbar\dot{\mathbf{k}} = e\mathbf{E} \tag{2.32}$$

expresses the quasimomentum $\mathbf{k}$ of an individual Bloch state varying linearly in time at a rate proportional to the electric field $\mathbf{E}$ [85]. Felix Bloch [85] predicted the dynamical behavior of electrons in a solid, subject to a uniform, static electric field. It was expanded later by Zener [86], whereby it was shown that electrons accelerated by an electric field in a periodic potential, under the right conditions, could oscillate. The frequency of oscillation is given by $\omega_{\mathrm{B}} = eEd_{\mathrm{L}}/\hbar$, where e is the electron charge, E is the electric field amplitude, d_{L} is the lattice constant. This phenomenon is known as Bloch oscillations.

Bloch oscillations have never been observed in natural crystals because the scattering time of the electrons at lattice defects is much shorter than the Bloch period. With the advent and refinement of semiconductor technology, it was possible to test the prediction of Bloch's proposal. In 1970, Esaki and Tsu [87] proposed using a semiconductor superlattice, which would provide the needed periodic structure on a scale large enough to detect Bloch oscillations. In fact, in semiconductor superlattices, the larger spatial period leads to a much shorter Bloch period. It was only in 1992 however, that Bloch oscillations and the associated Terahertz (THz) radiation were detected in semiconductor superlattices [19, 58]. Theoretically and experimentally it is now a well-established fact that the particle can perform Bloch oscillations [20, 21]. Recently, the first experimental observation of spectral Bloch oscillations in an optical fiber was reported [88]. In another recent work, it has been shown that localized and extended defects in the lattice can be engineered to be transparent for Bloch oscillations [89].

As mentioned in the previous section, for a periodic system, the solutions are known to be Bloch waves with the band structure (see below Figure 2.2). For a particle in a periodic potential $V(x)$ in the presence of a force F the time-dependent Schrödinger equation is given by

$$i\hbar\frac{\partial}{\partial t}\Psi(x,\,t) = \left(-\frac{\hbar^2}{2M}\nabla^2 + V(x) + Fx\right)\Psi(x,\,t). \tag{2.33}$$

It is assumed that the wave function has the following form

$$\psi(x,t) = \sum_{n,\,k} c_{n,\,k}(t)\psi_{n\,k}\,e^{-iE_n t/\hbar}, \tag{2.34}$$

and the time variation of the amplitude of the coefficients can be found as [85]

$$\frac{d}{dt}|c_{n,k}|^2 = -\frac{F}{\hbar}\frac{\partial}{\partial k}|c_{n,k}(0)|^2. \tag{2.35}$$

Later in 1933, Zener clarified Bloch's work in a paper studying the theory of electrical breakdown of solid dielectrics [86]. He stated that an electron under the influence of an electric field tends to become excited and oscillate instead of being totally freed from the solid. Using the Bloch model, he calculated the rate at which the electron moves from lower to upper energy bands in such a system. A particle confined to a single energy band will move in the opposite direction of the field until being reflected by the lattice, and then it moves in the opposite direction until it is stopped by the force, where it starts the same motion over again [86]. This periodic motion is characterized by a period

$$T_{\mathrm{B}} = 2\pi\hbar/Fd_{\mathrm{L}}, \tag{2.36}$$

where d_{L} is the spatial period of the system. Bloch oscillations in the time domain are related to the existence of a Wannier-Stark ladder in the frequency domain [90]. In addition, there is always a probability for a particle to go through a transition between the energy bands, the so-called Zener tunneling [86]. According to Zener's paper [86] a particle would undergo transitions between energy bands at the rate

$$\Gamma_n = \frac{Fd_{\mathrm{L}}}{2\pi\hbar}\, e^{-Md_{\mathrm{L}}\Delta E_n^2/4\hbar^2 F}. \tag{2.37}$$

where n indicates the Bloch band index and ΔE_n is the energy gap between n^{th} and $(n+1)^{\mathrm{th}}$ bands.

The tight-binding and single-band models allow an analytical study of the dynamics of Bloch oscillations and provide valuable insight. These models, in their simplest form, neglect the coupling between bands, i.e., Zener tunneling and only nearest neighbor coupling is taken into account [91]. In section 2.4, more details on the Wannier-Stark system will be presented and it will be also shown how this system was explained initially by the tight-binding and the single-band model. The weak point of these models in explaining the spectrum of a periodic system in the presence of a force will be addressed in the next section.

2.4 Wannier–Stark problem

The dynamics of a particle in a one-dimensional periodic lattice potential $V(x) = V(x + d_{\mathrm{L}})$ under the influence of a force is described by the so-called Wannier–Stark Hamiltonian

$$\hat{H} = -\frac{\hbar^2}{2M}\frac{d^2}{dx^2} + V(x) + Fx, \tag{2.38}$$

where F is the static force induced by the external field or by accelerating the lattice. The problem of describing the spectrum of the Wannier-Stark system is as old as the quantum theory of solids. There has been a long standing discussion about the properties of such systems [87, 92, 93, 94, 95, 96]. These discussions were initiated by the counter intuition predictions [85, 86] and by a difficulty to verify the predictions experimentally. The application of a force destroys the translational invariance of the periodic potential and causes a gradual localization of the initially delocalize Bloch states which is called Stark localization [92]. The so-called Wannier functions are in essence a Fourier transform of the Bloch states. Applying a force, the continuous density of states is transformed into a series of equally spaced - in energy and real space - ladder states with energies forming the Wannier–Stark ladder:

$$E_{n,m} = E_n + mFd_{\mathrm{L}}, \quad m = 0, \pm 1, \pm 2, \dots . \tag{2.39}$$

where $E_{n,m}$ are the energy levels, E_n is the mean energy of the band, and mFd_{L} are the ladder spacing intervals with m being the site index and n the band index. This implies that if there exists an eigenstate $\phi_n(x)$ with energy E_n, then the set of states corresponding to wavefunctions $\phi_{n,m}(x) = \phi_n(x - md_{\mathrm{L}})$ are eigenstates of the Hamiltonian with energies $E_{n,m}$. The ladder spacing is related to the Bloch oscillation period T_{B} and leads to what is called Stark ladders. This Wannier-Stark quantization was the subject of dispute. The discussions were focused mainly on the effect of the single band approximation on the spectral properties of the Wannier-Stark Hamiltonian.

Due to a short phase coherence time of an electron compared with the Bloch oscillation time (localization time), T_{B}, for all reasonable values of the electric field, the experimental observation of Bloch oscillations and Wannier-Stark ladders in realistic bulk solids is prevented. Scattering due to phonons, impurities, etc., and interband tunneling due to the virtual binding character of the Wannier–Stark states, are the limiting factors for the electron dephasing. The much larger period of superlattice allow a strong localization at much lower fields than in the bulk. Wannier–stark ladders were finally observed in semiconductor superlattices with various optical techniques [19, 97].

Today, we know that the process, which couples the bands and is neglected in the single band approximation, is the Zener tunneling [86]. The tunneling rate

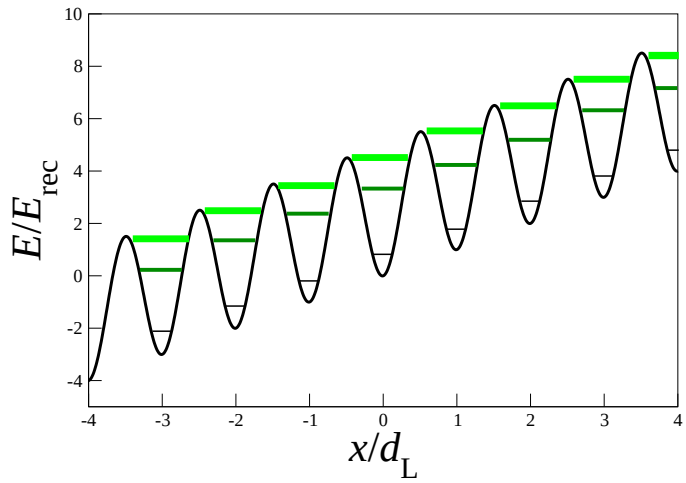

Figure 2.5: Schematic illustration of the Wannier-Stark ladders of resonances. The width of the lines indicate the width of the levels, i.e. their instability. The width of the levels is "proportional" to the resonance width Γ_n defining the lifetime of the states.

increases with decreasing band gap between the initial state and the final state and hence there is a large probability for the Bloch particle to tunnel to higher bands (see Zener's prediction given in Eq. (2.37)). As a result one can argue that the discrete spectrum given in Eq. (2.39) can only be an approximation. It was shown only in 1977 that the spectrum of a Bloch electron in an electric field is entirely continuous [93], which is a prerequisite of Zener tunnelings. Therefore, the Wannier-Stark ladders become resonances, i.e., nonstationary states with a long lifetime. In other words, if a system has a number of discrete levels (which are associated with classically bounded motion) followed by a continuous spectrum (associated with unbounded motion), after applying an electric field the discrete energy states become metastable. The decay time τ_{n} and the decay rate Γ_n of a metastable state are determined by the probability of tunneling through the potential barrier separating the region of classically bounded and unbounded motion. Therefore, Eq. (2.39) should be corrected

$$\mathcal{E}_{n,m} = E_n + mFd_{\mathrm{L}} - i\frac{\Gamma_n}{2}, \tag{2.40}$$

where the index n refers to the Wannier-Stark states originating from the nth Bloch band, i.e., $n = 0$ indicates the ground level. The eigenstates, $\psi_{n,m}(x)$, of the Hamiltonian given by Eq. (2.38) corresponding to these complex energies, are metastable states. The lifetime of metastable states is given by $\tau_n = \hbar/\Gamma_n$ [98]. Figure 2.5 shows a schematic illustration of the potential $V_0 \sin^2(k_L x) + Fx$. The

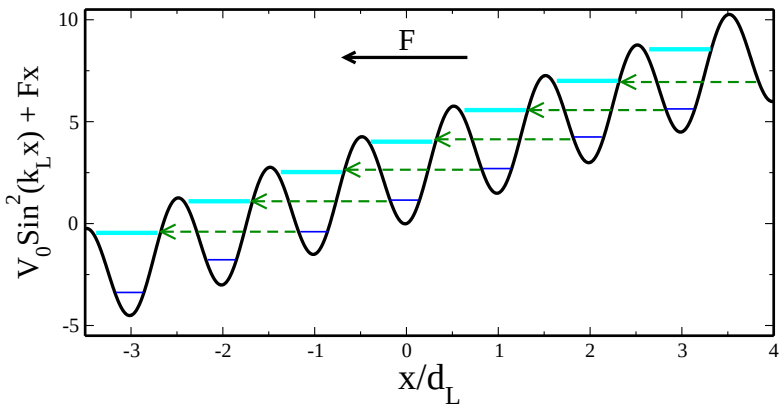

Figure 2.6: Schematic view of the resonantly enhanced tunneling (RET) process between second nearest neighbouring wells, i.e., for $m = 2$ shown by green arrows.

positions of the lowest three Wannier-Stark ladders are marked by lines whose thickness denotes the increasing width (the decreasing lifetime).

Recent Experimental and numerical calculations [41, 99, 100, 101, 102] demonstrate resonances which cannot be explained by Zener's semiclassical theory. These resonances are related to interactions ("anticrossings" or "avoided crossings") of Wannier–Stark ladders. Anticrossings of Wannier–Stark ladders have been observed in the optical spectra of superlattices without a direct connection made to Zener tunneling [103, 104]. In fact, Zener tunneling requires an entirely continuous spectrum and, therefore, cannot be explained on the basis of discrete Wannier-Stark ladders. In section 3.1, the Landau–Zener tunneling phenomenon will be described which is the key to the imaginary part of the Wannier-Stark spectrum and hence the lifetime of the Wannier–Stark states.

2.4.1 Resonantly enhanced tunneling

Additional electromagnetic fields, as in the case of the spectroscopy of Wannier-Stark levels [105], or quantum tunneling between the bands give rise to interband transitions. The uncoupled energy bands are coupled by an additional force, which can be a static Stark force (tilting the periodic lattice as seen in Figure 2.5) [27], and the tunneling process can occur. The so-called Landau–Zener tunneling theory will be explained in section 3.1 in the next chapter. Increasing the tilting force, as expected from Eq. (2.37), leads to more and more tunneling of the atoms from the ground band. On the other hand, depending on the system parameters, one can tune into a special condition for which the rate of the tunneling is enhanced or suppressed.

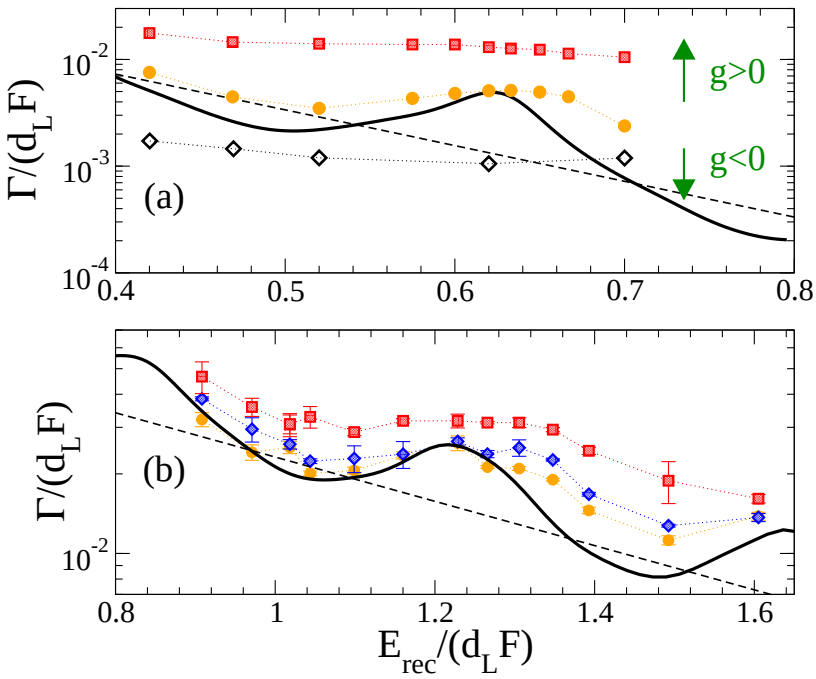

Figure 2.7: Resonant tunneling for $m = 2$ in the linear and nonlinear regimes. The solid lines are the theoretical prediction for the linear system. Globally the rates follow an exponential law (dashed lines) given in Eq. (2.37). Locally, due to RET peaks a clear deviation is seen of the solid line from the dashed line. (a) Numerical results for $V_0 = 5\,E_{\rm rec}$ with $C = -0.31$ (diamonds), $C = 0$ (solid line), $C = 0.065$ (stars), $C = 0.31$ (squares) [36]; (b) Experimental results for $V_0 = 2.5\,E_{\rm rec}$ with $C = 0.024$ (squares), $C = 0.035$ (circles) and $C = 0.057$ (triangles) [37]. The dimensionless nonlinear coupling constant $C = gn_0/8E_{\rm rec}$ was introduced in section 2.5. Results from [36, 37] are reproduced by courtesy of the corresponding authors.

The enhancement occurs when an integer multiple of the energy scale of the tilting force $Fd_{\rm L}$ matches the energy difference between the initial state and the final state, i.e., approximately the band gap ΔE. This phenomenon has been observed experimentally [37, 38] and is called resonantly enhanced tunneling (RET). It is possible to control Landau–Zener tunnelings of Bose–Einstein condensates from the ground band in the linear system (as defined in Eq. (2.12) with $g = 0$) by exploiting resonantly enhanced tunneling between degenerate Wannier–Stark states at $\Delta E \approx mFd_{\rm L}$ with m being an integer number [25]. A schematic representation of resonantly enhanced tunneling is shown in Figure 2.6.

In a tilted periodic lattice, atoms can tunnel from the energy band in which they have been initially prepared, to the next energy band and then escape to the continuum by successive tunneling across the much smaller band gaps between

the upper bands. The tunneling rate Γ_{LZ} can be calculated using the Landau–Zener formula of Eq. (2.37). A deviation from the Landau–Zener prediction is expected in the case when two Wannier–Stark levels in different potential wells are coupled, building upon the degeneracy as seen in Figure 2.6. Under such condition, the tunneling probability can be enhanced over the Landau–Zener prediction and the results can be seen by the black solid line in Figure 2.7. The resonantly enhanced tunneling phenomenon leads to a faster decay of the Wannier states trapped in the potential wells.

The nearly perfect control on the experimental parameters such as lattice depth, interaction strength, and the flexibility to prepare the condensates with arbitrary initial conditions make it possible to measure the RET decay of the ground band in a wide range of experimental conditions. The impact of atom-atom interactions and a loss of coherence on the RET process has been studied in [37]. As seen in Figure 2.7, the tilting force F is scanned to study the impact of the atom-atom interaction on RET, for which the standard Landau–Zener prediction is modified even in the absence of interactions [25]. The numerical [36] and the experimental results [37] demonstrate that repulsive atom-atom interactions increases the decay rate, hence the overall enhancement of the decay rate. Attractive atom-atom interaction, however, as seen by black diamond symbols in upper picture in Figure 2.7, suppresses the decay rate [36]. The effect of non-linearity (atom-atom interactions) on the tunneling probability can be explained by the effective model defined by Niu [39]. This model will be presented in the next section.

2.5 Tunneling in the presence of nonlinearity

The Gross–Pitaevskii equation can be used to simulate the dynamics of an interacting gas of ultracold atoms in the presence of a one-dimensional optical lattice. A Bose-Einstein condensate is prepared inside a long cigar shaped harmonic trap and then loaded adiabatically into the one-dimensional optical lattice. The density profile in the transverse directions is held fixed by the trap while the motion along the longitudinal direction can be considered free. Hence for a non-interacting ultracold atomic gas, one can easily model the motion as a quasi-one-dimensional problem. Taking into account the atom-atom interactions brings about the nonlinear term $N_0 g|\phi(\mathbf{r})|^2$, mixing the three coordinates of the system and hence the eigenstate can no longer be written as a product of three functions. The ground state of the condensate in such a system can be found by solving the following three-dimensional Gross-Pitaevskii equation

$$\mu\phi(\mathbf{r}) = \left(-\frac{\hbar^2}{2m}\nabla^2 + V_{trap}(\mathbf{r}) + V_0 \sin^2(k_{\mathrm{L}}x) + gN_0|\phi(\mathbf{r}|^2\right)\phi(\mathbf{r}), \tag{2.41}$$

where $V_{\mathrm{trap}}(\mathbf{r}) = \frac{m}{2}\left(\omega_{\mathrm{x}}^2 x^2 + \omega_{\mathrm{y}}^2 y^2 + \omega_{\mathrm{z}}^2 z^2\right)$ is the harmonic trap potential. However, to gain insight into the physics of a system of interacting ultracold atoms in a one-dimensional optical lattice, one can introduce an effective potential which can explain the strong dependence of the condensate state on the nonlinearity [39]. An explicit analytical expression for the effective potential can be calculated using perturbation theory. The effective potential amplitude reads [39]

$$V_{\mathrm{eff}} = \frac{V_0}{1+4C}, \tag{2.42}$$

where $C = gn_0/8E_{\mathrm{rec}}$ is a dimensionless coupling constant with n_0 being the peak density of a Bose-Einstein condensate (see the density profile $n(\mathbf{r})$ definition in section 2.1.1). The lattice depth V_0 is expressed in units of the recoil energy $E_{\mathrm{rec}} = \hbar^2 k_{\mathrm{L}}^2/2M$, where $\hbar k_{\mathrm{L}}$ is the recoil momentum. The dimensionless coupling constant C can be negative or positive depending on the sign on a_{s} for attractive or repulsive atom-atom interactions.

Starting from the Gross–Pitaevskii equation given in Eq. (2.41) for the condensate wave function in a one-dimensional optical lattice, one substitute the potential depth V_0 with the effective potential given in Eq. (2.42), thus providing a potential approximate resolution of the effect of the mean-field interaction could be approximately resolved. This effective potential has some validity limits for the potential and/or nonlinearity strength C [106]. It is expected that this expression will be valid as long as the condensate density remains nearly uniform i.e., when $V_{\mathrm{eff}} \ll 1$. This condition is realized for either a weak external potential

or a strong atomic interaction [39]. The relevant energy gap between the lowest two bands at the same Bloch number is modified due to the interaction and can be evaluated considering the effective potential.

The Landau-Zener tunneling probability as given in Eq. (3.4) is affected due to nonlinearity. Using the effective potential one can predict the effect of interaction on the tunneling probability. As seen in for the data shown in Figure 2.7 the repulsive interaction $C > 0$ leads to an overall enhancement of the decay rate since $V_{\text{eff}} < V_0$ and hence the effective band gap $\Delta E_{\text{eff}} \approx V_0/(2+8C)$ is smaller and results to more tunnelings of the condensate atoms. The attractive interaction $C < 0$, however, as seen in Figure 2.7 by diamond symbols, the decay rate is suppressed since the interaction leads to larger effective band gap ($V_{\text{eff}} > V_0$). This theory is not valid for the RET condition, where the peaks appear on top of the decay rate. The reason is that the landau–Zener theory cannot predict the enhancement of the tunneling rate which happens at RET condition (i.e., $\Delta E \approx mFd_{\text{L}}$, with $m \in \mathbb{N}$). For the derivation of the Landau–Zener transition rate Eq. (2.37), only the "band structure" is taken into account, while the Wannier-Stark states (levels) have not been considered. The RET condition, however, corresponds to Wannier-Stark levels, therefore, the exponential decay rate predicted by Eq. (2.37) does not hold for the RET condition. As presented in the previous section, the RET condition can be described within the Wannier–Stark problem.

When the interatomic interaction is repulsive, and the Thomas–Fermi condition is satisfied (i.e., when $N_0|a_{\text{s}}|/a_{\text{ho}} \gg 1$) an analytical expression for the dimensionless coupling constant C can be gained. For a Bose–Einstein condensate in a three-dimensional harmonic trap, with $\bar{\omega} = (\omega_x\omega_y\omega_z)^{1/3}$, from Eqs. (2.15) and (2.17) one gets

$$C = \frac{\hbar}{16E_{\text{rec}}}\bar{\omega}\left(15N_0a_{\text{s}}\right)^{0.4}\left(M\bar{\omega}/\hbar\right)^{0.2}. \tag{2.43}$$

This quantity can be used to estimate the repulsive interaction strength between the atoms in the system of Bose–Einstein condensate trapped by a harmonic potential. In section 5.5 the quantity C and the effective potential given in Eq. (2.42) are used to quantify the atom-atom interaction strength and to interpret the results given in Figure 5.15.

Chapter 3

Models under consideration

3.1 Landau–Zener model

As mentioned in the previous chapter, quantum tunneling is an essential phenomenon which is involved in explaining the resonance states as well as the Wannier–Stark spectrum. In quantum mechanical systems with two discrete energy levels, there is a possibility of a transition if the degeneracy is lifted by a coupling and the system is forced across the avoided crossing by varying the parameter determining the level separation. This phenomenon is known as Landau–Zener tunneling. According to Landau–Zener theory[1], transitions are possible between two approaching levels when a control parameter is swept across the point of minimum energy separation. The phase accumulated between the incoming and outgoing passages varies with, e.g., the collision energy, giving rise to Stückelberg oscillations in the populations [5]. As a basic physical process, it has found wide applications in various systems, such as current driven Josephson junctions [10], atoms in accelerating optical lattices [17, 22, 27, 35, 107, 108], field-driven superlattices [109], and in interferometry for qubits and solid-state artificial atoms [110, 111].

For a large enough acceleration (field) of the periodic potential, the semiclassical equations no longer hold and inter-band tunneling can occur. The atoms can leave the trapping potential via tunneling into the continuum of free states. The transition probability will increase as the acceleration is increased. This can be described in simple terms relating to the Heisenberg uncertainty principle. This process is similar in many avoided-crossing problems. The transition probability between levels becomes significant when the time that the atom spends

[1] Landau–Zener theory was developed in the early 1930's in the context of atomic scattering processes and spin dynamics in time-dependent fields [3, 4, 5, 6]

near the band gap becomes comparable to the the inverse energy gap,i.e.

$$\Delta E \cong \frac{\hbar}{\Delta t}. \tag{3.1}$$

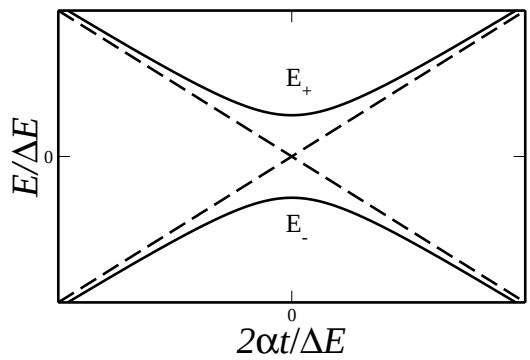

Figure 3.1: Energy levels as a function of time. The dashed lines show the so-called diabatic levels, i.e., the energies of states in the absence of the interaction. The solid lines demonstrate the so-called adiabatic levels, i.e., the eigenstates of the system corresponding to the instantaneous Hamiltonian.

In its basic form the Landau–Zener problem can be described by a two-state model and allows an eloquent expression for the transition probability. The Landau–Zener Hamiltonian for a single crossing taking place at time $t = 0$ can be written as the following 2 by 2 matrix

$$H_{\mathrm{LZ}} = \begin{pmatrix} \alpha t & \Delta E/2 \\ \Delta E/2 & -\alpha t \end{pmatrix} . \tag{3.2}$$

The off-diagonal term, $\Delta E/2$, is the coupling between the two states and α is the rate of change of the energy levels in time. The dynamics of the system can be measured in different bases, diabatic and adiabatic. The diabatic basis is the eigenbasis of the bare states of Eq. (3.2) when there is no off-diagonal coupling. The adiabatic basis, on the other hand, is the basis of a system with a finite $\Delta E/2$ coupling between the two states. The Hamiltonian has two adiabatic energy levels

$$E_{\pm} = \pm\frac{1}{2}\sqrt{(2\alpha t)^2 + \Delta E^2}. \tag{3.3}$$

Assuming the system initially at $t \to -\infty$ to be in the ground energy level E_-, should the sweeping rate be small enough, it will be exponentially likely that the system remains in its adiabatic ground state E_- at $t \to +\infty$. The limiting value

of the adiabatic Landau–Zener survival probabilities (for t going from $-\infty$ to $+\infty$) is,

$$P_{\mathrm{a}}(\infty) = 1 - \exp\left(-\frac{\pi}{\gamma}\right), \tag{3.4}$$

where a dimensionless parameter, the so called adiabaticity parameter $\gamma = 4\hbar\alpha/\Delta E^2$ is introduced [41]. The above probability gives the probability to remain the initial state while Eq. (2.37) gives the rate of transition to higher bands and hence the decay rate of the initial state. This survival probability is valid for both E_- and E_+ initial states, and the same equation is valid for the diabatic case. A small adiabaticity parameter corresponds to a small velocity of the state displacement along the energy scale compared to ΔE^2, such that the system follows the adiabatic trajectory of Figure. 3.1. Thus, there is a large coupling between the diabatic states and at the avoided crossing at $t = 0$ an almost complete transition from the initial diabatic state to the final diabatic state takes place. On the other hand, for a large value of the adiabaticity parameter γ, the coupling between the two states is small and consequently the system remains in its initial state following the diabatic trajectories of Figure. 3.1.

Later in chapter 5, the connection between the Landau-Zener model with our system of ultracold atoms in tilted optical lattices will be demonstrated. It will be explained how our system can be reduced to this simple model and what the limits are for such an approximation.

3.1.1 Transition times in the Landau-Zener model

A careful study of the transition from an initial state to a final state can reveal the time required to complete the transition. Moreover, in the case of multiple level crossings, as in [42, 43], it is necessary to know whether a transition has been completed before the next avoided crossing. The Landau–Zener approach may be applied when a transition between two coupled quantum states takes place in a small time interval around the avoided crossing and successive crossings are independent from each other.

Analytical estimates for the Landau–Zener transition times have been derived in [24, 40] using the two-state model of Eq. (3.2). In a given basis, e.g., adiabatic or diabatic, different transition times are obtained. Vitanov [40] calculated the time-dependent diabatic/adiabatic survival probability at finite times. The Landau–Zener transition times were derived in [24] using some exact and approximate results for the transition probability. Vitanov assumed a real and constant coupling between the two states and a time-dependent detuning frequency (the difference between the system transition frequency and the field frequency) as introduced in the Landau-Zener model in (3.2). He calculated the

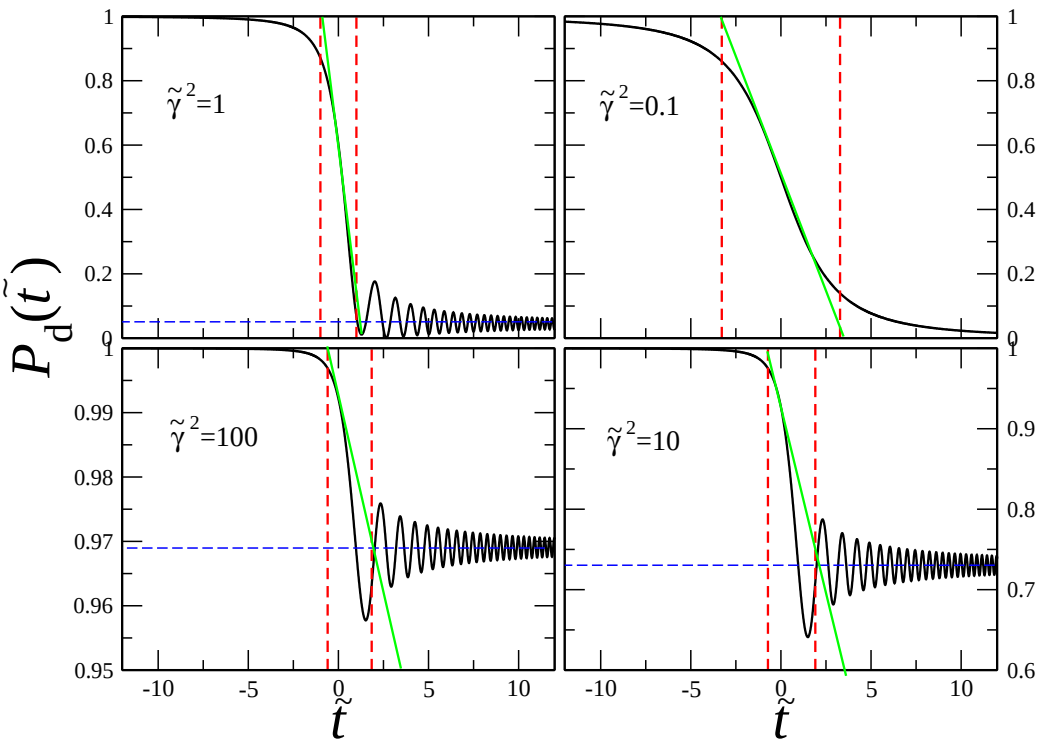

Figure 3.2: The time evolution of the survival probability in the diabatic basis $P_{\mathrm{d}}(\tilde{t})$ (thick black curve) – done as described in [40] – for four values of the coupling ω specified in each picture. The horizontal blue dashed line shows the asymptotic value $P_{\mathrm{d}}(\infty)$. The two vertical red dashed lines display the jump region, whose beginning is defined by the crossing of the tangent to $P_{\mathrm{d}}(\tilde{t})$ at $\tilde{t} = 0$ (shown by the slanted green solid line) with the line of $P_{\mathrm{d}}(\tilde{t}) = 1$, whereas its end is defined by the crossing of the tangent with the asymptotic line [40].

time evolution of this coherently driven two-level quantum system by solving the Schrödinger equation for Eq. (3.2). The survival probability of the initial state based on Vitanov's calculations in the diabatic and the adiabatic bases [24, 40] are demonstrated in Figures 3.2 and 3.3, respectively. These probabilities have been calculated for several values of $\gamma = 4\hbar\alpha/\Delta E^2$ as defined in the previous section. The survival probability in the diabatic basis is plotted versus a dimensionless time $\tilde{t} = \alpha^{1/2}t$. In the adiabatic basis, it is plotted against a rescaled time $\tilde{t}\,(\gamma/\hbar)^{1/2}$. For convenience a new parameter $\tilde{\gamma} = (\gamma/\hbar)^{1/2}$ is introduced.

The Landau–Zener jump time in a given basis can be defined as the time after which the transition probability reaches its asymptotic value. From this definition one can expect to observe a step-like structure, with a finite width, in the time-resolved tunneling probability, as will be seen also in our results in

chapter 5. As will be seen for our results as well as for the transition probability derived by Vitanov [40] (as shown in Figures 3.2 and 3.3), the step is not very sharp, therefore it is not straightforward to define the initial and final times for the transition. It is even less obvious as to how one defines the jump time for both small and for large coupling. Some possible choices have been used by Lim and Berry in [112] and by Vitanov in [24, 40]. The problem is even more complicated when the survival probability of the condensate in the ground band shows an oscillatory behavior on top of the step structure. Such oscillations can be seen in Figures 3.2 and 3.3 for some values of $\tilde{\gamma}$ and also in Figure 5.13 in chapter 5, which shows experimental and numerical results for a single Landau–Zener transition measured in the adiabatic basis (the numerical and experimental methods will be described in the corresponding chapter). The oscillations give rise to other time scales, namely the oscillation time and the damping time of the oscillations appearing in the transition probability after the crossing. Therefore, a measurement of the tunneling time depends very much on how these times are defined and also which basis is considered.

In [40], the jump time in the diabatic/adiabatic bases is defined as

$$\tau_{\mathrm{d/a}}^{jump} = \frac{P_{\mathrm{d/a}}(\infty)}{P'_{\mathrm{d/a}}(0)}, \tag{3.5}$$

where $P_{\mathrm{d/a}}$ is the transition probability between the two diabatic/adiabatic states respectively. $P'_{\mathrm{d/a}}(0)$ denotes the time derivative of the tunneling probability evaluated at the crossing point. The diabatic jump time $\tau_{\mathrm{d}}^{jump} \approx \sqrt{2\pi\hbar/\alpha}$ is almost constant for large values of the adiabaticity parameter γ [40]. Instead, for $\gamma \ll 1$ it decreases with increasing γ, $\tau_{\mathrm{d}}^{jump} \approx 2\sqrt{\hbar(\gamma\alpha)^{-1}}$ [40]. In the adiabatic basis, when γ is large the transition probability resembles the one of the diabatic basis with an equal jump time. For a small adiabaticity parameter, because of the oscillations appearing on top of the transition probability step structure, it is not straightforward to define the initial and the final time for the transition. Vitanov [40] defines the initial jump time as the time $\tilde{t} < 0$ at which the transition probability is very small (i.e., $P_{\mathrm{a}}(\tilde{t}) = \varepsilon P_{\mathrm{a}}(\infty)$, where ε is a proper small number). The final time of the transition $\tilde{t} > 0$ is defined as the time at which the non-oscillatory part of $P_{\mathrm{a}}(\tilde{t})$ is equal to $(1+\varepsilon)P_{\mathrm{a}}(\infty)$. Using these definitions, Vitanov derived that the transition time in the adiabatic basis depends exponentially on the adiabaticity parameter [40]:

$$\tau_{\mathrm{a}}^{jump} \approx (4/\varepsilon)^{1/6}\, \gamma^{-1/6} e^{\pi/(6\gamma)} \sqrt{\hbar/\alpha} \tag{3.6}$$

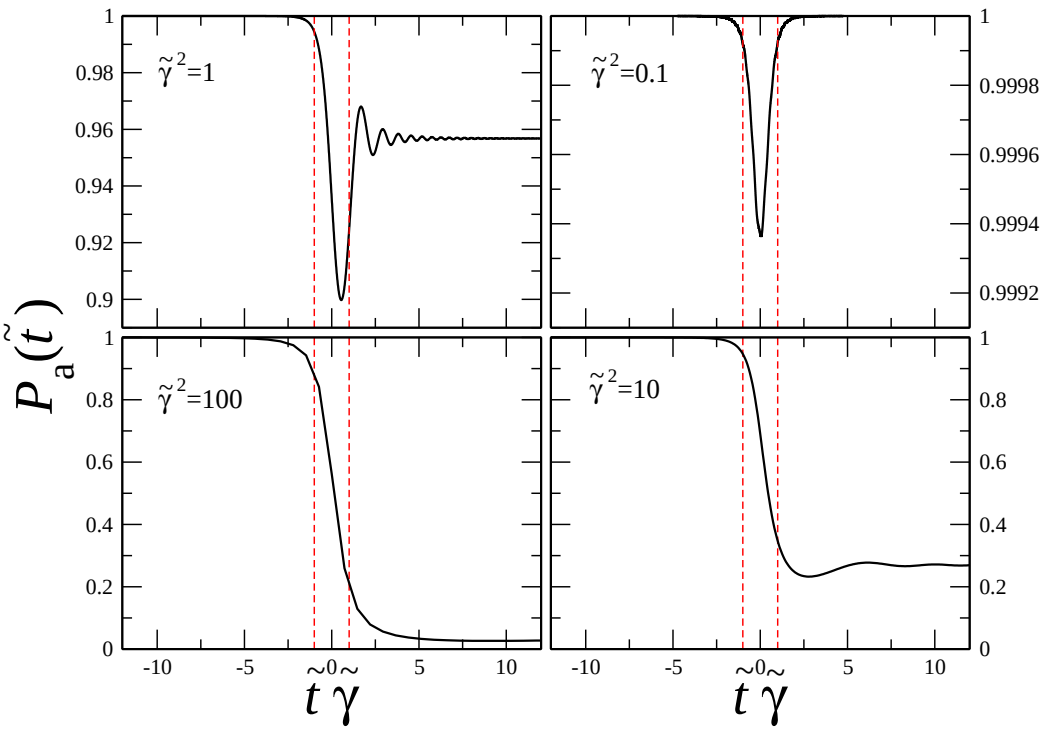

Figure 3.3: The time evolution of the survival probability in the adiabatic basis $P_{\rm a}(\tilde{t})$ (thick black curve) – done as described in [40] – plotted against the scaled time $\tilde{t}\tilde{\gamma}$ for the same four values of the coupling ω specified in each picture, as in Figure 3.2. The two vertical red dashed lines display the interval $-1 \leq \tilde{t}\tilde{\gamma} \leq 1$, which provide approximately the jump region [40].

According to the transition probability from the initial state that Vitanov calculated in diabatic and adiabatic bases [40], whose corresponding plots are seen in Figures 3.2and 3.3, the amplitude of the oscillations in $P_{\rm d}(\tilde{t})$ vanishes as $\tilde{t}^{-1}$ at large times. The relaxation time τ_d^{relax} can be defined as the time it takes to damp the oscillation amplitude to the (small) value $\varepsilon P_{\rm d}(\infty)$, where $\varepsilon \ll 1$. Therefore the relaxation time in the diabatic basis is given by

$$\tau_d^{relax} \approx \left(\frac{\hbar(\gamma\alpha)^{-1}}{\varepsilon^2(e^{\pi/\gamma})} - \hbar(\gamma\alpha)^{-1} \right)^{1/2}. \tag{3.7}$$

In the adiabatic basis, however, at large positive times the amplitude of the oscillations, that appear in $P_{\rm a}(\tilde{t})$ after crossing vanishes as $\tilde{t}^{-3}$. The relaxation time is defined in the same way as in the diabatic basis and for large and small

adiabaticity parameter γ, and it is approximated by

$$\tau_a^{relax} \approx \begin{cases} \left(\frac{\pi}{4\varepsilon^2}\right)^{1/6} \gamma^{-1/3} \sqrt{\hbar/\alpha} & (\gamma \gg 1) \\ \left(\frac{1}{2\varepsilon}\right)^{1/3} \gamma^{-1/6} e^{\pi/(6\gamma)} \sqrt{\hbar/\alpha} & (\gamma \ll 1) \end{cases} \tag{3.8}$$

Comparing Eq. (3.7) and Eq. (3.8) for large adiabaticity parameter, one sees that $\tau_d^{relax} \gg \tau_a^{relax}$. This can be explained by the fact that the oscillation amplitude of $P_{\mathrm{a}}(\tilde{t})$ vanishes as $\tilde{t}^{-3}$, i.e., much faster than $P_{\mathrm{d}}(\tilde{t})$ which vanishes as $\tilde{t}^{-1}$. For small adiabaticity γ, $\tau_a^{relax} \ll \tau_d^{relax} \approx 0$, which follows from the fact that the reference value in the diabatic basis is $P_{\mathrm{d}}(\infty) = e^{-\pi/\gamma} \approx 1$, whereas the reference value in the adiabatic basis is $P_{\mathrm{a}}(\infty) = 1 - e^{-\pi/\gamma} \ll 1$.

3.2 Noise algorithms

As mentioned in section 2.2.3, one possibility to create a disordered potential is provided by using bichromatic optical lattices with incommensurate lattices constants. An additional way was proposed, at the end of section 2.2.3, to create a spatially and temporally random potential, namely by adding a time-dependent stochastic phase difference $\phi(t)$ between the two lattices [44]. This random phase can be produced by different noise generators. Noise can be described by stochastic differential equations and there are various numerical algorithms for the integration of stochastic differential equations [113]. A time-dependent random phase $\phi(t)$ is characterized by its spectral distribution

$$S(\omega) = \frac{1}{2\pi} \int_{-\infty}^{\infty} dt\ e^{-i\omega t} \langle \phi(t)\phi(0) \rangle, \tag{3.9}$$

where the average $\langle \cdot \rangle$ is an integral over time for a sufficiently large time, i.e., $\langle \cdot \rangle = 1/T \int_0^T \cdot\, dt$. The noise fluctuations are described by the autocorrelation function of the noise

$$\langle \phi(t)\phi(s) \rangle \propto \gamma\left(|t-s|\right), \tag{3.10}$$

where $\gamma\left(|t-s|\right)$ is a general correlation function which is specified for each type of noise. Knowing the spectral distribution and the correlation function, one can distinguish different regimes of noise parameters and study how they can affect physical systems.

In this section, a few different noise generators (which are used as a time-dependent random phase for the secondary lattice in chapter 6) are introduced. In the following, an ideal type of noise, the so-called white noise, will be presented which is used as the basis of some random number generators. This leads us to a more realistic type of noise, the so-called colored noise, which can have interesting impact on the physical systems. The terms "white" noise and "colored" noise are, of course, jargon words. Nevertheless, it is common to use them since they are widely recognized and understood.

White noise vs. Colored noise

Initial studies of the fluctuations in physical systems concentrated on the effect of Gaussian white noise as an external noise which generates fluctuations in the system. In the frequency analysis, white noise is a uniform mixture of random energy at every frequency, this is of course a purely theoretical construction. The correlation function of the white noise is given by

$$\langle \xi(t)\xi(s) \rangle = 2D\delta\left(|t-s|\right), \tag{3.11}$$

where $\xi(t)$ is the Gaussian white noise with zero mean and the standard deviation of the noise equals one and D is the noise intensity. This noise has no time scale.

The white noise approximation, which dates back to the work of Einstein [114] and Smoluchowski [115] is of course an idealization and is never exactly realized in the physical world, not least because of its spectral distribution

$$S_{\mathrm{WN}}(\omega) = \frac{D}{\pi}, \tag{3.12}$$

which is flat and hence the total noise power is infinite for a finite characteristic noise intensity D, i.e., there is energy available for all frequencies. A large body of literature on white noise applications exists [116].

In order to consider the noise and the physical system within which it is operating together, the time scales of the two systems must be taken into account. Therefore, we seek a noise with a well-defined characteristic time. It is important to understand what time scale is being used to measure the correlation time of the noise. It is the physical system itself, which is either generating the noise internally or is subjected to the noise as an external forcing, which according to its own characteristic response time, defines the time scale of the noise. The comprehension of realistic noise sources with a finite correlation time in modeling dynamical systems has been attracting growing interest over the last few decades [117].

Somewhat more realistic for experiments is a noise with a finite correlation time of its fluctuations i.e., the mean-square value $\langle\phi^2(t)\rangle$ is finite. For such a noise, the spectral distribution $S(\omega \to \infty)$ falls to zero, implying that $S(\omega)$ is a frequency dependent function, hence the term colored noise. The function $\phi(t)$ represents a noise with a finite correlation time. They are created using the Gaussian white noise $\xi(t)$. The colored noise $\phi(t)$ is considered stationary and Gaussian distributed colored noise with zero mean and a correlation function $\langle\phi(t)\phi(s)\rangle$. In the following two types of colored noise with a finite correlation time are presented.

3.2.1 Exponentially correlated noise

A standard example of time-correlated noise is the Ornstein-Uhlenbeck process [118], the so-called exponentially correlated noise, which is characterized by a single correlation time. Such a noise can be written in terms of linearly filtered white noise as follows

$$\dot{\phi} = -\frac{\phi}{\tau} + \frac{\sqrt{2D}}{\tau}\xi(t), \tag{3.13}$$

where ξ is the white Gaussian noise with zero mean, the standard deviation is one and τ is the correlation time of the noise. The strength of the noise is given

by the parameter D. The introduced noise has a zero mean $\langle\phi(t)\rangle = 0$ and exhibits an exponential correlation function

$$\langle\phi(t)\phi(s)\rangle = \frac{D}{\tau}\, e^{-|t-s|/\tau}. \tag{3.14}$$

The time-scale of the fluctuations is described by τ, and its variance by D/τ. This fluctuation is called "colored noise" in analogy with the effects of filtering on white light. The spectral distribution is given by a Lorentzian with corner frequency $1/\tau$ as follows

$$S_{\mathrm{ECN}}\,(\omega) = \frac{D}{\pi(1+\omega^2\tau^2)}. \tag{3.15}$$

Such a spectrum has its maximum at zero frequency, with the amplitude $S(\omega = 0) = D/\pi$ (see the red curve in Figure 3.4). The inflection points of this Lorentzian function are at $\omega = \pm 1/\sqrt{3}\tau$ by which one can estimate the half width of the peak at zero frequency.

Different regimes of parameters

Considering the correlation time τ of the noise, two regimes can be defined for this Ornstein-Uhlenbeck noise [118]: (i) the regime of fast noise with a small correlated time τ, and (ii) the regime of slowly varying noise with a large correlation time τ.

It is crucial to understand how one can measure the noise correlation time. In order to successfully apply these theories to any real physical system, it is essential to know what "small" and "large" mean. According to what was initially discussed, the above introduced regime (i) actually means that the correlation time of the noise τ is much smaller than the time scale τ_{s} of the system under consideration and the regime (ii) just means the opposite limit of (i), i.e., $\tau \gg \tau_{\mathrm{s}}$.

It is often justified to assume that the random forces induced by noises are correlated on a very small time scale τ compared to the characteristic relaxation time for the system τ_{s}, around a locally stable state. An idealized treatment then assumes the random phase to have zero correlation time, i.e., $\tau \to 0$. In the limit that $\tau \to 0$, the noise $\phi(t)$ is approximated by a generalized δ-correlated (i.e., uncorrelated) process:

$$\langle\phi(t)\phi(s)\rangle = D/\tau\, \delta(t-s), \tag{3.16}$$

which is the definition of the white noise. Therefore, the Gaussian white noise can be recovered in the limit of vanishing correlation time of the Ornstein-Uhlenbeck noise. In this limit, all the frequencies of the power spectrum

$$\int_{-\infty}^{\infty} dt\; e^{-i\omega t}\langle\phi(t)\phi(0)\rangle \equiv D/\tau, \tag{3.17}$$

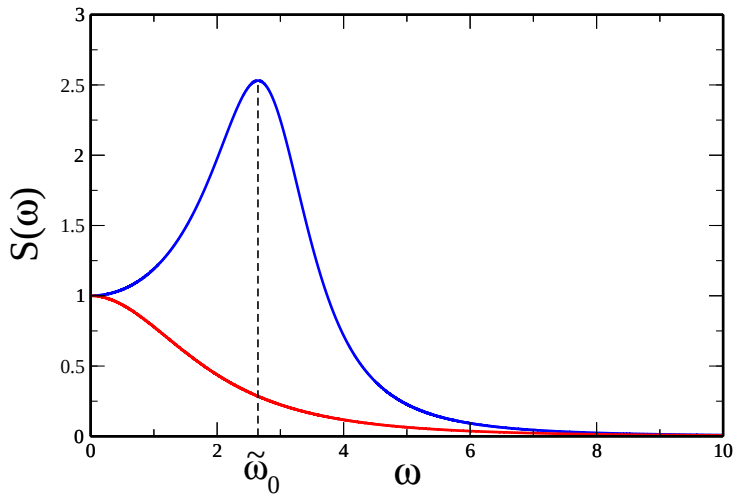

Figure 3.4: A schematic view of the corresponding spectral distributions of exponentially correlated noise given by Eq. (3.15) (red curve) and harmonic noise given by Eq. (3.24) (blue curve) are shown for noise parameters that set $S(\omega = 0)$ the same for both spectral distributions. The parameter $\tilde{\omega}_0$ shows the peak frequency, given within the text in section 3.2.2, for the spectral distribution of harmonic noise

are present with equal weight. This assumption considerably simplifies the problem, because it allows one to treat the dynamics within the notion of Markov processes. In the physical world however, as previously mentioned, this idealization is never exactly realized.

The other regime of the exponentially correlated noise is defined when $\tau \gg \tau_{\rm s}$. In this regime the fluctuations of the noise are very slow compared to the time scale of the system, and therefore, it can be considered as a constant. Considering $\tau \gg \tau_{\rm s}$, the correlation function now reads

$$\langle \phi(t)\phi(s)\rangle = D/\tau, \tag{3.18}$$

which is a constant and therefore, the power specrum of the noise in this limit of $\tau \gg \tau_s$ can be written as

$$\int_{-\infty}^{\infty} dt\; e^{-i\omega t}\langle \phi(t)\phi(0)\rangle \equiv \frac{D}{\tau}\,\delta(\omega). \tag{3.19}$$

The impact of such a noise in its different limits on the transport of ultracold atoms in the system under consideration will be shown in chapter 6-section 3.2.1. These two introduced limits are very good benchmarks which help us to understand our results.

3.2.2 Harmonic noise

Another type of colored noise can be presented by using a noisy damped oscillator. This type of colored noise, on the one hand, generalizes the Ornstein-Uhlenbeck process and on the other hand allows the consideration of resonance phenomena. The simplest type, as mentioned above, can be produced by a harmonic oscillator of frequency ω_0 and damping frequency Γ, driven by a Gaussian white noise. This noise is called harmonic noise [119] and gives rise to a more interesting spectral distribution which peaks at a finite frequency as will be shown in the following. The harmonic noise is represented by a two dimensional Gauss-Markov process taking the form of the following stochastic differential equations for $\phi(t)$

$$\dot{\phi} = \nu \tag{3.20a}$$

$$\dot{\nu} = -2\Gamma\nu - \omega_0^2\phi + \xi(t), \tag{3.20b}$$

where Γ and ω_0 are the characteristic parameters of the noise, and have the dimension of frequency. $\xi(t)$ is the Gaussian white noise with

$$\langle\xi(t)\rangle = 0, \quad \langle\xi(t)\xi(s)\rangle = 4\Gamma T\delta(t-s). \tag{3.21}$$

The parameter T is a measure for the noise strength and expressed in the unit of frequency squared. In the white noise limit, through the fluctuation dissipation theorem, the parameter T is related to temperature.

The properties of a white noise driven harmonic noise are known from the works of of Chandrasekhar [120] and Wang and Uhlenbeck [121]. The stationary distribution of the harmonic noise reads [122]

$$P(\phi,\nu) = N^{-1}\exp\left(-\frac{2\Gamma}{|\xi|^2}\nu^2 - \frac{2\Gamma\omega_0^2}{|\xi|^2}\phi^2\right), \tag{3.22}$$

where $|\xi|^2 = 4\Gamma T$ (using Eq. (3.21)) and from this distribution one gets the mean square displacements

$$\langle(\Delta\phi)^2\rangle = \frac{2T}{\omega_0^2}, \quad \langle(\Delta\nu)^2\rangle = T, \quad \langle\Delta\nu\Delta\phi\rangle = 0. \tag{3.23}$$

The spectral distribution of the harmonic noise is given by

$$S_{\mathrm{HN}}(\omega) = \frac{2\Gamma T}{\pi(4\Gamma^2\omega^2 + (\omega^2-\omega_0^2)^2)}. \tag{3.24}$$

Comparing this spectral distribution with the one of the Ornstein-Uhlenbeck process, the above spectral distribution possesses a peak at a finite frequency $\tilde{\omega} = \sqrt{\omega_0^2 - 2\Gamma^2}$. It is shown in Figure 3.4 by the blue curve which peaks at

$\tilde{\omega}$. The width $\Delta\tilde{\omega}$ of the peak can be estimated by finding the full width at half maximum (FWHM) of the spectral function, which gives

$$\Delta\tilde{\omega} \approx 2\sqrt{\Gamma\sqrt{\omega_0^2 - \Gamma^2}}. \tag{3.25}$$

According to the early work of Chandrasekhar [120], the correlation function for such harmonic noise is obtained by assuming the initial distribution of the harmonic noise to be of Gaussian type,

$$\langle\phi(t)\phi(t+h)\rangle = \frac{T}{\omega_0^2}e^{-\Gamma h}\left(\cos(\omega_1 h) + \frac{\Gamma}{\omega_1}\sin(\omega_1 h)\right), \tag{3.26}$$

with $\omega_1 = \sqrt{\omega_0^2 - \Gamma^2}$. Using the above correlation function one can derive another parameter of the harmonic noise

$$\tau_{\mathrm{HN}} = \frac{\int_0^\infty h\langle\phi(t)\phi(t+h)\rangle dh}{\int_0^\infty \langle\phi(t)\phi(t+h)\rangle dh}. \tag{3.27}$$

For exponentially correlated noise this parameter presents the correlation time τ of the noise. In the case of harmonic noise, however, this parameter does not have the meaning of the characteristic time of the decay of the correlation anymore. From Eq.(3.26) one can simply find

$$\tau_{\mathrm{HN}} = \frac{2\Gamma}{\omega_0^2} - \frac{1}{2\Gamma}, \tag{3.28}$$

which may be a positive or a negative quantity. A negative τ_{HN} is connected with the oscillatory behavior of the noise since the spectrum given by Eq. (3.24) possesses well developed peaks in this regime. On the other hand, as long as τ_{HN} is positive the effect of the harmonic noise is quite similar to the effect of the exponentially correlated noise (see the red curve in Figure 3.4). Later, in this section, it is shown how the spectral distribution helps to distinguish different regimes of parameters for the harmonic noise.

Different regimes of parameters

The noise parameters Γ and ω_0 are both given in the unit of frequency. It is essential to know what the large and what the small frequencies are. The frequency scale is specified by the system under consideration, hence defined as $\omega_{\mathrm{s}} = 2\pi/\tau_{\mathrm{s}}$. This already introduces a few regimes of parameters, namely (i) $\omega_0, \Gamma > \omega_{\mathrm{s}}$, (ii) $\omega_0, \Gamma < \omega_{\mathrm{s}}$ and (iii) $\omega_0\omega_{\mathrm{s}} > \Gamma$ (or $\Gamma > \omega_{\mathrm{s}} > \omega_0$).

The spectral distribution given in Eq. (3.24) peaks at $\tilde{\omega}_0 = \sqrt{\omega_0^2 - 2\Gamma^2}$ which

allows for two different regimes: a. fast noise, when the oscillation time of the noise is much less than the damping time, i.e., $2\Gamma^2 \ll \omega_0^2$, and b. slowly-varying noise when $2\Gamma^2 \gg \omega_0^2$. The corresponding spectral distribution corresponding to these limits of the harmonic noise are shown in Figure 3.4 by the blue and the red curves, respectively.

The spectral distribution in a regime of fast noise ($2\Gamma^2 \ll \omega_0^2$), peaks at a finite frequency $\tilde{\omega}_0$ as shown by the blue curve in Figure 3.4. In this regime the noise shows oscillatory behavior and can give rise to resonance phenomena since a specific amount of energy is induced into the system when the spectral distribution shows a peak at a finite frequency.

Assuming high frequencies $\omega_0 \to \infty$ with fixed ratio $2\Gamma/\omega_0^2 = \tau = \textit{const.}$ (i.e., $\Gamma \to \infty$) one is able to arrive at Eq. (3.13), where τ becomes the correlation time of the process and is strictly positive. In such a regime the harmonic noise recovers the exponentially correlated noise with a Lorentzian-like spectral distribution peaked around zero frequency (see the red curve in Figure 3.4). In such a regime, one can define an expression for the strength of the noise, T, in terms of noise characteristic parameters as $T = D\omega_0^2/\tau$.

Algorithm of harmonic noise

In order to develop a numeric simulation and implement the harmonic noise for a physical system, one needs to integrate the Eqs. (3.20). In this section an algorithm to integrate such stochastic differential equations is presented. Introducing $W \equiv (\phi, \nu)$ and $F(t) \equiv (0, \xi(t))$, the above coupled Eqs. (3.20) are written as

$$\dot{W} = M \times W + F(t) \tag{3.29}$$

where the matrix M is defined as

$$M = \begin{pmatrix} 0 & 1 \\ -\omega_0^2 & -\Gamma \end{pmatrix}.$$

The formal solution of Eq. (3.29) is

$$W(t+h) = \left(\exp\left(\int_t^{t+h} M(s)ds\right)\right) W(t) + \int_t^{t+h} \exp\left(\int_s^{s+h} M(z)dz\right) F(s)ds, \tag{3.30}$$

where h is the time step grid of the numerical calculations. The first part of Eq. (3.30) shows the deterministic evolution of the vector W and the second part corresponds to its stochastic evolution. It is then possible to derive the evolution of each component of W. Therefore the final results can be written as

$$\phi(t+h) = A_{11}\phi(t) + A_{12}\nu(t) + w_1 \tag{3.31a}$$

$$\nu(t+h) = A_{21}\phi(t) + A_{22}\nu(t) + w_2, \tag{3.31b}$$

where w_1 and w_2 are Gaussian stochastic variables with zero average and as yet unknown standard deviation and cross correlation. The matrix A is a real matrix which follows immediately from the first term of Eq. (3.30). For the stochastic variables, the correlation of w_1 and w_2 in Eq. (3.31) can be matched with the corresponding quantities in Eq. (3.30). The expressions for w_1 and w_2 can be written in the following general form

$$w_1 = B_{11} z_1 \tag{3.32a}$$
$$w_2 = B_{21} z_1 + B_{22} z_2, \tag{3.32b}$$

where z_1 and z_2 are uncorrelated Gaussian variables with zero average and whose standard deviation one. The second term in Eq. (3.32b) makes w_1 and w_2 uncorrelated. In the following explicit expressions for A_{ij} and B_{ij} will be calculated.

Diagonalizing the matrix M, the eigenvalues $\lambda_\pm$ of this matrix can be calculated

$$\lambda_\pm = -\Gamma \pm \sqrt{\Gamma^2 - \omega_0^2}. \tag{3.33}$$

Considering a matrix U that can diagonalize the matrix M and the resulting diagonal matrix, the Eq. (3.29), one can write $U\dot{W} = UMU^{-1}UW$. Solving this equation, the matrix elements A_{ij} and B_{ij} given in Eqs. (3.31) and (3.32) can be calculated as

$$A_{11} = -\frac{1}{\lambda_- - \lambda_+} \left\{ \lambda_+ e^{h\lambda_-} - \lambda_- e^{h\lambda_+} \right\}, \tag{3.34a}$$
$$A_{12} = -\frac{1}{\lambda_- - \lambda_+} \left\{ e^{h\lambda_-} - e^{h\lambda_+} \right\}, \tag{3.34b}$$
$$A_{21} = -\frac{\lambda_- \lambda_+}{\lambda_- - \lambda_+} \left\{ e^{h\lambda_-} - e^{h\lambda_+} \right\}, \tag{3.34c}$$
$$A_{22} = -\frac{1}{\lambda_- - \lambda_+} \left\{ \lambda_- e^{h\lambda_-} - \lambda_+ e^{h\lambda_+} \right\}. \tag{3.34d}$$

Writing an expression for the moments of w_1 and w_2 leads to the numerical evaluation of the matrix B. Therefore, if the moments $\langle w_1^2 \rangle$, $\langle w_1 w_2 \rangle$, and $\langle w_2^2 \rangle$ are known by multiplying and averaging Eq. (3.31), and whilst considering the properties of z_1 and z_2, then

$$B_{11}^2 = \langle w_1^2 \rangle, B_{12}^2 = \langle w_1 w_2 \rangle / B_{11}, B_{22}^2 = \langle w_2^2 \rangle - B_{12}. \tag{3.35}$$

The expressions for the various moments of the variables w_1 and w_2 read

$$\langle w_1^2 \rangle = C_w \left\{ \frac{e^{2h\lambda_+ - 1}}{2\lambda_+} + \frac{e^{2h\lambda_- - 1}}{2\lambda_-} - 2\frac{e^{h(\lambda_+ + \lambda_-) - 1}}{\lambda_+ + \lambda_-} \right\}, \tag{3.36a}$$

$$\langle w_1 w_2 \rangle = C_w \left\{ -\frac{e^{2h\lambda_+}}{2} + \frac{1 - e^{2h\lambda_- - 2}}{2} - \left(1 - e^{h(\lambda_+ + \lambda_-)}\right) \right\}, \tag{3.36b}$$

$$\langle w_2^2 \rangle = C_w \left\{ \frac{\left(e^{2h\lambda_+} - 1\right)\lambda_+}{2} + \frac{\left(e^{2h\lambda_-} - 1\right)\lambda_{-1}}{2} - 2\lambda_-\lambda_+ \frac{e^{h(\lambda_+ + \lambda_-)} - 1}{\lambda_+ + \lambda_-} \right\}. \tag{3.36c}$$

where the parameter $C_w = 4\Gamma T / \left(\omega_0^2 - \Gamma^2\right)$. Using the expressions given in Eq. (3.36), the algorithm of harmonic noise can be implemented in numerical simulations. Later in chapter 6 the numerical results will be presented and it is shown how the driving by this harmonic noise can affect the transport of ultracold atoms in optical lattices. In the following another type of time-dependent phase is presented which is not stochastic and random anymore, but rather is a purely oscillatory function.

3.2.3 Deterministic phase

One can define the shifting phase by a time-dependent deterministic function which is no longer a stochastic function. We define here an oscillatory function as the time-dependent phase for the lattice

$$\phi(t) = A\cos(\Omega t + \varphi), \tag{3.37}$$

where A is the amplitude and Ω is the frequency of the oscillations. The parameter φ is a random phase picked from a flat distribution. These parameters define the characteristic parameters of the deterministic phase. The time-dependence is fast oscillating for large Ω and very slowly varying in time when Ω is small. The parameter A determines the strength of this so called "deterministic noise". It is important to study different limits of these parameters. A very small amplitude of the phase in comparison with energy scale of the system may have no effect on the observable whereas a very large amplitude may drive the system out of equilibrium.

The power spectrum of the defined cosine function is a delta function.

$$S_{\mathrm{d}}(\omega) = \frac{A^2}{4}\left\{\delta(\omega - \Omega) + \delta(\omega + \Omega)\right\}. \tag{3.38}$$

The corresponding spectral distribution and its characteristic frequencies are demonstrated in Figure 3.5. There are two characteristic frequencies for such

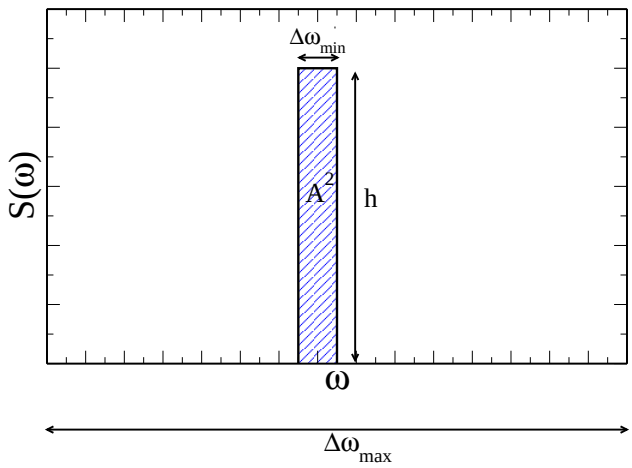

Figure 3.5: A schematic illustration of the spectral distribution $S_{\mathrm{d}}(\omega)$ of the deterministic phase $\phi(t) = A\cos(\Omega t)$. The frequency ranges are defined as follows: $\Delta\omega_{min} = \frac{2\pi}{T_{\mathrm{tot}}}$, where T_{tot} is the total integration time of the system, and $\Delta\omega_{max} = \frac{2\pi}{2\delta t}$, with δt being the time step of the calculations.

a delta-like distribution, namely, $\Delta\omega_{min} = \frac{2\pi}{T_{\mathrm{tot}}}$, where T_{tot} is the total integration time of the system, and $\Delta\omega_{max} = \frac{2\pi}{2\delta t}$ (according to the Nyquist frequency theory [123]), where δt is the time grid (numerical integration time step) of the system. The small frequency $\Delta\omega_{min}$ determines the width of the delta function in the spectral distribution. The height of the delta-like distribution can be estimated by dividing the area under the delta-like function by its width $\Delta\omega_{min}$, i.e., $h = \frac{A^2}{\Delta\omega_{min}}$ (see Figure 3.5).

The spectral distribution of the harmonic noise, in the limit of fast noise, peaks at frequency $\tilde{\omega}_0$ which is similar to the delta-like spectral distribution of the "deterministic noise". Hence, comparable areas under the power spectrum of the harmonic noise (around the peak frequency) and the deterministic phase gives a reference tool to check the effect of harmonic noise in the regime of fast noise:

$$\begin{aligned} A^2 &= \int_0^{\omega} S_{\mathrm{HN}}(\omega')\, d\omega' \\ &= \int_0^{\omega} d\omega\, \frac{2\Gamma T}{\pi(4\Gamma^2\omega^2 + (\omega'^2 - \omega_0^2)^2)}. \\ &\approx \langle \phi(t)^2 \rangle_{\mathrm{HN}} \end{aligned} \tag{3.39}$$

Results of the effect of the deterministic phase on the tunneling of the ultracold atom in bichromatic lattices will be presented in section 6.5.

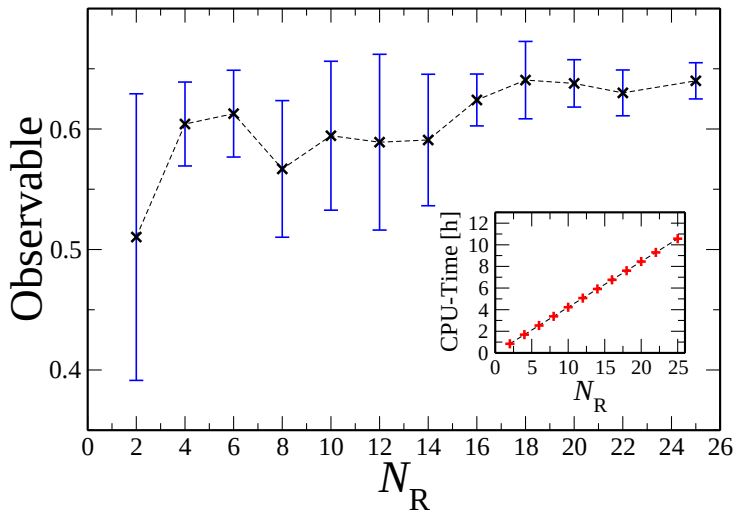

Figure 3.6: Dependence of the accuracy of the observable on the number of realizations N_{R}. The standard deviation depending on the number of realizations are shown by blue vertical line. Inset: CPU-time in hour versus number of realizations.

3.2.4 Averaging and ensembles

Dealing with stochastic processes and random numbers, it is necessary to consider a large enough number of realizations of the noise. The qualitatively true response of the system to the noise can be found when averaging over the ensemble of realizations. The larger the number of the realizations the closer the results are to the expected response. The error bars denote the standard deviation of the results with respect to the finite number of realizations as shown in Figure 3.6. The notion that averaging over repeated realizations of a probe reduces these fluctuations presupposes that the noise in the different realizations is uncorrelated because only then we get the desired noise-suppression.

The stochastic nature of the potential $V_{\mathrm{dis}}(x,t)$ defined in Eq.(6.2) makes it necessary to average our results over a sufficient number of noise realizations. Figure 3.6 shows the observable $P_{\mathrm{a}}(t_0 \approx 6\,T_{\mathrm{B}})$, which is mostly studied in chapter 6, for different number of realizations. As seen the error bars are smaller for larger number of realizations. For the results presented in chapter 6, 20 realizations turned out to well stabilize statistical fluctuations (as seen in Figure 3.6). Of course, larger number of realizations gives a more accurate result, but it costs more time.

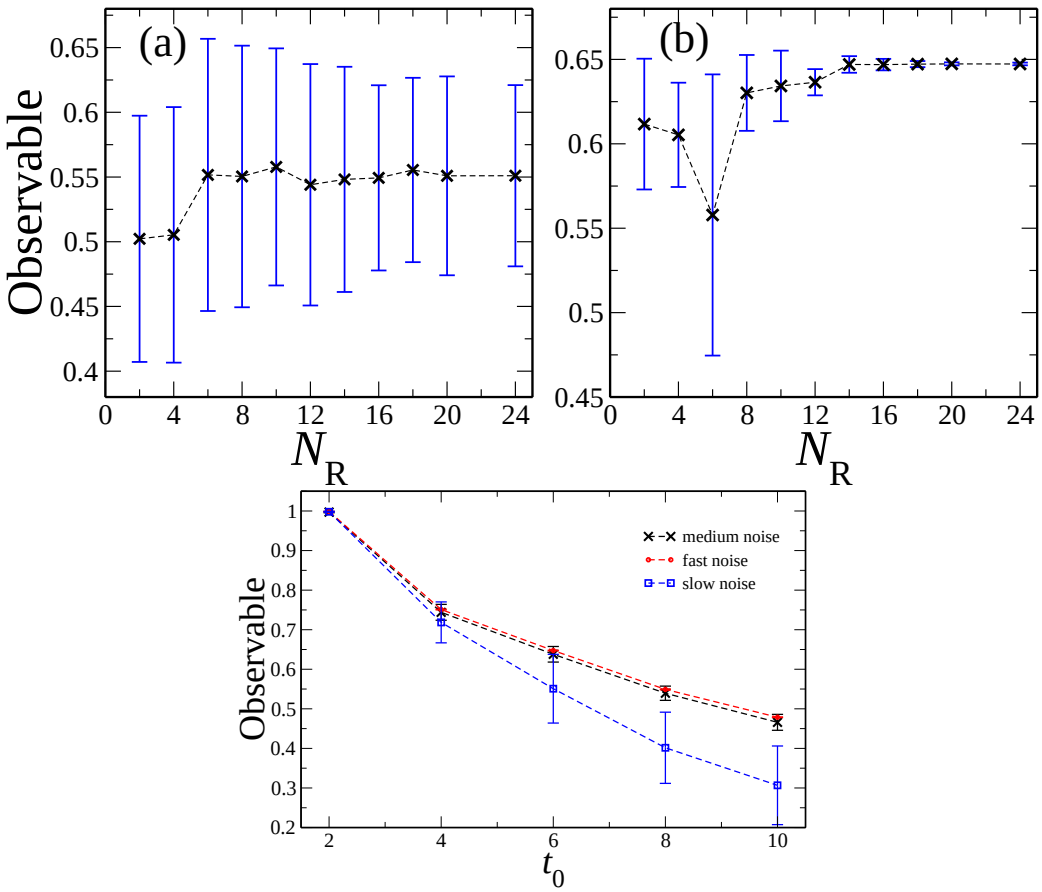

Figure 3.7: Top: Dependence of the observable on the number of realization N_{R}: (a) In the regime of slowly varying noise, (b) fast oscillating regime of noise. The error bar are shown by blue vertical line. Bottom: Dependence of the observable on the time of realization t_0. The error bar are shown by blue vertical line. The data are obtained by averaging over 20 realizations.

The time that is needed to numerically calculate the observable (the survival probability $P_{\mathrm{a}}(t)$) for each realization of the noise is about $30\,\mathrm{min}$. Therefore, considering 20 times realizations of the noise, each data point shown in chapter 6 took around $600\,\mathrm{min}$ time of calculations. The inset of Figure 3.6 shows the dependence of the CPU time needed for our calculations on different number of realizations.

The error depends also on the noise parameters. Figure 3.7 shows the observable for different numbers of realizations: (a) in the slowly varying regime of noise, and (b) in the fast oscillating regime of noise. The errors bars are almost equally long in the slowly varying regime, and after 6 realizations of the

noise, the fluctuations of the observable are very small. For the other regime shown in panel (b), the error bars are smaller for larger number of realizations and after 12 realizations the fluctuations vanishes and the observable remains almost constant. This behavior is expected since – in the case of fast noise – an effective time average occurs which stabilizes the fluctuations. The dependence of the error on the realization time is shown in Figure 3.7-bottom. According to our data in this figure, the observable and its error (standard deviation over 20 realizations) does not depend on the time of realizations.

Chapter 4

Numerical methods

In order to integrate the Schrödinger or the Gross–Pitaevskii equations, numerical methods can be used. In this chapter, an implicit integration procedure is introduced, based on a numerical evaluation of the time evolution operator. This is applied to the representation of the wave function in a grid basis.

Since the Bose-Einstein condensate can be prepared with certain symmetries due to the trap (see Chapter 2), different coordinate representations can be considered. This can reduce the three-dimensional Gross–Pitaevskii equation to a quasi one- or two-dimensional one. The integration methods can be generalized or modified with respect to symmetries in the system.

This chapter starts with solving the one-dimensional problem in section 4.1. The numerical scheme to intergate the corresponding one-dimensional Hamiltonian is presented in this section. Then in section 4.2, the method is generalized for the three-dimensional system with no symmetry. Finally, it will be shown in section 4.3 how the generalized integration scheme is modified to solve the Gross–Pitaevskii equation in cylindrical coordinates.

4.1 Implicit integration scheme in one-dimension

In this section, an implicit method to solve the partial differential equation given by a one-dimensional nonlinear Schrödinger equation is presented. The time evolution of the Hamiltonian $H(x,t)$ is described as

$$\begin{aligned} i\hbar\frac{\partial\psi\left(x,t\right)}{\partial t} &= H\left(x,t\right)\psi\left(x,t\right), \\ H\left(x,t\right) &= -\frac{\hbar^2}{2M}\frac{\partial^2}{\partial x^2} + V\left(x\right) + U_{\mathrm{1D}}\left|\psi\left(x,t\right)\right|^2, \end{aligned} \tag{4.1}$$

where $\psi(x,t)$ is the wave function of the condensate and $V(x)$ is the external potential. The nonlinear term $U_{1\mathrm{D}}|\psi(x,t)|^2$, with $U_{1\mathrm{D}} \equiv 2\hbar\omega_\perp a_\mathrm{s} N$ (see section 2.1.2), presents the one-dimensional interaction potential for the weak atom-atom interactions of the condensate atoms. It can be considered as an additional, time-dependent effective potential.

Solution to the time-dependent Schrödinger equation

The solution to the time-dependent nonlinear Schrödinger equation as in Eq. (4.1) in the Schrödinger representation is given by

$$\psi(x,t) = u(t,t_0)\,\psi(x,t_0)\,. \tag{4.2}$$

where the time evolution operator is defined as

$$\begin{aligned} u(t,t_0) =& \mathcal{T}\exp\left(-\frac{i}{\hbar}\int_{t_0}^{t} dt' H(x,t')\right) \\ =& 1 - \frac{i}{\hbar}\int_{t_0}^{t} dt_1 H(x,t_1) + (\frac{i}{\hbar})^2 \int_{t_0}^{t} dt_1 \int_{t_0}^{t_1} dt_2 H(x,t_1)\,H(x,t_2) + \cdots\,. \end{aligned} \tag{4.3}$$

Here, the nonlinear term $U_{1\mathrm{D}}|\psi(x,t)|^2$ is considered as a self-consistent time-dependent effective potential. For a small time difference $\Delta t = t - t_0$, according to the mean-value theorem the above integral can be approximated as

$$u(t,t_0) \simeq 1 - \frac{i}{\hbar}H(x,t)\,\Delta t + \frac{i^2}{2\hbar^2}H^2(x,t)\,\Delta t^2 + \cdots\,. \tag{4.4}$$

Assuming that $\psi(x,t)$ is known at time t, the wave function $\psi(x,t+\Delta t)$ at time $t+\Delta t$ can now be calculated by Eq. (4.2). Taking into account only the terms of the order $\mathcal{O}(\Delta t)$, a simple explicit solution results from Eq. (4.4) reads

$$\psi(x,t+\Delta t) = \left[1 - \frac{i}{\hbar}H(x,t)\,\Delta t\right]\psi(x,t)\,. \tag{4.5}$$

But since the operator $\left[1 - \frac{i}{\hbar}H\Delta t\right]$ is non-unitary, this explicit integration method is numerically unstable [124], and moreover, it does not conserve the normalization of the wave function. To circumvent these disadvantages, the so-called *Cayley*'s theorem can be used which results in the following presentation of time evolution operator [125]

$$\psi(x,t+\Delta t) = \frac{1 - \frac{i}{2\hbar}H\Delta t}{1 + \frac{i}{2\hbar}H\Delta t}\psi(x,t)\,. \tag{4.6}$$

This approximation has error on the order of $\mathcal{O}((\Delta t)^3)$. This error can be determined by comparing the power series of the time evolution operator given in Eq. (4.6) with the power series of $\exp(-iH\Delta t/\hbar)$. Taking the first four terms in the power series expansion of this time evolution operator reads

$$e^{-\frac{iH\Delta t}{\hbar}} = 1 + \frac{iH\Delta t}{\hbar} - \frac{(H\Delta t)^2}{2\hbar^2} + \frac{i\,(H\Delta t)^3}{6\hbar^3} + \cdots, \tag{4.7}$$

while the expansion for the approximation $\frac{1-\frac{i}{2\hbar}H\Delta t}{1+\frac{i}{2\hbar}H\Delta t}$ gives

$$\frac{1-\frac{i}{2\hbar}H\Delta t}{1+\frac{i}{2\hbar}H\Delta t} = 1 + \frac{iH\Delta t}{\hbar} - \frac{(H\Delta t)^2}{2\hbar^2} + \frac{i\,(H\Delta t)^3}{4\hbar^3} + \cdots. \tag{4.8}$$

These two expansions differ beginning only in the third term, and the error will be of the third order. With this *unitary* time-evolution operator, the norm of the wavefunction is also conserved. Eq. (4.6) results in the following integration algorithm:

$$\left[1 + \frac{i}{2\hbar}H\Delta t\right]\psi(x, t+\Delta t) = \left[1 - \frac{i}{2\hbar}H\Delta t\right]\psi(x, t). \tag{4.9}$$

In numerical analysis, this type of solution is called an implicit scheme or a Crank–Nicholson scheme [124]. In the numerical simulation of the time evolution over a total time period $\Delta T = t_{\mathrm{f}} - t_{\mathrm{i}}$ (with $t_{\mathrm{f}} > t_{\mathrm{i}}$), we divide ΔT into N_{t} equal time intervals $\Delta t = \Delta T/N_{\mathrm{t}}$. The aim is to calculate numerically the wave function of the discrete times $t_{\mathrm{n}} = n\Delta t$, by means of the implicit scheme given in Eq. (4.9). To solve this equation numerically, one must discretize Eq. (4.1). In the following, the discretization process is presented.

4.1.1 Expansion over the grid basis

To solve the one-dimensional Gross–Pitaevskii equation given in Eq. (4.1), the wave function is expanded over a discrete basis. The continuous variable x is represented as a discrete variable, $x = x_0 + j\Delta x$, where Δx is the mesh size, x_0 is the starting value, and j is an integer which runs from 1 to N_x. Time is also represented as a discrete variable as $t = t_0 + n\Delta t$, where Δt is the time step, t_0 is the initial time, and n is an integer. Both t_0 and x_0, can be set to zero for simplicity. Therefore, one can define the following basis states

$$\chi_j \equiv \begin{cases} 1\,, x_j - \frac{1}{2}\Delta x \leq x < x_j + \frac{1}{2}\Delta x \\ 0\,, \text{otherwise} \end{cases} \tag{4.10}$$

The wave function, therefore, is expanded over this discrete space as $\psi(x, t_n) = \sum_{j=1}^{N_x} \psi_j^n \chi_j$, where the expansion coefficient, at time t_n, is $\psi_j \equiv \psi_j^{t_n}$.

Discretization of the wave function

The form of the wave function is a column vector, with each component taken at a mesh point, such that for any time t, the wave function can be written as

$$\psi^{n\Delta t}(x) = \begin{pmatrix} \psi(\Delta x) \\ \psi(2\Delta x) \\ \psi(3\Delta x) \\ \vdots \\ \psi(N_x \Delta x) \end{pmatrix}, \tag{4.11}$$

In our numerical calculation N_x typically takes a value between $2^{14} - 2^{16}$. Using a loop over time, a new ψ vector can be generated for each time step.

Discretization of the Hamiltonian

The potential term in the Hamiltonian is a function of x. Therefore, the discrete representation of $V(x)$, at any time t_n, is

$$V_{n\Delta t}(x) = \begin{pmatrix} V(\Delta x) \\ V(2\Delta x) \\ V(3\Delta x) \\ \vdots \\ V(N_x \Delta x) \end{pmatrix}. \tag{4.12}$$

The interaction term consists of the time-dependent wave function and can also be generated at each time step as $U_{1\mathrm{D}} |\psi(x, n\Delta t)|^2 \equiv U_{1\mathrm{D}} |\psi_j^n|^2$, for its time-dependence see section 4.1.2 below.

The discretization of the kinetic energy operator is more involved. A proper discrete representation for the second spatial derivative can be found using a finite difference method. The Crank–Nicolson method is a finite difference method which is based on central difference in space, and the trapezoidal rule in time, giving second-order convergence in time. This method provides a discrete representation for the kinetic term

$$-\frac{\hbar^2}{2M}\frac{\partial^2 \psi_j^n}{\partial x^2} = -\frac{\hbar^2}{2M}\frac{\psi_{j+1}^n + \psi_{j-1}^n - 2\psi_j^n}{\Delta x^2}, \tag{4.13}$$

where ψ_j^n is in fact $\psi_{\mathrm{n\Delta t}}(x)$ and x for an arbitrary mesh point is $j\Delta x$. Therefore, the Hamiltonian operating on ψ at an arbitrary mesh point $j\Delta x$ at each time $n\Delta t$, has the following discrete form

$$H\psi_j^n = -\frac{\hbar^2}{2M\Delta x^2}\left\{\psi_{j+1}^n + \psi_{j-1}^n - 2\psi_j^n\right\} + V_j\psi_j^n + U_{1\mathrm{D}}\left|\psi_j^n\right|^2 \psi_j^n. \tag{4.14}$$

The mesh runs from $j = 1, \cdots, N_x$, therefore, for solving this equation, values for $\psi(0 \cdot \Delta x)$ and $\psi((N_x+1)\Delta x)$ are needed, which are outside the mesh system. These values are simply set to zero. Of course, this is like assuming the potential is suddenly infinite outside the mesh system. Practically, the spatial system should be constructed sufficiently large so that, over the time scales of interest, the wave functions do not reflect from these "hard walls".

As a result of the discretization, a single differential equation is thus replaced with a set of N_x coupled equations. The Hamiltonian has the form of an $N_x \times N_x$ matrix:

$$H = \begin{pmatrix} -2\kappa + K & \kappa & 0 & \cdots & 0 \\ \kappa & -2\kappa + K & \kappa & 0 & \vdots \\ 0 & \ddots & \ddots & \ddots & 0 \\ \vdots & 0 & \kappa & -2\kappa + K & \kappa \\ 0 & \cdots & 0 & \kappa & -2\kappa + K \end{pmatrix}, \tag{4.15}$$

where $\kappa = -\hbar^2/(2M\Delta x^2)$ and $K = V_j + U_{1\mathrm{D}} \left|\psi_j^n\right|^2$. As seen, the Hamiltonian H is a tridiagonal matrix, with non-zero term on only the main diagonal and the first upper and lower diagonals. To reduce the memory required for this calculation, only non-zero terms are stored. Using the discrete representation of the Hamiltonian given in Eq. (4.14), the *r.h.s.* term of Eq. (4.9) i.e., $[1 - iH\Delta t/(2\hbar)]\,\psi(x_j, t_n)$ in the discrete form reads

$$\psi_j^n - \frac{i\Delta t}{2\hbar}\left[\frac{\hbar^2\left(\psi_{j+1}^n + \psi_{j-1}^n - 2\psi_j^n\right)}{2M\Delta x^2} + V_j\psi_j^n + U_{1\mathrm{D}}\left|\psi_j^n\right|^2\psi_j^n\right]. \tag{4.16}$$

Using the matrix representation of Hamiltonian as Eq. (4.15), one finds the following tridiagonal matrix representation for the operator $\mathbf{M}_1 \equiv 1 - iH\Delta t/(2\hbar)$:

$$\mathbf{M}_1 = \begin{pmatrix} \ddots & & & & \\ & \alpha & 1-\beta_{j-1} & \alpha & & \\ & & \alpha & 1-\beta_j & \alpha & \\ & & & \alpha & 1-\beta_{j+1} & \alpha \\ & & & & & \ddots \end{pmatrix}, \tag{4.17}$$

where

$$\begin{aligned} \alpha &\equiv \frac{i\Delta t\hbar}{4M\Delta x^2} \\ \beta_j &\equiv \frac{i\Delta t\hbar}{2M\Delta x^2} + \frac{i\Delta t}{\hbar}\left(V_j + U_{1\mathrm{D}}\left|\psi_j^n\right|^2\right). \end{aligned} \tag{4.18}$$

The operator $\mathbf{M}_2 \equiv 1 + iH\Delta t/(2\hbar)$ results to a similar tridiagonal matrix

$$\mathbf{M}_2 = \begin{pmatrix} \ddots & & & & & & \\ & -\alpha & 1+\beta_{j-1} & -\alpha & & & \\ & & -\alpha & 1+\beta_j & -\alpha & & \\ & & & -\alpha & 1+\beta_{j+1} & -\alpha & \\ & & & & & & \ddots \end{pmatrix}. \tag{4.19}$$

Therefore, the numerical evaluation of the implicit integration scheme given in Eq. (4.9) is described by the following matrix equation

$$\mathbf{M}_2\psi^{n+1} = \mathbf{M}_1\psi^n \Rightarrow \psi^{n+1} = \mathbf{M}_2^{-1}\mathbf{M}_1\psi^n. \tag{4.20}$$

The vectors ψ^n and ψ^{n+1} are wave functions as defined in Eq. (4.11) at time t_n and t_{n+1}, respectively. The above equation has the form of $\mathbf{A} \cdot \vec{X} = \vec{b}$, where $\vec{b}$ is an $N_x \times 1$ column vector and equals $\mathbf{M}_1\psi^n$. The matrix $\mathbf{A} = \mathbf{M}_2$ given in Eq. (4.19) and $\vec{X}$ is what has to be found, i.e., $\psi(x, t + \Delta t)$, through solving the above equation. In our numerical simulation, we solve this matrix equation using *Gaussian elimination* method for tridiagonal matrices [124]. This algorithm allows to calculate the inversion without actually storing the matrix, i.e., one only needs to store its non-zero elements as a vector. Therefore, it results in one vector which represents the *l.h.s.* matrix in Eq. (4.20) and another vector for the *r.h.s.* of Eq. (4.20).

4.1.2 Predictor–Corrector method

Due to the nonlinear term $U_{1\mathrm{D}}|\psi|^2$, the Hamiltonian given in Eq. (4.1) is a time-dependent operator. Starting from $\psi(x, t)$, using the matrix representation of the integration scheme given in Eq. (4.20), one can calculate $\psi(x, t+\Delta t)$. Therefore, the wave function $\psi(x, t)$ at time t is used in the matrices $\mathbf{M}_1$ and $\mathbf{M}_2$. This assumes, however, the approximation that the effective potential $U|\psi|^2$ induced by the non-linearity is not changing during the time interval Δt. In principle, the error caused by this approximation can be reduced by choosing an infinitesimally small time interval Δt for the numerical integration. Due to such a small time interval, it becomes necessary to have a larger number of matrix inversions which causes a huge growth of numerical costs.

To deal with this problem, a two step *Predictor–Corrector* method [124] is used in our simulations, which allows to reduce the approximation error induced by the nonlinearity, without being forced to use an infinitesimally small time interval Δt. The basic idea is to use the averaged value over the time interval Δt for the wave function, instead of the wave function $\psi(x, t)$. Therefore, each

integration step is really done in two times to go from time t to time $t+\Delta t$. In the first time, $\psi(x,t)$ is used in the nonlinear term in Eq. (4.20), and a "predicted" wave function $\tilde{\psi}(x,t+\Delta t)$ is obtained, This is the so-called predictor step. In the second time, the integration step of Eq. (4.20) is repeated starting again from $\psi(x,t)$, but placing the averaged value $U_{1\mathrm{D}}\left|\frac{1}{2}\left(\psi(x,t)+\tilde{\psi}(x,t+\Delta t)\right)\right|^2$ in the nonlinear term. In this way, in this so-called corrector-step, an already better approximate value for the nonlinear term is used. This process is represented schematically here:

$$\begin{aligned}
&\text{Predictor step :}\\
&\qquad \psi(x,t) \xrightarrow{U_{1\mathrm{D}}|\psi(x,t)|^2} \tilde{\psi}(x,t+\Delta t)\\
&\text{Corrector step :}\\
&\qquad \psi(x,t) \xrightarrow{U_{1\mathrm{D}}\left|\frac{1}{2}\left(\psi(x,t)+\tilde{\psi}(x,t+\Delta t)\right)\right|^2} \psi(x,t+\Delta t)
\end{aligned} \tag{4.21}$$

4.1.3 Imaginary time propagation

The numerical method developed in this chapter, can be used not only to simulated the time evolution of a Bose-Einstein condensate, but also it allows calculating the ground-state wave function $\Phi_0(x)$ of a condensate in an external potential. The ground state is the lowest energy state of a solution of the Schrödinger or the Gross-Pitaevskii equation. Here, we introduce a method which is known as the time-imaginary propagation [126], which allows the calculation of $\Phi_0(x)$. In this method the following imaginary time are defined

$$t \to \tau \equiv -it \quad \Rightarrow \quad \Delta t \to \Delta\tau \equiv -i\Delta t \tag{4.22}$$

By these substitutions, from Eq. (4.1) one arrives at the following nonlinear diffusion equation

$$\hbar\frac{\partial\psi\left(x,t\right)}{\partial t} = \left[-\frac{\hbar^2}{2M}\frac{\partial^2}{\partial x^2} + V\left(x\right) + U_{1\mathrm{D}}\left|\psi\left(x,t\right)\right|^2\right]\psi\left(x,t\right), \tag{4.23}$$

The process of finding the ground state of this equation is quite similar to the process of finding the wave function at time t of the real time evolution explained previously. The implicit integration scheme given in Eq. (4.9) is also used for the imaginary propagation in the following modified form

$$\left[1+\frac{1}{2\hbar}H\Delta t\right]\psi\left(x,t+\Delta t\right) = \left[1-\frac{1}{2\hbar}H\Delta t\right]\psi\left(x,t\right). \tag{4.24}$$

Using the discrete forms of wavefunction and the Hamiltonian, one can arrive at the following matrix representation

$$\psi^{n+1} = \tilde{\mathbf{M}}_2^{-1}\tilde{\mathbf{M}}_1\psi^n, \tag{4.25}$$

with

$$\tilde{\mathbf{M}}_1 = \frac{1}{i}\begin{pmatrix} \ddots & & & & & \\ & \alpha & i-\beta_{j-1} & \alpha & & \\ & & \alpha & i-\beta_j & \alpha & \\ & & & \alpha & i-\beta_{j+1} & \alpha \\ & & & & & \ddots \end{pmatrix}, \tag{4.26}$$

and

$$\tilde{\mathbf{M}}_2 = \frac{1}{i}\begin{pmatrix} \ddots & & & & & \\ & -\alpha & i+\beta_{j-1} & -\alpha & & \\ & & -\alpha & i+\beta_j & -\alpha & \\ & & & -\alpha & i+\beta_{j+1} & -\alpha \\ & & & & & \ddots \end{pmatrix}. \tag{4.27}$$

In order to determine the ground state wave function with the imaginary propagation, the iteration scheme is used as follows

$$\begin{aligned} &\text{Propagation step}: \psi^{n+1} = \tilde{\mathbf{M}}_2^{-1}\tilde{\mathbf{M}}_1\psi^n, \\ &\text{Renormalization}: \psi^{n+1} \to \psi^{n+1} = \sqrt{\mathcal{N}/\tilde{\mathcal{N}}}\psi^{n+1}, \end{aligned} \tag{4.28}$$

where $\mathcal{N} = \int_{-\infty}^{\infty} dx\, |\Phi_0(x)|^2$ and $\tilde{\mathcal{N}} \equiv \int_{-\infty}^{\infty} dx\, |\psi(x, t_0 + \Delta t)|^2 \leq \mathcal{N}$, until a given initial wave function $\psi^{n=0}$ has developed to a steady wave function. Numerically, this can be implemented, by computing the maximum norm $\mathcal{N}_{\max} = \max\left|\psi_j^{n+1} - \psi_j^n\right|$ for each integration step. Once $\mathcal{N}_{\max}$, over several propagation steps, become smaller than a predetermined Limit δ, one can say that the stationary ground state in the desired precision has been achieved. In our calculation δ is set to 10^{-14}.

4.2 Integration scheme in three-dimension

In this section, the generalized implicit integration scheme in the three-dimensional cartesian coordinate is presented. As presented in the first chapter, the goal is to describe the dynamics of the Bose–Einstein condensate, prepared in the three-dimensional harmonic trap, which is a three-dimensional system. In the presence of the weak atom-atom interaction, the dynamics of such a system is very well described by the three-dimensional Gross-Pitaevskii equation which generally can be written in cartesian coordinates

$$\begin{aligned} i\hbar\frac{\partial\psi\left(\vec{r},t\right)}{\partial t} &= H\left(\vec{r},t\right)\psi\left(\vec{r},t\right), \\ H\left(\vec{r},t\right) &= -\frac{\hbar^2}{2M}\left(\frac{\partial^2}{\partial x^2}+\frac{\partial^2}{\partial y^2}+\frac{\partial^2}{\partial z^2}\right)+V\left(x,y,z\right)+U\left|\psi\left(\vec{r},t\right)\right|^2, \end{aligned} \tag{4.29}$$

where $\vec{r} \equiv (x,y,z)$ and $\psi\left(\vec{r},t\right)$ is the wave function of the condensate and $V\left(x,y,z\right)$ is the external potential. The nonlinear term $U\left|\psi(\vec{r},t)\right|^2 \equiv gN_0\left|\psi\left(\vec{r},t\right)\right|^2$, as in section 2.1.2, consists of the coupling constant g in three-dimensional system and the peak density $\left|\psi(\vec{r},t)\right|^2$ of the condensate. This term is considered as an additional, time-dependent effective potential. To solve the Schrödinger equation in higher dimensions, it is common to use the separation method and solve the equation for each coordinate separately. But this is not possible for the nonlinear equation of the Gross–Pitaevskii equation, since the nonlinear term $U\left|\psi\left(\vec{r},t\right)\right|^2$ couples the coordinates. However, it is appropriate to spread the nonlinearity term uniformly on the three spatial directions [127], so we use the effective portion operators

$$H\left(q_\nu,t\right) = -\frac{\hbar^2}{2M}\frac{\partial^2}{\partial q_\nu^2}+V\left(q_\nu\right)+\frac{1}{3}U\left|\psi\right|^2, \ \left(q_\nu = x,y,z\right) \tag{4.30}$$

where the factor $1/3$ provides the evenly weight of $U\left|\psi\right|^2$ for the three operators in x, y, and z directions. The idea is to split the full Hamiltonian in three sub-Hamiltonians, so that at each time the Laplacian with respect to only one coordinate has to be written, leading to the solution of a tridiagonal system explained in section 4.1, and to huge savings in required computer memory. In fact, in the ν-th spatial direction, there are N_ν grid points, so instead of inverting the $N \times N$ tridiagonal matrix $\mathbf{A}$, now, three tridiagonal matrices of degree N_x, N_y, N_z should be inverted. The splitting is carried out so that the commutators are included exactly up to the order Δt^2.

To solve Eq. (4.29), the integration scheme given in Eq. (4.6) is implemented

which for a three-dimensional system one arrives at

$$\begin{aligned}\psi\left(x,y,z,t+\Delta t\right) =& \frac{1}{1+\frac{i\Delta t}{2\hbar}H_z}\left[1-\frac{i\Delta t}{2\hbar}H_x\right]\cdot \\ & \frac{1}{1+\frac{i\Delta t}{2\hbar}H_y}\left[1-\frac{i\Delta t}{2\hbar}H_y\right]\cdot \\ & \frac{1}{1+\frac{i\Delta t}{2\hbar}H_x}\left[1-\frac{i\Delta t}{2\hbar}H_z\right]\psi\left(x,y,z,t\right).\end{aligned} \tag{4.31}$$

There is a problem with the nonlinear term $U\left|\psi(\vec{r},t)\right|^2$, because we should really use a ψ averaged over the time step Δt, not a ψ evaluated at the beginning of the time step. To overcome this problem, the predictor-corrector step (see section 4.1.2) is used. The aim is to calculate the wave function of the discrete times $t_{\mathrm{n}} = n\Delta t$ numerically, by means of the implicit scheme given in Eq. (4.31). To solve this equation numerically, the equation given in Eq. (4.1) is discretize.

Discretization of the wave function and the Hamiltonian

The continuous variables x, y, and z can be represented as discrete variables $\nu = \nu_0 + j_\nu \Delta\nu$, where $\nu = x, y, z$ and $\Delta\nu$ is the mesh sizes in each direction. The starting point is $\nu_0 = (x_0, y_0, z_0)$, and j_ν is an integer. Time is represented as a discrete variable as in the previous section ($t = t_0 + n\Delta t$).
The discrete representation of the wavefunction is

$$\psi = \begin{pmatrix} \psi\left(\Delta x\right) \\ \psi\left(2\Delta x\right) \\ \vdots \\ \psi\left(N_x\Delta x\right) \\ \psi\left(\Delta y\right) \\ \psi\left(2\Delta y\right) \\ \vdots \\ \psi\left(N_y\Delta y\right) \\ \psi\left(\Delta z\right) \\ \psi\left(2\Delta z\right) \\ \vdots \\ \psi\left(N_z\Delta z\right) \end{pmatrix}, \tag{4.32}$$

As seen the wavefunction is restored in one column vector with the length $N_t \equiv N_x N_y N_z$.

The discrete representation of the Hamiltonian H_ν operating on ψ has the

following form

$$H_\nu \psi_j^n = -\frac{\hbar^2}{2M}\frac{\psi_{j+1}^n + \psi_{j-1}^n - 2\psi_j^n}{\Delta\nu^2} + V_j\psi_j^n + \frac{1}{3}U\left|\psi_j^n\right|^2\psi_j^n, \tag{4.33}$$

where j runs from 1 to N_ν. One can see from this discrete representation that the Hamiltonian forms a tridiagonal $N_\nu \times N_\nu$ matrix in each spatial direction. Using these discretization forms of the wave function and the Hamiltonian, $\left[1 - \frac{i\Delta t}{2\hbar}H_\nu\right]\psi$ reads

$$\psi_j^n - \frac{i\Delta t}{2\hbar}\left[-\frac{\hbar^2}{2M}\frac{\psi_{j+1}^n + \psi_{j-1}^n - 2\psi_j^n}{\Delta\nu^2} + V_j\psi_j^n + \frac{1}{3}U\left|\psi_j^n\right|^2\psi_j^n\right], \tag{4.34}$$

which also results in three tridiagonal matrices in each direction. The numerical evaluation of the implicit integration scheme in Eq. (4.31) is described by the matrix equation given in Eq. (4.20). The tridiagonal matrices build up by H_ν are represented by a vector (see end of section 4.1.1). This means that the non-zero elements of matrices on the left and the right hand sides of Eq. (4.20) are restored in a one column matrix (vector) with a length N_t. The procedure will be the same as in one dimension, only instead of one loop over one coordinate, there will be three involuted loops over three spatial directions.

By using the imaginary time propagation (i.e., $t \to \tau \equiv -it$) and the operator splitting method, the ground state of a condensate in the three-dimensional case can also be calculated numerically.

Finally, let us now move to the more important special case of cylindrically symmetric systems. In the following, the integration scheme for cylindrical symmetric system is presented.

4.3 Integration scheme in cylindrical coordinates

Frequently trap geometries are considered to have certain symmetries. In the experimental setup presented in [42, 43], the Bose-Einstein condensate is prepared in the elongated harmonic trap (a cigar-shaped trap). The results of numerical calculations and experimental measurements [42, 43, 44] in such cylindrical symmetrical system will be presented in chapters 5 and 6.

In particular, the solutions to the Gross–Pitaevskii equation of our interest system are rotational invariant with respect to the cylindrical symmetry. The considered system is described by the radial variable ρ and x the longitudinal variable. The trapping potential $V(\vec{r})$ is radially symmetric with respect to the longitudinal x-axis. In principle, this three-dimensional system can be described

by the two-dimensional, nonlinear Gross–Pitaevskii equation in the cylindrical coordinates

$$\begin{aligned} i\hbar\frac{\partial\psi\left(x,\rho,t\right)}{\partial t} &= H\left(x,\rho,t\right)\psi\left(x,\rho,t\right), \\ H\left(x,\rho,t\right) &= -\frac{\hbar^2}{2M}\left(\frac{\partial^2}{\partial x^2}+\frac{\partial^2}{\partial\rho^2}+\frac{\partial}{\rho\partial\rho}\right)+V\left(x,\rho\right)+U\left|\psi\left(x,\rho,t\right)\right|^2. \end{aligned} \tag{4.35}$$

This Hamiltonian depends on x and $\rho \geq 0$. It is possible to split this Hamiltonian into two parts of: x-dependent operator and a ρ-dependent operator as the three-dimension Hamiltonian explained in section 4.2, therefore

$$H_x = -\frac{\hbar^2}{2M}\frac{\partial^2}{\partial x^2}+V\left(x\right)+\frac{1}{2}U\left|\psi\left(x,\rho,t\right)\right|^2. \tag{4.36a}$$

$$H_\rho = -\frac{\hbar^2}{2M}\left(\frac{\partial^2}{\partial\rho^2}+\frac{\partial}{\rho\partial\rho}\right)+V\left(\rho\right)+\frac{1}{2}U\left|\psi\left(x,\rho,t\right)\right|^2. \tag{4.36b}$$

To solve Eq. (4.35), the integration scheme given in Eq. (4.6) is implemented for the system in cylindrical coordinates as follows

$$\begin{aligned} \psi\left(x,\rho,t+\Delta t\right) =& \frac{1}{1+\frac{i\Delta t}{2\hbar}H_\rho}\left[1-\frac{i\Delta t}{2\hbar}H_x\right]\cdot \\ & \frac{1}{1+\frac{i\Delta t}{2\hbar}H_x}\left[1-\frac{i\Delta t}{2\hbar}H_\rho\right]\psi\left(x,\rho,t\right). \end{aligned} \tag{4.37}$$

The Hamiltonian H_x is the same as the one-dimensional Hamiltonian solved in section 4.1. In the following, it is shown how the corresponding matrices of the implicit integration scheme, as in Eq. (4.9), can be indicated for H_ρ with $\rho \geq 0$. Applying the operator $1 \pm iH_\rho\Delta t/\left(2\hbar\right)$ on the wave function ψ in the grid-based representation defined in Eq. (4.10), gives the following discrete form

$$\begin{aligned} \left[1\pm\frac{i\Delta t}{2\hbar}H_\rho\right]\psi_j^n =& \psi_j^n \pm \frac{i\Delta t}{2\hbar}\left(-\frac{\hbar^2}{2M}\left(\frac{\psi_{j+1}^n+\psi_{j-1}^n-2\psi_j^n}{\Delta\rho^2}\right)\right) \\ & \pm\frac{i\Delta t}{2\hbar}\left(-\frac{\hbar^2}{2M}\left(\frac{\psi_{j+1}^n-\psi_{j-1}^n}{2\rho\Delta\rho}\right)\right) \\ & \pm\frac{i\Delta t}{2\hbar}\left(V_j\psi_j^n+\frac{1}{2}U\left|\psi_j^n\right|^2\psi_j^n\right). \end{aligned} \tag{4.38}$$

The discrete grid points are given by $\rho_j = \rho_0 + j\rho$, where j runs from 0 to N_ρ. At $\rho = 0$ the third term in the above equation diverges. This special case for $j = 0$ must be considered separately. To circumvent this problem, an additional

condition should be specified that keep the symmetry of the wave function. Since the wave function should be continuous and continuously differentiable everywhere, the following condition should hold

$$\frac{\partial \psi}{\partial \rho}|_{\rho=0} = 0. \tag{4.39}$$

By implementing L'Hopital's rule one gets

$$\lim_{r\to 0} \frac{1}{\rho}\frac{\partial \psi}{\partial \rho}|_{\rho=0} = \lim_{r\to 0} \frac{\partial^2}{\partial \rho^2}|_{\rho=0}. \tag{4.40}$$

Therefore, the following discrete form for the case of $j = 0$ (i.e., $\rho = 0$) is evaluated

$$\begin{aligned}\left[1 \pm \frac{i\Delta t}{2\hbar} H_\rho\right] \psi_0^n =& \psi_0^n \pm \frac{i\Delta t}{2\hbar}\left(-2\frac{\hbar^2}{2M}\frac{\psi_1^n - 2\psi_0^n + \psi_1^n}{\Delta\rho^2}\right) \\ & \pm \frac{i\Delta t}{2\hbar}\left(V_0\psi_0^n + \frac{1}{2}U\left|\psi_0^n\right|^2\psi_0^n\right).\end{aligned} \tag{4.41}$$

According to the symmetry assumption, ψ_{-1}^n was replaced by ψ_1^n in the second derivative in above equation. Hence, the terms including ψ_0^n are $1 \pm \frac{i\Delta t}{2\hbar}\left(-2\frac{\hbar^2}{2M}\frac{-2}{\Delta\rho^2} + V_0 + \frac{1}{2}U\left|\psi_0^n\right|^2\right)$ and for ψ_1^n is $\pm\frac{i\Delta t}{2\hbar}\left(-2\frac{\hbar^2}{2M}\frac{2}{\Delta\rho^2}\right)$. The following indications for the matrix representation are introduced

$$\alpha_j^1 \equiv \frac{i\Delta t}{2\hbar}\left(-\frac{\hbar^2}{2M}\left(\frac{1}{\Delta\rho^2} + \frac{1}{2\rho\Delta\rho}\right)\right), \tag{4.42a}$$

$$\alpha_j^2 \equiv \frac{i\Delta t}{2\hbar}\left(-\frac{\hbar^2}{2M}\left(\frac{1}{\Delta\rho^2} - \frac{1}{2\rho\Delta\rho}\right)\right), \tag{4.42b}$$

$$\beta_j \equiv \frac{i\Delta t}{2\hbar}\left(-\frac{\hbar^2}{2M}\left(\frac{-2}{\Delta\rho^2}\right) + V_j + U\left|\psi_j^n\right|^2\right), \tag{4.42c}$$

$$\gamma \equiv \frac{i\Delta t}{2\hbar}\left(-\frac{\hbar^2}{2M}\left(2\cdot\frac{-2}{\Delta\rho^2}\right) + V_0 + \frac{1}{2}U\left|\psi_0^n\right|^2\right), \tag{4.42d}$$

$$\eta \equiv \frac{i\Delta t}{2\hbar}\left(-\frac{\hbar^2}{2M}\left(2\cdot\frac{2}{\Delta\rho^2}\right)\right). \tag{4.42e}$$

For the real time propagation the tridiagonal matrix $\mathbf{M}_1^\rho \equiv 1 - iH_\rho\Delta t/(2\hbar)$ is written as

$$\mathbf{M}_1^\rho = \begin{pmatrix} 1-\gamma & -\eta & & & \\ \alpha_1^2 & 1-\beta_1 & \alpha_1^1 & & \\ & \alpha_2^2 & 1-\beta_2 & \alpha_2^1 & \\ & & \ddots & \ddots & \ddots \\ & & & & \end{pmatrix}, \tag{4.43}$$

and similarly, the operator $\mathbf{M}_2^\rho \equiv 1 + iH_\rho \Delta t/\left(2\hbar\right)$ results to the following tridiagonal matrix

$$\mathbf{M}_2^\rho = \begin{pmatrix} 1+\gamma & \eta & & & \\ -\alpha_1^2 & 1+\beta_1 & -\alpha_1^1 & & \\ & -\alpha_2^2 & 1+\beta_2 & -\alpha_2^1 & \\ & & \ddots & \ddots & \ddots \\ & & & & \end{pmatrix}. \tag{4.44}$$

Using above matrices and also the ones for H_x in Eq. (4.37), one can calculate the wave function $\psi(\vec{r}, t + \Delta t)$ numerically. As seen in Eq. (4.37), one has to performe twice the integration schemes, as introduced in section 4.1, once for H_x and another time for H_ρ.

Similar to section 4.1.3, by replacing t by $-it$ in Eqs. (4.43) and (4.44), one gets the necessary elements for the imaginary-time propagation matrices.

In the following chapters the results of our numerical calculations are presented. The presented methods in the current chapter are used to integrate the Hamiltonians in chapters 5 and 6 and hence to calculate numerically our observable (i.e., the survival probability). For the results presented in section 5.5 for the weakly interacting condensate atoms in the elongated harmonic trap, the three-dimensional Gross–Pitaevskii equation is integrated with the method presented in section 4.3. For the rest of the calculations in chapter 5 and 6 the implicit method in one dimension (described in section 4.1) is applied to integrate the Wannier–Stark Hamiltonian.

Chapter 5

Results 1: Landau–Zener tunneling of Bose–Einstein condensate in tilted optical lattices

In this chapter, numerical results as well as experimental data, published in our papers [42, 43], on the Landau–Zener tunneling of atoms in the Wannier–Stark system are presented. This system is realized with ultracold atoms, forming a Bose–Einstein condensate, in an optical lattice subjected to a static tilting force [23]. The tilt is experimentally implemented by accelerating the optical lattice [17, 21, 23, 27, 35, 37, 38, 106, 128]. The Landau–Zener tunneling of a Bose–Einstein condensate between the Bloch bands in such a tilted lattice is explored in this chapter. We compute the time dependence of the tunneling probability of Bose–Einstein condensate atoms out of the ground band, in which they were originally prepared. The lattice depth controls the tunneling barrier, while its acceleration controls the time dependence of the Hamiltonian. At large accelerations Landau–Zener tunneling leads to significant interband transitions for the condensate [27, 41]. This tunneling process is detected by studying the measured atomic momentum distributions. It is shown that by changing the initial condition and also the system parameters, it is possible to control the tunneling rate of the Bose–Einstein condensate to higher bands. Introducing atom-atom interactions into the system provides a further handle to control the interband tunnelings of the condensate atoms. It is also discussed in this chapter that the time dependence of the tunneling probability can be calculated by performing a projective quantum measurement on the eigenstates in a given basis of the Hamiltonian describing the Bose–Einstein condensate within the optical lattice [42, 43].

Measurements and calculations presented in this chapter resolve the step-like time dependence of the occupation probability. Using different theoretical as well as experimental protocols [43], it is possible to perform calculations and experiments both in the adiabatic basis of the lattice eigenstates and in the diabatic basis of the free-particle momentum eigenstates. Achieved theoretical and experimental results clearly show that the time dependence of the transition probability exhibits a step-like structure with a finite transition time and oscillations with a finite damping time, all of them depending on the choice of the measurement basis.

This chapter is organized as follows. The limits one faces in applying the Landau–Zener theory to the Wannier–Stark problem and the essential theoretical and numerical tools to describe our time-resolved measurements are reported in Section 5.1 and 5.2. In section 5.3 the considered observable is introduced. This observable is called the survival probability and is the probability of the Bose–Einstein condensate to remain in the ground band which it has been initially prepared. Details about its theoretical calculations and the resulting data are presented in this section. More numerical and experimental data [42, 43] on the survival probability of the condensate in the ground band for different system parameters are demonstrated in section 5.4. It will be shown in this section that how the characteristic parameters if the system affect the Landau–Zener tunneling rate and provide the possibility to control the Landau–Zener tunneling of atoms out of the ground band coherently. In the last section, the impact of atom-atom interactions on the tunneling rate is studied.

5.1 Landau–Zener limit of Wannier–Stark problem

The two-level Landau–Zener theory can be generalized to study the temporal evolution of ultracold atoms loaded into a spatially periodic potential subjected to an additional static force in the presence of negligible atom-atom interactions, as in the experimental conditions [42, 43]. The dynamics of ultracold atoms in a tilted quasi one-dimensional optical lattice can be described by the well-known Wannier–Stark Hamiltonian [25]

$$\tilde{H} = -\frac{\hbar^2}{2M}\frac{d^2}{dx^2} + \frac{V}{2}\cos\left(2k_{\mathrm{L}}x\right) + Fx, \tag{5.1}$$

where M is the atomic mass, V is the depth of the optical lattice, $k_{\mathrm{L}} = 2\pi/\lambda_{\mathrm{L}}$ is the wave number of the laser light, with wavelength $\lambda_{\mathrm{L}} = 842\ \mathrm{nm}$, creating the periodic potential, and F is the Stark force. The spatial period of the lattice

is half the wavelength of the laser: $d_{\mathrm{L}} = \lambda_{\mathrm{L}}/2$. The recoil energy $E_{\mathrm{rec}} = p_{\mathrm{rec}}^2/2M$ and the recoil momentum $p_{\mathrm{rec}} = \pi\hbar/d_{\mathrm{L}}$ are the characteristic energy and momentum scales for our system.

The atomic motion produced by the force F may be interpreted in the upper left energy diagram of Figure 5.1 where for the case of $F = 0$ the atomic energies $E(q)$ for the $n = 0, 1, 2$ lower bands are represented versus the quasi-momentum q within the Brillouin zone of width $p_{\mathrm{B}} = 2p_{\mathrm{rec}} = 2\pi\hbar/d_{\mathrm{L}}$ [27, 106]. Under the action of a constant force F, the quasi-momentum of a condensate, initially prepared at $q = 0$ in the $n = 0$ band scans the lower band in an oscillating motion periodically – the so-called Bloch oscillations [19] – with the Bloch period $T_{\mathrm{B}} = 2\hbar(F_{\mathrm{LZ}}d_{\mathrm{L}})^{-1}$. At the edge of the Brillouin zone, where a level splitting (i.e., gap between the ground and the first excited band of the $F = 0$ system) ΔE increasing with V [41] takes place, tunneling of the condensate to the $n = 1$ energy band may occur. The tunnelled atoms escape from the system through successive tunneling events across the much smaller band gaps between the upper bands. This phenomenon is known as the Landau–Zener tunneling.

The Wannier–Stark Hamiltonian of Eq. (5.1) can be written in dimensionless units [41, 129]

$$H_0 = -\frac{1}{2}\frac{\partial^2}{\partial x_0^2} + \frac{V_0}{16}\cos(x_0) + \frac{F_0 x_0}{16\pi}, \tag{5.2}$$

where $x_0 = 2\pi x/d_{\mathrm{L}}$, and energy and time are rescaled by $H_0 = \tilde{H}/(8E_{\mathrm{rec}})$ and $t_0 = 8tE_{\mathrm{rec}}/\hbar$ respectively. Moreover, in dimensionless units, the lattice depth is given by $V_0 = V/E_{\mathrm{rec}}$ and the force by $F_0 = Fd_{\mathrm{L}}/E_{\mathrm{rec}}$. The translational symmetry of the given Hamiltonian, broken by the static force, is recovered using a gauge transformation. Substituting the wavefunction by

$$\tilde{\psi}(x_0, t_0) = e^{-iF_0 t_0 x_0/16\pi}\psi(x_0, t_0), \tag{5.3}$$

the Schrödinger equation reads $i\partial\psi/\partial t_0 = H(t_0)\psi$, with $H(t_0)$ the time-dependent Hamiltonian [43]

$$H(t_0) = \frac{1}{2}\left(\hat{p} - \frac{F_0 t_0}{16\pi}\right)^2 + \frac{V_0}{16}\cos(x_0), \tag{5.4}$$

and the momentum operator $\hat{p} = -i\partial/\partial x_0$. In the following, we analyze the Hamiltonian of Eq. (5.4) in the momentum basis. In order to decompose the Hilbert space into independent subspaces, Bloch decomposition can be used and for that the momentum eigenstates of the free particle ($V_0 = 0 = F_0$) for fixed quasi-momentum q within the Brillouin zone can be identified, i.e., $p = q + n$, p and q being indices in the momentum and quasi-momentum representations and $n \in \mathcal{Z}$. To calculate the time evolution of any momentum eigenstate

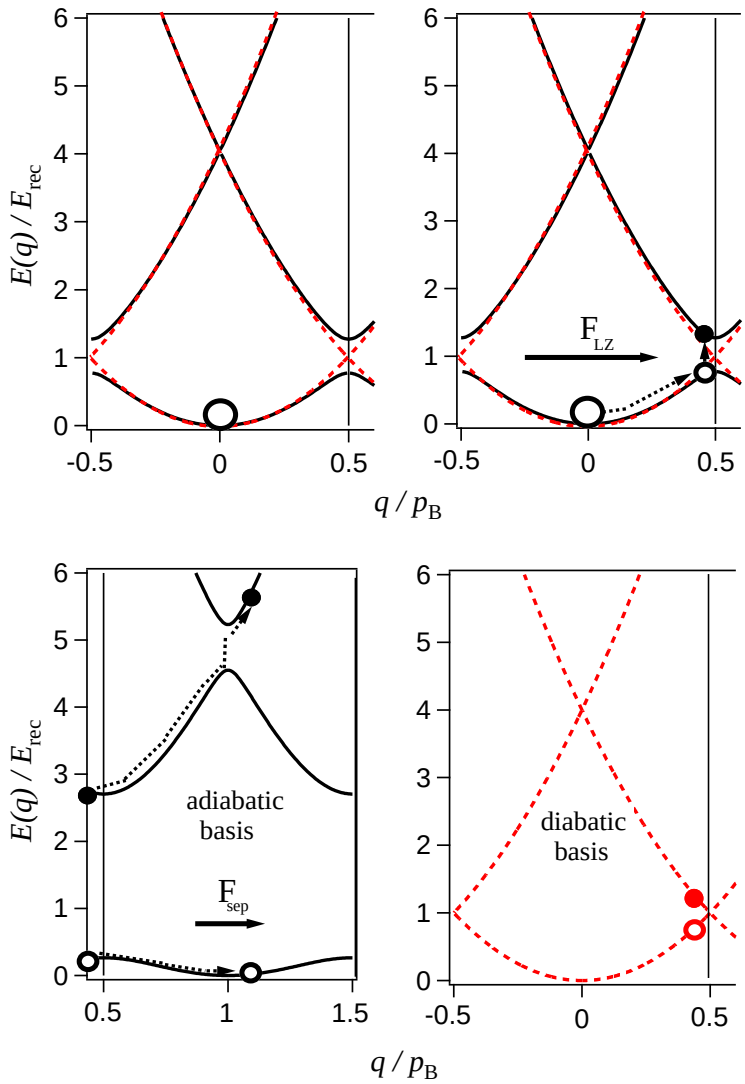

Figure 5.1: Schematic view of the band structure in the optical lattice potential and experimental protocols for measuring Landau–Zener dynamics in the adiabatic and diabatic bases. After the initial loading into the lattice and acceleration for a time t_{LZ} (top), measurements of the instantaneous populations in the two states are performed (bottom). In the top figures, the adiabatic (solid lines) and diabatic energies (dashed lines) for an optical lattice of depth $V_0 = 1$ are shown. This picture was adopted from [43] with courtesy of the corresponding authors.

$|p\rangle = |q+n\rangle$, the Hamiltonian H_{q} acting on the subspace with a given quasi-momentum index q is needed, as there is no transition between states with different q [43]

$$H_{\mathrm{q}} = \frac{1}{2}\begin{pmatrix} \ddots & & & & 0 \\ & (\tilde{q}-1)^2 & V_0/16 & & \\ & V_0/16 & (\tilde{q})^2 & V_0/16 & \\ & & V_0/16 & (\tilde{q}+1)^2 & \\ 0 & & & & \ddots \end{pmatrix}, \tag{5.5}$$

where $\tilde{q} = q - F_0 t_0/16\pi$. The full dynamics of the Wannier–Stark system can be locally approximated by a simple two-state model [43]

$$h_{\mathrm{q}} = \frac{1}{2}\begin{pmatrix} \tilde{q}^2 & V_0/16 \\ V_0/16 & (\tilde{q}+1)^2 \end{pmatrix}. \tag{5.6}$$

The two by two matrix h_{q} can be brought into the form of the Hamiltonian given by Eq. (3.2) by properly shifting the diagonal parts (e.g., shifting away the quadratic term in time t_0) as follows

$$h_{\mathrm{q}} = \frac{1}{2}\begin{pmatrix} -\tilde{q} & V_0/16 \\ V_0/16 & \tilde{q} \end{pmatrix}. \tag{5.7}$$

For $q = 0$ we have $\tilde{q} = -F_0 t_0/16\pi$, thus the following matrix is obtained

$$\frac{1}{8}\begin{pmatrix} 2F_0 E_{\mathrm{rec}} t_0/\pi\hbar & V_0/4 \\ V_0/4 & -2F_0 E_{\mathrm{rec}} t_0/\pi\hbar \end{pmatrix}. \tag{5.8}$$

The parameters α, ΔE and γ introduced in the Landau–Zener model of Eq. (3.2) can be expressed now in terms of considered system parameters: $\alpha = 2F_0 E_{\mathrm{rec}}^2/\pi\hbar = 4E_{\mathrm{rec}}/(\pi T_{\mathrm{B}})$, $\Delta E = V_0 E_{\mathrm{rec}}/2$, and $\gamma = 32F_0/\pi V_0^2$ [42, 43].

5.2 Deviation from Landau–Zener limit

The Landau–Zener theory predicting the asymptotic behavior of the tunneling probability can be used as a very good approximation for our system. It can be used at the avoided Landau–Zener crossing, this theory, however, does not take into account successive crossings. It only provides the initial and final probability of the transition or the survival probability but no details on what happens in between.

Short-time deviation

Short-time deviations from the universal exponential decay law given in Eq. (3.4) are observed [17, 42, 43]. The expression for the Landau–Zener tunneling rate derived above is based on a single transit of the atom through the region of an avoided crossing. However, for small tunneling probability the atom can undergo Bloch oscillations within a given band, leading to multiple passes through the Brillouin zone. The tunneling amplitudes can interfere constructively or destructively depending on the rate at which the atom traverses the Brillouin zone. This mechanism is responsible for the formation of tunneling resonances. For small accelerations the tunneling rate is small and the ultracold atoms can perform many Bloch oscillations before leaving the band. Therefore large deviations from the Landau–Zener prediction for the tunneling rate are to be expected. For a larger acceleration, the ultracold atoms leave the band quickly and the interference effects are less pronounced. For those cases the Landau–Zener prediction is a good approximation for the actual tunneling rate [22].

Limiting cases

There are some limiting cases, and experimental parameters, for which the simplified two-state model is not a good approximation for the Wannier–Stark system. The discrepancy is large for lattice depths larger than the energy scale E_{rec} of the system ($V_0 \gg 1$), where the gap between energy bands increases leading to quasi-flat bands and localized eigenstates. Therefore, several momentum eigenstates contribute with a non-negligible amount to the lowest energy eigenstate, and one would need to take into account more components in the Hamiltonian matrix. For lattice depth $V_0 \neq 0$, one can calculate the ground state of the Hamiltonian given in Eq. (5.5) approximately by using perturbation theory. Therefore, the ground state reads

$$|0\rangle = |0^{(0)}\rangle + \sum_{k\neq 0} |k^{(0)}\rangle \frac{\langle k^{(0)}|V|0^{(0)}\rangle}{E_0^{(0)} - E_k^{(0)}} + \cdots , \tag{5.9}$$

where $|0\rangle$ is the ground state and $|k^{(0)}\rangle$ are the momentum states, V is the potential energy. The ratio $V/(E_0^{(0)} - E_k^{(0)})$ also exists in the higher order terms. If it is large enough, then the states with index k will contribute in the calculation of the ground state. Therefore, the larger the potential is, the more higher momentum states contribute.

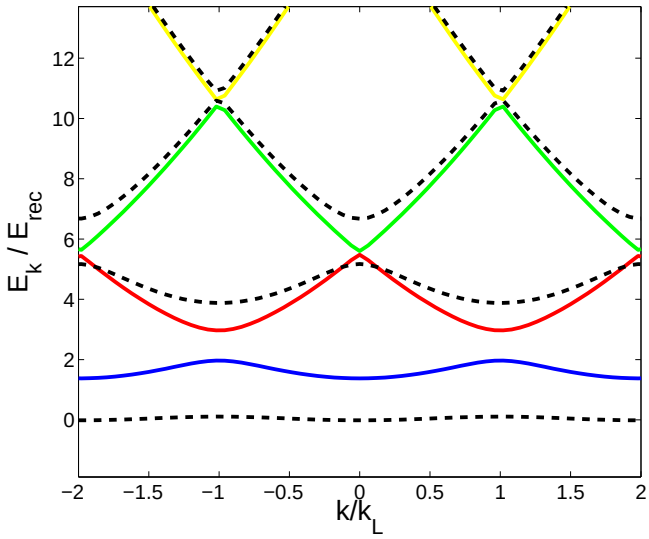

Figure 5.2: Bloch-band spectrum of the system Eq. (5.1) for $F = 0$ and a small $V_0 = 1$ (solid lines) and a large $V_0 = 4$ (dashed lines). The y-axis is scaled in the units of the recoil energy and the x-axis in the units of the laser wave vector. The bands are almost flat for larger potential depth.

Figure 5.2 illustrates the band structure for a small lattice depth V_0 (solid lines) and a large V_0 (dashed lines). As seen, the flat bands for larger lattice depths do not allow the picture of isolated avoided crossing and therefore, the Landau–Zener theory starts to break down.

Finite coupling duration

Before analyzing the results, an additional problem needs to be addressed, namely, the finite coupling duration as in [24], an experiment, takes necessarily a finite time for the measurement, whereas the standard Landau–Zener theory assumes that the time taken for the transition runs from $-\infty$ to ∞. The experimental finiteness of the sweep time T_{B} implies that for the initial state at a finite distance from the transition point, the diagonal and off-diagonal matrix elements in the system Hamiltonian are comparable. The experiment, which its data are presented in this chapter [42, 43], typically operates in the large time regime, meaning that the time intervals from the turn-on and the turn-off times to the crossing are larger than the jump time (see section 3.1.1). The presence of a jump time comparable to the Bloch time may modify the temporal evolution of the survival probability for the two mechanisms discussed in the following.

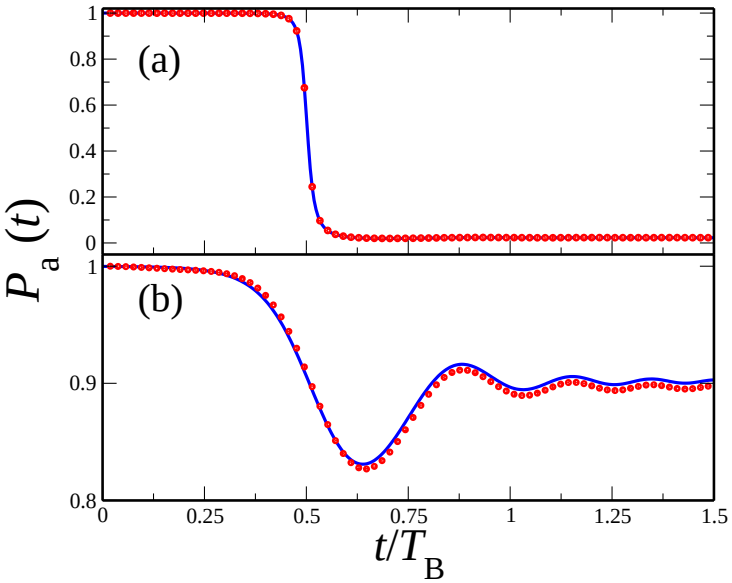

Figure 5.3: Comparison between the time evolution of the Landau–Zener model of Eq. (5.8) in the adiabatic, starting from initial ground states prepared at different time "distances" from the transition point. Survival probabilities measured for (a) $F_0 = 1.197$ and $V_0 = 0.3$, and (b) $F_0 = 1.197$ and $V_0 = 3.0$. The red dotted lines show the evolution obtained evolving the survival probability from the ground state in the adiabatic basis at $t = -\infty$; the blue solid lines illustrate the evolution obtained evolving the survival probability from the ground state which simulates a possible experimental initial state, i.e., the ground state in an adiabatic basis, at a finite time from the transition point. The survival probability is calculated by the method introduced in section 5.4.3. Data reproduced from [43] with courtesy of the corresponding authors.

Because at large γ, the ratio $\tau_{\mathrm{d}}^{jump}/T_{\mathrm{B}}$ between jump time and sweep time is given by $\pi\sqrt{F_0}/2$, large F_0 values may produce deviation in the resulting survival probability from the ideal theory of Landau–Zener.

It is not at all obvious that an initial state chosen as the adiabatic ground state at a finite time from the transition point (which is likely to be the initial experimental state) should coincide with the state obtained evolving from $t = -\infty$, projected onto the adiabatic basis. The survival probability simulating different initial states for the Landau–Zener model is computed as seen Figure 5.3. To calculated the time evolution of the survival probability, the Hamiltonian is integrated by the implicit method presented in chapter 4. Then by applying the method that is introduced in section 5.4.3, the survival probability is calculated by projecting the state of the system on the chosen basis. For the experimental

parameter set [43] which is also used for our calculations in the current chapter, the discrepancy is not very large, but certainly important for a precise description of the temporal evolution of the tunneling. Therefore, the approach of [40] yields some elegant theoretical results for the Landau–Zener transition, but care is needed in comparing them with the experiment due to the presence of the additional time scale connected to the finite distance between the experimental starting point and the transition point.

5.3 Survival probability in the ground band

The initial state is the relaxed condensate wave function prepared in the confining potential given by a three-dimensional harmonic trap $V_{\mathrm{trap}} = \frac{1}{2m}\left(\omega_\rho^2\rho^2 + \omega_x^2 x^2\right)$, with $\omega_x \ll \omega_\rho$. This latter condition forms an elongated Bose–Einstein condensate along the x-axis and hence a quasi one-dimensional system. Therefore, the relaxed condensate wavefunction in momentum space is given by $\Psi(p, t=0) = N \exp\left(-p^2/\Delta p^2\right)$, where N is the normalization constant. Then the condensate is loaded adiabatically into the optical lattice when the Stark force F equals zero. During the time evolution, ω_x is either switched off or relaxed to a small value $\omega_{x,rel}$ and the Stark force F is simultaneously switched on to induce the dynamics.

The Bose–Einstein condensate, shown with a circle in Figure 5.1, can be produced at the center of the Brillouin zone initially with a very small momentum distribution Δp in comparison with the characteristic momentum scale of the problem given by the width of the first Brillouin zone p_{B}. Due to the acceleration (constant force F) the Bose–Einstein condensate wave packet starts to move within the Brillouin zone and at the edge of the Brillouin zone most of the wave packet is reflected and gives rise to the Bloch oscillations with the period given by Bloch time T_{B}. A schematic illustration of the Brillouin zone with the first two bands is shown in Figure 5.4, the dark blue circle shows the initial wave packet and the light blue circles show the moving wavepacket. This picture demonstrates the process of acceleration and Bloch oscillations.

For a large enough force there is also a probability of tunneling of Bose–Einstein condensate atoms at the edge of the Brillouin zone, where the band gap is minimal. Therefore, part of the population can tunnel from the ground band, across the first band gap, to the next energy band and then escape from the system by successive tunneling events across the much smaller band gaps between the upper bands as seen in Figure 5.4. The remaining part of the wave packet continues moving within the ground band and performs Bloch oscillations. Tunneling events from the ground band to the next band occur after each Bloch period (as seen in Figure 5.5). The Landau–Zener theory, as in Eq. (3.4), pre-

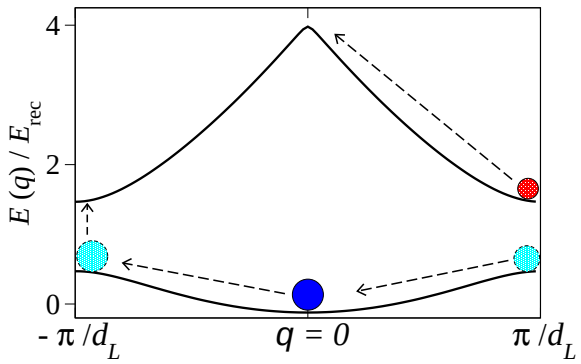

Figure 5.4: A Schematic illustration of the band structure for the first two bands forming the first Brillouin zone. The dark blue circle shows the Bose–Einstein condensate wave packet prepared initially at the center of the Brillouin zone. The light blue circles show the moving wave packet and the red circle represents the tunnelled part of the wave packet.

dicts the rate of decay of the survival probability of Bose–Einstein condensate in the ground band, for a comparable lattice depth and a force to the energy scale of the system (as mentioned in the previous section).

In order to study the Landau–Zener prediction for the tunneling of Bose–Einstein condensate from the ground band, we need to access the decay rate of the population from the ground band. In that respect, the time-dependence of the probability of the condensate to remain in the ground band, in which it has been initially prepared, is computed. Experimentally, the most easily measurable quantity is the momentum distribution of the condensate obtained from a free expansion after the evolution inside the lattice [27, 38, 42, 43]. Therefore, such a survival probability is best measured in the momentum space. From the time-dependent momentum distribution the survival probability $P_{\mathrm{a}}(t)$ in the adiabatic basis can be determined by projection of the evolved state $\Psi\left(p,t\right)$ on to the support of the initial state:

$$P_{\mathrm{a}}(t) = \int_{-p_{\mathrm{c}}}^{\infty} dp\, |\Psi(p,t)|^2 \,. \tag{5.10}$$

The function $\Psi(p,t)$ is the Bose–Einstein condensate wave function in momentum representation, and p_{c} is an ad hoc cut-off. For the results shown in Figure 5.5(a), $3p_{\mathrm{rec}}$ is a good choice for cut-off momentum p_{c} since three momentum peaks (shown by black curve), are initially significantly populated, corresponding to $-2\ p_{\mathrm{rec}}$, 0, and $+2\ p_{\mathrm{rec}}$. Eq. (5.10) can be interpreted as the projection of $\Psi(p,t)$ onto the support of the initially prepared condensate at $t=0$ (in the presence of the optical lattice but at $F=0$), which is illustrated by

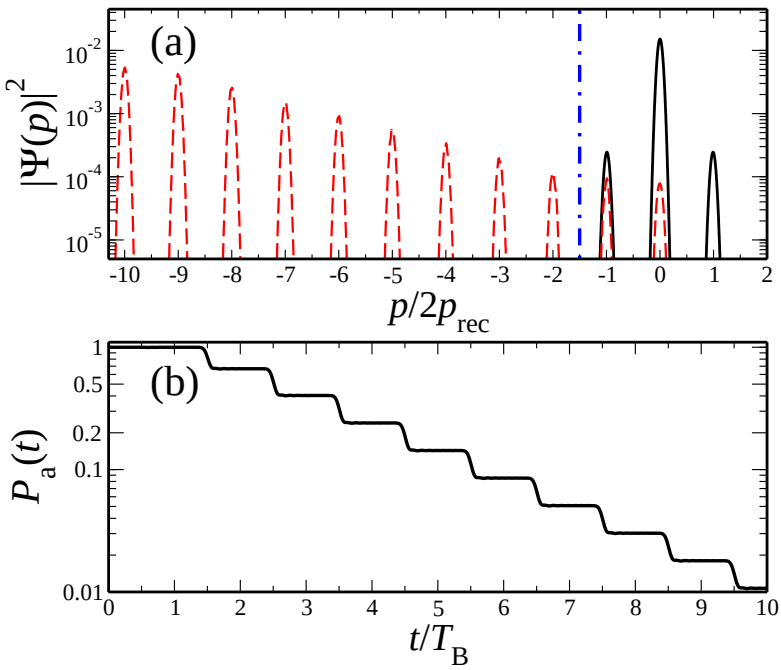

Figure 5.5: In (a) the momentum distribution at time $t = 10T_{\rm B}$ (dashed lines) starting from the initial momentum distribution (solid lines) under the action of a force directed towards negative p values. The vertical dash-dotted line shows the cut-off value $p_{\rm c} = 3p_{\rm rec}$ in the definition of Eq. (5.10). (b) Temporal evolution of the survival probability in the adiabatic basis using Eq. (5.10). Simulation parameters: $V_0 = 2.07$, $F_0 = 1.197$.

the black solid curve in Figure 5.5(a). The equidistant peaks of the momentum distribution shown by the red dashed curve in Figure 5.5(a) reflect the fact that the condensate moves with a constant acceleration due to the constant Stark force F. The height of the peaks is decreasing since part of the wave packet has tunnelled out of the ground band.

The temporal evolution of the survival probability calculated using Eq. (5.10) is shown in Figure 5.5(b). A very nice step structure can be seen in the survival probability shown in this Figure. Such step structures reflect the Bloch oscillations and Landau–Zener tunneling. Figure 5.7 shows the time-resolved calculations together with the experimental measurements (done in Pisa BEC group) of the survival probability for the lattice depth $V_0 = 1.0\ E_{\rm rec}$ and the force $F_0 = 0.383$ [42, 43]. The red dashed line is an exponential decay curve $\exp(-\Gamma_{\rm LZ}t)$ for the systems parameters. The parameter $\Gamma_{\rm LZ}$ is Landau–Zener's prediction of the transition rate given in Eq. (2.37). As seen in this figure the experimental and the numerical results for the survival probability $P_{\rm a}(t)$, which

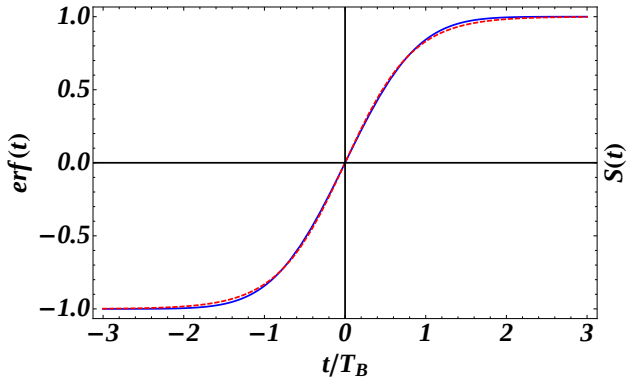

Figure 5.6: The error function $\mathrm{erf}(t)$ (blue solid line) and the sigmoid function $S(t)$ (red dashed line). The width of the sigmoid function was rescaled by 0.42. The function is similar to the step we see for our survival probability.

match each other perfectly, show clear deviation from the exponential curve due to the step structure.

Each step can be well fitted by a step function. In fact the step is like a error function $\mathrm{erf}(t)$, which arises from a integration over a Gaussian distribution $\exp(-p^2)$ with $\Delta p = 1$. This Gaussian distribution corresponds to the initial state of the Bose–Einstein condensate prepared in a trap and is written as $\exp(-p^2/\Delta p)$, where $/\Delta p$ is the width of the condensate's momentum distribution. As explained in the beginning of this section, due to the acceleration, this the condensate with a Gaussian distribution sweep the Brillouin zone (see Figure 5.4). Therefore, in order to calculate the survival probability, this Gaussian function is integrated over the Brillouin zone which gives rises to a error function. The error function has a sigmoid shape given by function

$$P_{\mathrm{a}}(t) = 1 - \frac{h}{1 + \exp((t_0 - t)/\Delta t)}, \tag{5.11}$$

where t_0 is the position of the step (which can deviate slightly from the expected value of $0.5\,T_{\mathrm{B}}$, e.g. due to a non-zero initial momentum of the condensate), h is the step height and Δt represents the width of the step. This quantities are shown in Figure 5.7. The error function and the sigmoid function can be fitted with each other by scaling the width Δt of the sigmoid function by a factor of 0.42. In this way the sigmoid function is relevant to the same Gaussian distribution as the one above. Figure 5.6 shows these two function fitted on top of each other, by rescaling the width Δt in the Sigmoid function.

Therefore, the step function given by the Sigmoid function in Eq. (5.11) will

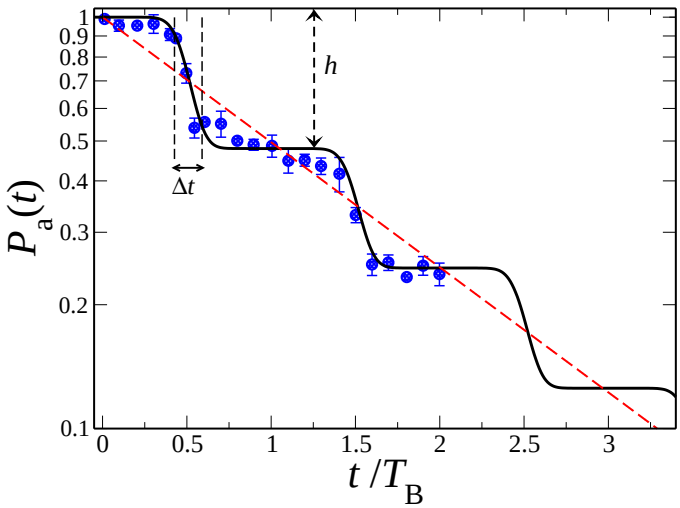

Figure 5.7: Time-resolved calculations of Landau–Zener tunneling for the lattice depth $V_0 = 1\ E_{\rm rec}$, the force $F_0 = 0.383$ and $p_{\rm c} = 3\ p_{\rm rec}$. The black solid line is the numerical simulation using Eq. (5.10) for the experimental protocol (blue circles) and the red dashed line is an Landau–Zener exponential decay prediction for our systems parameters. The height of the step $\rm h$ and its width Δt (as introduced in Eq. (5.11)) are shown by vertical dashed lines for the first step. Data reproduced from [42] with courtesy of corresponding authors.

be used, as seen in section 5.4.1, to fit the steps of the survival probability for various system parameters and the results are compared to the Landau–Zener prediction given in Eq. (3.4).

Eq. (5.10) measures the survival probability only once the Bose–Einstein condensate wave packet $\Psi(p,t)$ has extended beyond $-p_{\rm c}$ ($= 3p_{\rm rec}$ in Figure 5.5(a)). Therefore, one must resort to the acceleration theorem [21, 41], to identify time t with $t - T_{\rm B}$ (see section 5.1). Hence time must be rescaled by the traversal time of the Brillouin zone $T_{\rm B}$. The impact of changing the cut-off momentum $p_{\rm c}$ on the survival probability is shown in Figure 5.8. This figure sheds a light on the above statement about rescaling time. As seen, for a small $p_{\rm c}$ some oscillations appear on top of the steps which are in fact numerical artifact. They arise because the wave packet oscillates in and out of the measurement window. Therefore, some artificial oscillation appear on top of the step structure. By choosing larger $p_{\rm c}$ (larger measurement window) this effect can be diminished or eliminated. The choice of $p_{\rm c}$ does not affect the tunneling rate of Bose–Einstein condensate from the ground band. This will be demonstrated by comparing the height of a step of the calculated survival probability to the Landau–Zener prediction, as can be seen in Figure 5.9.

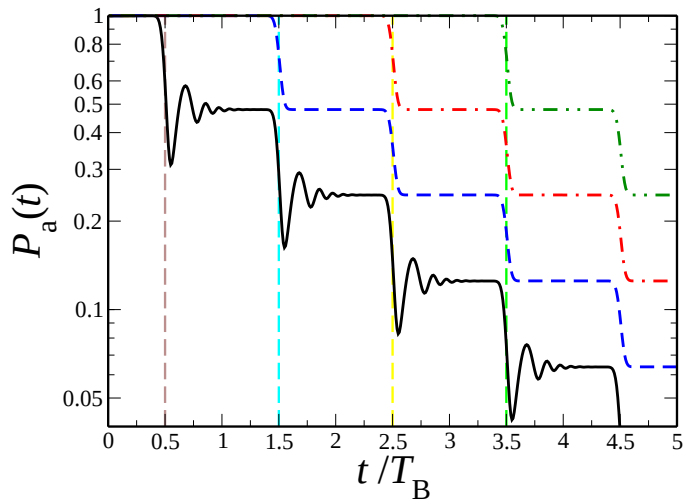

Figure 5.8: Temporal evolution of the survival probability in the adiabatic basis using the definition of Eq. (5.10), for $V_0 = 1.0\ E_{\rm rec}$, $F_0 = 0.383$ and various $p_{\rm c}$. The vertical dashed lines shows the cut-off values: $p_{\rm c} = 1\ p_{\rm rec}$ (brown dashed line), $3\ p_{\rm rec}$ (cyan dashed line), $5\ p_{\rm rec}$ (yellow dashed line), and $7\ p_{\rm rec}$ (green dashed line).

According to the Landau–Zener theory increasing the force and/or decreasing the band gap, through decreasing the lattice depth V_0, leads to a faster decay of the Bose–Einstein condensate in the ground band. The impact of different system parameters and of the calculation basis on the tunneling probability is studied in the following section.

5.4 Coherent control of Landau–Zener tunneling

It is possible to control the Landau–Zener tunneling of the Bose–Einstein condensate from the ground band in the linear system, in the absence of atom-atom interactions, by

- changing the system parameters, such as external force F_0, and the amplitude of the optical lattice V_0 (see Figures 5.9 and 5.10),
- exploiting resonantly enhanced tunneling (RET) between degenerate Wannier–Stark states at $\Delta E \approx mFd_{\mathrm{L}}$ with m being an integer number as described in section 2.4.1 (see Figure 5.10) [25],
- changing the initial condition by changing the trap frequencies and hence preparing the Bose–Einstein condensate with different widths Δp of its initial momentum distribution (see Figure 5.12),
- performing experiments in different bases: (i) in the adiabatic basis of the lattice eigenstates (see Figure 5.13) and (ii) in the diabatic basis of the free-particle momentum eigenstates (see Figure 5.14).

In the following each of the above mentioned possibilities are introduced and discussed in detail and their effects on the tunneling probability of the condensate in engineered tilted optical lattices is studied.

5.4.1 Impact of lattice depth and the Stark force

As predicted by Landau–Zener theory (Eq. (3.4)) the tunneling rate from the ground band depends on the system parameters such as the band gap between the ground band and the first excited band, and the force exerted on the atoms. This can be checked easily in the system of Bose–Einstein condensate changing the lattice depth and the tilting force. Figure 5.9(a) shows the first Landau–Zener tunneling step for different lattice depths V_0, measured in units of E_{rec} at a given force F_0. As seen, for a fixed force the height of the step increases by reducing the lattice depth since it leads to smaller band gaps between the bands. This agrees also with Landau–Zener prediction for the tunneling transition given in Eq. (3.4). The numerical results calculated using Eq. (5.10) and the results of experimental measurements demonstrate the same behavior and the same height of the step [42].

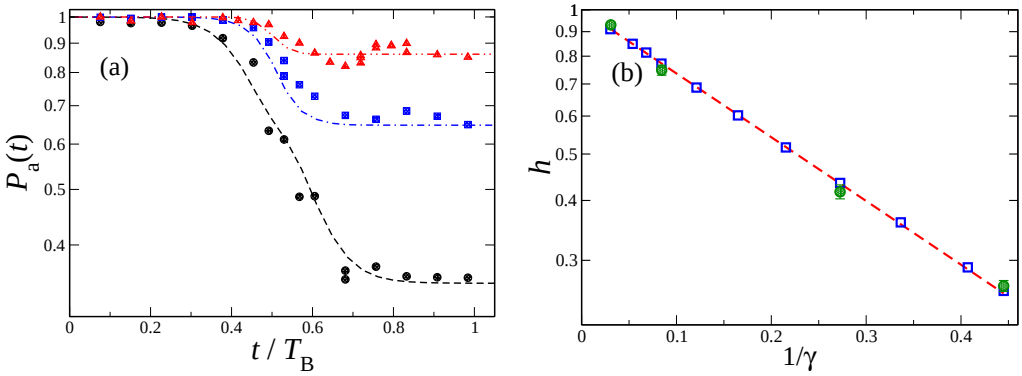

Figure 5.9: (a) Time-resolved calculations of the survival probability (using Eq. (5.10)) for the Bose–Einstein condensate, with $\Delta p \approx 0.2\, p_{rec}$, tunneling in an optical lattice at fixed dimensionless force $F_0 = 1.197$ and different lattice depths: $V = 2.3\, E_{\rm rec}$ (dot-dot-dashed red line), $1.8\, E_{\rm rec}$ (dot-dashed blue line), $1\, E_{\rm rec}$ (dashed black line). For the Bose–Einstein condensate evolution the crossing time is $t = T_{\rm Bloch}/2$, where the step of the survival probability is one half of the final value. The experimental results are reproduced from [42] and shown by red filled triangles, blue filled squares, and black filled circles, respectively. The lattice depth for the numerical simulations was corrected by up to $\pm 15\%$ with respect to the experimentally measured values to give the best possible agreement. (b) Step height $\rm h$ as a function of the inverse adiabaticity parameter $1/\gamma$ for varying lattice depth and $F_0 = 1.197$ [42]. The numerical results are shown by open squares in comparison with experimental results (green circles). The dashed line is the prediction of Eq. (3.4) for the Landau–Zener tunneling probability. Data reproduced from [42] with courtesy of the authors

The steps in Figure 5.9(a) can be fitted using the step function given in Eq. (5.11). Figure 5.9(b) shows the step height $\rm h$ for various amounts of adiabaticity parameter $\gamma = 32 F_0/\pi V_0^2$ (see section 5.1). The results from fitting the numerical calculations (blue open squares) and from fitting the experimental measurements (green filled circles), for a variety of values of lattice depths V_0 and forces F_0 [42, 43], show almost perfect agreement with each other and with the theoretical prediction shown by the red dashed line. This agreement admits that Eq. (3.4) (red dashed line) correctly predicts the height $\rm h$ of the step.

As expected from Eq. (3.4) and confirmed in Figure 5.9, increasing the tilting force leads to more and more tunneling of the atoms from the ground band. On the other hand, depending on the system parameters, one can tune into a special condition for which the rate of the tunneling is enhanced. As described in section 2.4.1, this condition is fulfilled when an integer multiple of the energy scale of the tilting force $F d_{\rm L}$ matches the energy difference between the initial state

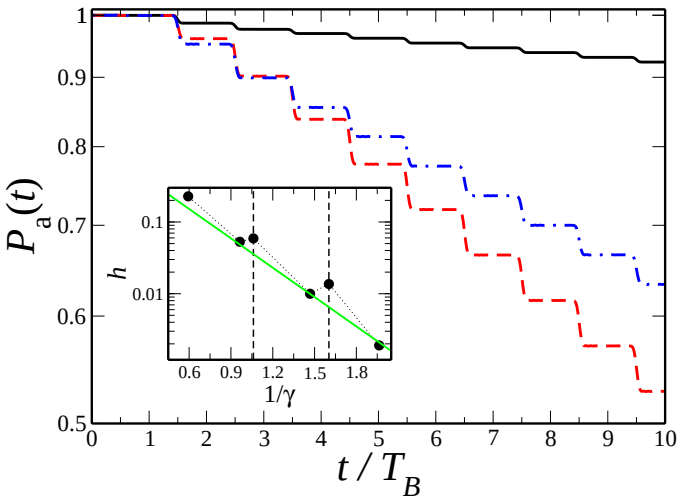

Figure 5.10: Time resolved survival probability of the Bose–Einstein condensate in the ground band, for a lattice depth $V_0 = 4\ E_{\rm rec}$ and a narrow width of the initial momentum distribution of the Bose–Einstein condensate cloud, $\Delta p = 0.1\ p_{\rm rec}$, and various Stark forces. For non-RET condition: $F_0 = 1.07$ (solid line) and $F_0 = 1.63$ (dash-dotted line); for RET condition: $F_0 = 1.48$ (dashed line). Inset: height of one step (of data as shown in the main panel) for fixed $V_0 = 4\ E_{\rm rec}$ and various γ. The step height as predicted by Eq. (3.4) (solid line) in comparison with the numerically obtained values (filled circles). A significant deviation from the Landau–Zener prediction can be observed at values of $1/\gamma$ corresponding to RET conditions and marked by the vertical dashed lines [44].

and the final state, i.e., approximately the band gap ΔE. This phenomenon is known as resonantly enhanced tunneling (RET). A deviation from the Landau–Zener prediction is expected in this case. In order to see whether the tunneling probability given by the standard Landau–Zener tunneling probability correctly predicts the height of a step corresponding to a single tunneling event, we fit the function given in Eq. (5.11) to the steps of the survival probability and extract the height of each step. The result and the comparison to the Landau–Zener prediction is shown in the inset of Figure 5.10. When the system parameters are in the RET condition (e.g., $1/\gamma \approx 0.59,\ 1.05$ and 1.6), the height of the steps of the survival probability increases and shows a significant deviation from the Landau–Zener prediction given in Eq. (3.4). This behavior is seen in Figure 5.10 where the survival probability for $F_0 = 1.48$ decays much faster than for the other two cases.

5.4.2 Impact of initial condition

The other parameter which can be used to control time evolution of the survival probability is the width Δp of the initial momentum distribution. By changing the trap frequencies ω_x and ω_ρ of the confining potential one can prepare the initial distribution with different widths (see section 5.3).

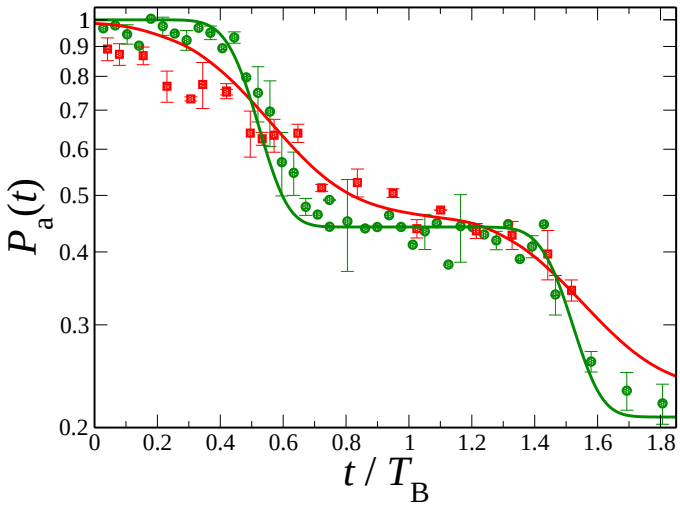

Figure 5.11: The survival probability of the Bose–Einstein condensate in the ground band for a lattice depth $V_0 = 1.0\ E_{\rm rec}$, a constant Stark force $F_0 = 0.383$, and various widths of the initial momentum distribution of the Bose–Einstein condensate cloud, $\Delta p \approx 0.2\ p_{\rm rec}$ (green solid line); $\Delta p \approx 0.7\ p_{\rm rec}$ (red solid line). The experimental results are shown by green filled circles and red filled squares, respectively. Data are reproduced from [42] with courtesy of the authors.

The effect of initial condition of the system on the survival probability $P_{\rm a}(t)$ is studied numerically and also experimentally by making time-resolved measurements of the survival probability of the created condensate with different initial widths [42]. Figure 5.11 shows numerical and experimental results for the survival probability of the condensate with narrow initial widths of the momentum distribution $\Delta p = 0.2\ p_{\rm rec}$ and a broad initial width $\Delta p = 0.7\ p_{\rm rec}$, in the tilted optical lattice with depth $V_0 = 1.0\, E_{\rm rec}$ and force $F_0 = 0.383$. As seen for the narrow initial momentum distribution $\Delta p = 0.1\ p_{\rm rec}$ a clear step structure in time-evolution of the survival probability similar to the one shown in Figure 5.7 is observed. The steps are smooth and partly washed out since the wave packet reaches the edge of the Brillouin zone earlier when it has a broader initial momentum distribution (e.g., $\Delta p = 0.6\ p_{\rm rec}$). Therefore, the tunneling events start earlier and hence the decay of the survival probability as seen in Figure 5.7. Still,

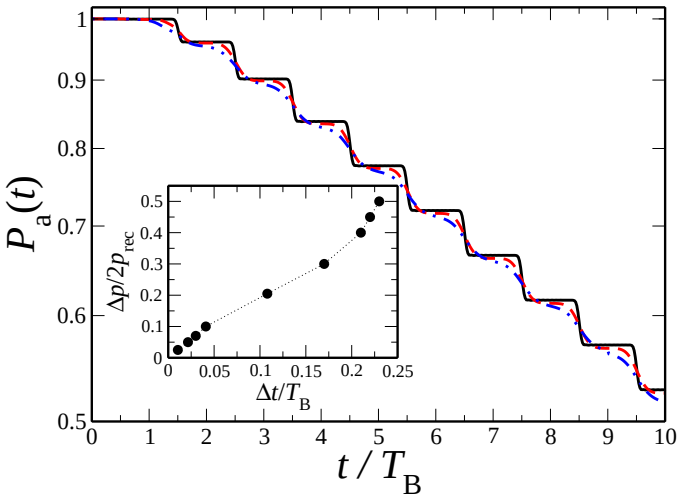

Figure 5.12: The survival probability of the Bose–Einstein condensate in the ground band for a lattice depth $V_0 = 4.0\ E_{\rm rec}$, a constant Stark force $F_0 = 1.48$, and various widths of the initial momentum distribution of the Bose–Einstein condensate cloud, $\Delta p = 0.1\ p_{\rm rec}$ (solid line); $\Delta p = 0.4\ p_{\rm rec}$ (dashed line); $\Delta p = 0.6\ p_{\rm rec}$ (dash-dotted line). Inset: step width Δt for several Δp (filled circles). The step width Δt is the distance between the two vertical dashed lines shown in Figure 5.7. Data reproduced from [44] with courtesy of all the authors.

the remnants of the steps cause a local deviation from the exponential decay of the tunneling probability. Nevertheless, the survival probability exhibits an exponential decay globally in time, i.e., on large time scales.

The main part of Figure 5.12 shows the survival probability after $10\ T_{\rm B}$ for three values of Δp. In order to test the dependence of the measured step width Δt on the width Δp of the momentum distribution of the condensate, condensates with several different widths are created. The inset of Figure 5.12 demonstrates such dependence. Fitting the function given in Eq. (5.11) to the steps, it is possible to calculate their step width Δt. As expected, the larger the initial momentum width of the condensate, the larger the step width.

The widths Δt corresponding to the steps shown in the inset of Figure 5.12 should, according to our interpretation, reflect the "tunneling time" or "jump time" for Landau–Zener tunneling during which the probability of finding the atoms in the lowest energy band goes from $P_{\rm a}(t = 0) = 1$ to its asymptotic Landau–Zener value $P_{\rm LZ}(\infty)$ given in Eq. (3.4). Using the jump time given Eq. (3.5), which is the jump time in the adiabatic basis defined by Vitanov [40], and implementing a sigmoidal function given in Eq. (5.11) for $P_a(t)$ leads to $\tau_a^{jump} = 4\Delta t$. For large values of γ, which is the regime of our calculations, the

theoretical jump time is given by $\tau_a^{jump}/T_B \approx \Delta E/(4\,E_{\rm rec})$, where ΔE is the band gap. From the sigmoidal fits we retrieve $\tau_a^{jump}/T_{\rm B} \approx 0.15 - 0.35$. The theoretical values applying Vitanov theory [40] for parameters are in the region of $0.1 - 0.15$. We interpret this discrepancy as being due the fact that the condensate does not occupy one single quasi-momentum but is represented by a momentum distribution of a finite width $\Delta p \gtrsim 0.2\,p_{\rm rec}$ due to the finite number of lattice sites (around 50 in the experimental results presented in this chapter) it occupies and the effects of atom-atom interactions. The simulation can be used by preparing a narrow initial distribution and shows that for a vanishing momentum width, the step width still remains finite (see the inset of Figure 5.12). However, the numerical error grows towards the regime of very narrow initial distribution (e.g., for $\Delta p < 0.05\,p_{\rm rec}$, the error in $Err(\Delta t) \approx 10^{-2}$). As mentioned in section 3.1.1, the jump time measure is affected due to the different time scales appear in the time evolution of the survival probability, e.g., the oscillation time and the relaxation time of these oscillations as can be seen in Figures presented in the next section. It also depends on the method of calculation and the basis which the measurements are performing on. In the following section, the survival probability measurements in different basis are presented.

5.4.3 Calculation in different bases

Using different experimental protocols,it is possible to perform experiments both in the adiabatic basis of the lattice eigenstates and in the diabatic basis of the free-particle momentum eigenstates. Numerically, the calculations can be done in any chosen basis in experiments.

While many experimental results showed a very good agreement with numerical simulations based on Eq. (5.10), c.f. [37, 38], a better numerical method is needed for the new generation of experiments [42, 43]. The dashed lines in Figure. 5.13 were produced using $P_{\rm a}(t)$ of Eq. (5.10). These simulations well reproduce the height of the steps in agreement with the Landau–Zener prediction given in Eq. (3.4). They do not, however, reproduce the oscillations of the experimentally measured survival probability, due to the artificial cut-off used for evaluating $P_{\rm a}(t)$ in Eq. (5.10). While the sequence of steps, corresponding to a sequence of Landau–Zener tunneling events, is seen in Figures 5.5(b) and 5.7, no oscillations are visible. To reproduce the oscillatory behavior of the experimental data as in Figure 5.13, instead of Eq. (5.10) the survival proability $P_{\rm a}(t)$ in the adiabatic basis is determined in the following way: $|\phi(n=0,q)\rangle$ shall denote the ground state of the Hamiltonian given in Eq. (5.5), for the quasi momentum q, as shown also in the lower left panel of Figure 5.1. Then the adiabatic survival probability is just the projection of the condensate wave function $\Psi(p,t)$ onto

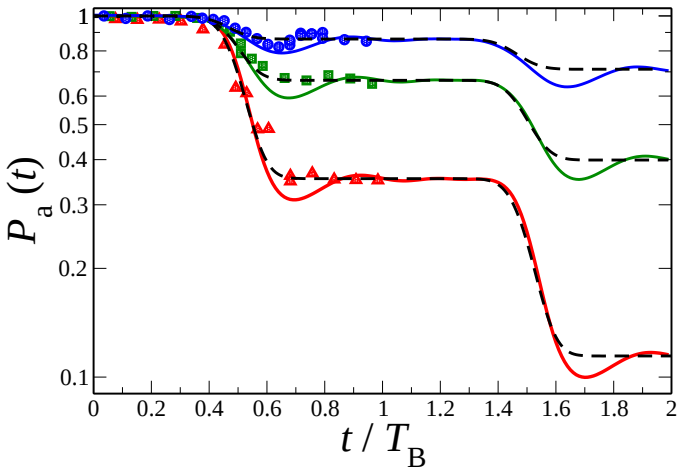

Figure 5.13: Time-resolved calculations of the adiabatic survival probability for the Bose–Einstein condensate tunneling in an optical lattice at fixed $F_0 = 1.197$, and different lattice depths: $V_0 = 2.8$ (experimental results: blue circles), $V_0 = 2.07$ (experimental results: green squares), $V_0 = 1.3$ (experimental results: red triangles). For the Bose–Einstein condensate evolution, the crossing time is $t = T_{\rm Bloch}/2$, where the step of the survival probability is one half of the final value. The dashed and solid lines are the results of numerical simulations using the cut-off given in Eq. (5.10) and the adiabatic method given in Eq. (5.12), respectively. The initial width of the condensate being $\Delta p \approx 0.2\, p_{\rm rec}$. The lattice depth for the numerical simulations was corrected by up to $\pm 15\%$ with respect to the experimentally measured values to give the best possible agreement. The experimental data are adopted from [42, 43] with courtesy of all the corresponding authors.

$\phi(n = 0, q)$ integrated over the full Brillouin zone [43], i.e.,

$$P_{\rm a}(t) = \int_{-p_{\rm rec}}^{p_{\rm rec}} dq |\langle \Psi(p = q, t) | \phi(0, q) \rangle|^2. \tag{5.12}$$

The solid lines in Figure 5.13 show $P_{\rm a}(t)$ calculated using Eq. (5.12). As seen, an oscillatory behavior now appears on top of the steps. However the asymptotic value of $P_{\rm a}(t)$ for each step, i.e., the height of the steps, remains the same for both methods of calculating the survival probability.

Figure 5.13 shows a typical time dependence of the survival probability in adiabatic basis, similar to that predicted in [40]. Notice that in the Bose–Einstein condensate case the crossing occurs at the time $t = T_{\rm B}/2$. The $t \to \infty$ asymptotic value is given by Eq. (3.4).

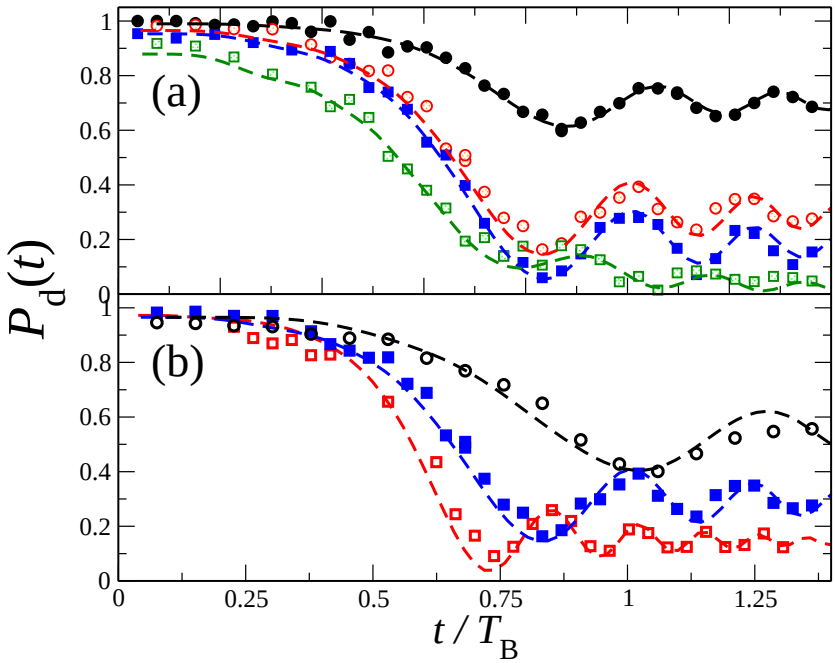

Figure 5.14: Time-resolved measurements of Landau–Zener tunneling in the diabatic basis. (a) Fixed force $F_0 = 1.197$ with different lattice depths $V_0 = 1.3$ (black filled circles), 2.07 (red open circles), 2.8 (blue filled squares) and 4 (green open squares). (b) Fixed lattice depth $V_0 = 2.07$ with different forces: $F_0 = 2.394$ (black open circles), 1.197 (blue filled squares) and 0.599 (red open squares). The dashed colored lines are the results of numerical simulations based on Eq. (5.13) which nicely reproduce the experimental data. The experimental data are adopted from [43] with courtesy of all the corresponding authors.

It is possible to make analogous measurements experimentally in the diabatic basis of the unperturbed free-particle wave functions (plane waves with a quadratic energy-momentum dispersion relation) by abruptly switching off the lattice and the dipole trap after the first acceleration step (with the Bose–Einstein condensate initially prepared in the adiabatic basis, which, far away from the band gap, is almost equal to the diabatic basis). Following the procedure sketched in the lower right panel of Figure 5.1, the survival probability determined in the diabatic basis of free momentum eigenstates is given by

$$P_{\mathrm{d}}(t) = \int_{-p_{\mathrm{rec}}}^{p_{\mathrm{rec}}} dq |\langle \Psi(p=q,t)|p=q\rangle_{V=0}|^2, \tag{5.13}$$

with $p = q$ within the first Brillouin zone. The state $|p = q\rangle$ shall denote the momentum eigenstates, which are the eigenstates of the Hamiltonian given in

Eq. (5.5) for zero potential $V = 0$. Eq. (5.13) is used to simulate the experimental results and all the results are shown in Figures 5.14(a) and (b) for various lattice depths and tilting forces. The numerical results computed using Eq. (5.13) and the experimental results show perfect agreement in all the cases. As in the adiabatic case, a step of the survival probability around $t = 0.5\,T_{\mathrm{B}}$ is clearly seen, as well as strong oscillations for $t > 0.5\,T_{\mathrm{B}}$. These oscillations are much stronger and visible for a wider range of parameters in the diabatic basis than in the adiabatic basis [40] (see the results for $V_0 = 2.8$ in Fig. 5.13, which is confirmed by our numerical simulations).

5.5 Impact of atom-atom interactions

In the regime of weak atom-atom interactions as described in section 2.1.2 the effect of interactions is studied in the mean-field regime based on the Gross–Pitaevskii equation. The Gross–Pitaevskii equation can describe the dynamics of the entire Bose–Einstein condensate in terms of an equation of motion for a single particle wave function. Due to the nonlinear term in the Gross–Pitaevskii Hamiltonian, the coordinates are coupled and it is not possible to separate the Hamiltonian in different coordinates.

As mentioned in section 5.4.2, experimentally, the initial state is the relaxed condensate wave function prepared in a three-dimensional harmonic trap $V_{\mathrm{trap}}(\vec{r}) = \frac{1}{2M}\left(\omega_\rho^2\rho^2 + \omega_x^2 x^2\right)$, with $\omega_x \ll \omega_\rho$ which leads to formation of an elongated Bose–Einstein condensate with cylindrical symmetry, and then loaded adiabatically into the optical lattice. Therefore, the following three-dimensional Gross–Pitaevskii equation describes the dynamics of interacting Bose–Einstein condensate atoms in a tilted quasi one-dimensional periodic potential $V(x)$:

$$H = -\frac{\hbar^2}{2M}\nabla_{\vec{r}}^2 + V_{\mathrm{trap}}(\vec{r}) + V(x) + gN_0\left|\Psi(\vec{r},t)^2\right| + Fx. \tag{5.14}$$

The third term in the Hamiltonian is the nonlinearity, which makes the equation different from the Schrödinger equation. As mentioned in section 2, $g = 4\pi\hbar^2 a_{\mathrm{s}}/M$ is the coupling constant which is proportional to the scattering length a_s and determines the strength of atom-atom interactions, where $4\pi\hbar^2 a_{\mathrm{s}}/(M\,E_R) \approx 2.45\times10^{-21}\ \mathrm{m}^3$, with $a_s = 53\times10^{-10}\ \mathrm{m}$ and $M = 1.44\times10^{-25}\ \mathrm{kg}$ for rubidium 87. The number of atoms in the condensate is given by N_0 and $|\Psi(\vec{r},t)^2|$ is the local atomic density. As an estimate for the nonlinear term in Eq. (5.14), we define $C \equiv gN_0\left|\Psi(\vec{r},t)^2\right|_{\mathrm{peak}}/E_{\mathrm{rec}}$ at the peak density of the initial state.

The survival probability for various quantities of atoms in the condensate is shown in Figure 5.15. The system parameters are chosen in a way to fulfill the RET condition (see section 2.4.1). The RET condition already implies that the tunneling probability of the condensate to higher bands is resonantly enhanced. Nevertheless, as shown in Figure 2.7, seen in the inset if Figure 5.15, an overall enhancement of the tunneling is expected to be seen in the presence of repulsive interactions. The following effects can be seen by increasing the strength of a repulsive interaction ($g > 0$) in the system [36, 37, 38] by

- enhancement of the tunneling rate,
- deviation from mono-exponential decay,
- washed out steps (corresponding to damped Bloch oscillations).

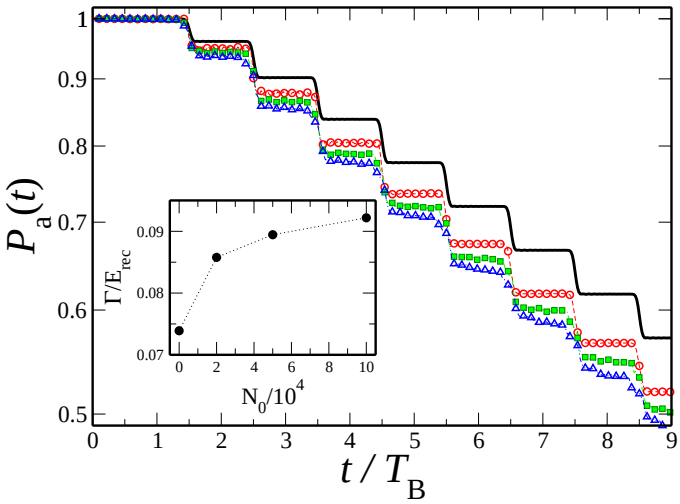

Figure 5.15: Nonlinear time resolved survival probability in the ground band for $V_0 = 4.0\ E_{\rm rec}$ and $F_0 = 1.48$ (RET), with a narrow width of the initial momentum distribution of the Bose–Einstein condensate $\Delta p = 0.1\ p_{\rm rec}$, and composed of the following number of atoms prepared in a trap with $\omega_{\rm x} = 2\pi \times 50$ Hz and $\omega_\rho = 2\pi \times 100$ Hz: $N_0 = 2 \times 10^4$, $C \approx 0.2$ (open circles); $N_0 = 5 \times 10^4$, $C \approx 0.32$ (filled squares); $N_0 = 1 \times 10^5$, $C \approx 0.42$ (open triangles) as compared to the linear case $g_{\rm 3D} = 0$ (solid line). Inset: Decay rate of the survival probability Γ at RET condition vs. N_0 (filled circles). Data reproduced from [44] with courtesy of all the corresponding authors.

According to results shown in Figure 5.15 for a RET case and the experimental results of [37, 38], the temporal behavior of the survival probability depends on the strength of atom-atom interactions. As can be found with more details in [36, 37], the enhancement of the decay rate is generic for repulsive interactions. The scaling of the decay rate as a function of nonlinearity is yet more interesting in the RET case (see the inset of Figure 5.15). We can quantify the decay rate Γ of the survival probability by globally fitting an exponential decay function to the step-like curves of the survival probability. Such rates, for various nonlinearities, are depicted in the inset of Figure 5.15. A repulsive interaction initially enhances the interband tunneling probability of the ultracold atoms [36]. Using the effective potential given in Eq. (2.42), it is possible to explain the enhancement of the tunneling rate. According to this effective potential the band gap between the ground band and the first excited band is modified in the presence of a nonlinear term, since the band gap is now $\Delta E \approx V_{\rm eff}/2$ [41]. Stronger atom-atoms interactions gives the smaller effective band gap, and therefore more atoms can tunnel to higher bands.

Since the tunneling events occurring at different integer multiples of the Bloch

period are correlated by the presence of the nonlinearity, a clear deviation from the mono-exponential decay is observed. A continuous change in the density of the condensate in time due to escaped particles from the system leads to a decreasing impact of the nonlinearity. Therefore, the time local rate of decay systematically decreases as the time increases. Additionally, the nonlinearity leads to a dephasing and damping of the Bloch oscillations, not discussed here, but a discussion of this phenomenon can be found in [27, 35, 130, 131]. Essentially, It is possible to observe persistent Bloch oscillations when minimizing the effect of interactions [131]. Dephasing effects occur due to the mean-field interaction in a Bose–Einstein condensate. In order to quantify the dephasing of Bloch oscillations, one can determine for each Bloch period the width Δp of the momentum distribution [131]. For minimal interaction strength, no broadening of the distribution is observed. The rate of broadening then increases with increasing interaction strength. Due to interactions between the atoms, Bloch oscillations of Bose–Einstein condensates suffer, in contrast to the case of fermions [130], from dynamical instabilities [132]. In the outer half of the Brillouin zone the nonlinear coupling leads to an exponential growth of small perturbations. They are responsible for a damping of the Bloch oscillations.

5.6 Summary

It is possible to control the Landau–Zener tunneling probability of the ultracold atoms from the ground band in tilted optical lattices. The complete control over the parameters of the lattice makes it possible to measure the tunneling dynamics in the adiabatic and diabatic bases, by using different measurement methods. This control is possible by changing the system parameters such as the lattice depth and the Stark force, or by changing the initial condition which is given by the initial width of the momentum distribution of the Bose–Einstein condensate. All the mentioned parameters can be easily tuned experimentally. Furthermore, our calculations showed that atom-atom interactions affect the Landau–Zener tunneling probability and a repulsive interaction typically leads to an enhancement of the Landau–Zener tunneling of the ultracold atoms from the ground band. The presented results confirm the existence of a finite temporal width for the transition in both bases (diabatic and adiabatic bases) and of strong oscillations of the survival probability in the diabatic basis. Both of these features are backed up by numerical simulations taking into account details of the experimental protocol.

Chapter 6

Results 2: Landau–Zener tunneling in time-dependent stochastic potentials

The dynamics of non-interacting Bose-Einstein condensates in tilted optical lattices are well-described by the Wannier–Stark Hamiltonian given in Eq. (5.1). It was shown in the previous chapter that the Landau–Zener tunneling probability can be manipulated by changing the initial condition and by engineering the system parameters such as the lattice depth and the Stark force. In this chapter, the dynamics of Bose–Einstein condensates in time-dependent stochastic optical lattices is studied. It will be shown that a controlled time-dependent noise is a further handle to engineer the interband tunneling.

6.1 Hamiltonian with a time-dependent stochastic potential

In the absence of atom-atom interactions, the temporal evolution of a Bose–Einstein condensate loaded into a one-dimensional potential and subjected to an additional static force is described by the single-particle Hamiltonian

$$H = -\frac{\hbar^2}{2M}\frac{d^2}{dx^2} + V_{\text{dis}}(x,t) + Fx, \tag{6.1}$$

where M is the mass of the condensate atoms ($M = 1.44 \times 10^{-25}$ kg for rubidium 87), and F is the Stark force. The term $V_{\text{dis}}(x,t)$ is a time-dependent stochastic potential which is created by a time-dependent bichromatic lattice

(see Eq. (2.27)) along the longitudinal direction x as

$$V_{\mathrm{dis}}(x,t) = \alpha V \left\{ \sin^2\left(\frac{\pi x}{d_{\mathrm{L}}}\right) + \sin^2\left(\frac{\pi x}{d_{\mathrm{L}}^{'}} + \phi(t)\right) \right\}, \tag{6.2}$$

which consists of two spatially periodic potentials with incommensurate lattice spacings d_{L} and $d_{\mathrm{L}}^{'}$, respectively. In our calculation, we chose $d_{\mathrm{L}} = 426\,\mathrm{nm}$ for the initially existing lattice (the "main" lattice), and $d_{\mathrm{L}}^{'} = d_{\mathrm{L}}(\sqrt{5}-1)/2$ for the secondary lattice. The time-dependence of the second lattice arises because of the time-dependent stochastic phase $\phi(t)$. The time-dependent phase $\phi(t)$ can be produced by using different noise generators introduced in section 3.2. The depths of the two lattices are considered to be comparable and for convenience equal amplitudes αV for both lattices are chosen, where V is the lattice depth of the main lattice which was already presented in section 5.1. The factor α is a renormalization factor for the lattice depth (see section 6.2 for more details).

As in the previous chapter, the recoil energy $E_{\mathrm{rec}} = \pi^2\hbar^2/(2Md_{\mathrm{L}}^2)$ is the characteristic energy scale for the system and $V_0 = V/E_{\mathrm{rec}}$ and $F_0 = Fd_{\mathrm{L}}/E_{\mathrm{rec}}$ are dimensionless quantities in this energy unit. The initial state is a relaxed condensate wave function in the harmonic trap with frequency ν_{x} (here $20\ Hz$), which is then loaded adiabatically in the lattice given by $V_{\mathrm{dis}}(x,t)$ at $t=0$. The stochastic nature of $V_{\mathrm{dis}}(x,t)$ makes it necessary to average our results over a sufficient number of noise realizations. As explained in section 3.2.4, 20 realizations of the noise is an adequate number in order to study the effects of different parameters of the stochastic potential qualitatively.

The goal in this chapter is to investigate the possibilities to control the dynamics of the Bose–Einstein condensate by manipulating the characteristic parameters of the time-dependent stochastic phase $\phi(t)$. To that respect, the temporal behavior of the survival probability of the condensate in the ground band is studied in a broad range of parameters. In section 6.3, the exponentially correlated noise, introduced in section 3.2.1, is used as the time-dependent phase $\phi(t)$. It is shown that different regimes of the system and the noise parameters lead to different tunneling rates of the condensate atoms. In section 6.4, the impact of harmonic noise on the tunneling rate is investigated. Various regimes of harmonic noise parameters are studied in this section. Finally, in section 6.5, a deterministic noise is used as the time-dependent phase $\phi(t)$. The idea of the latter is to compare the effect of the determonistic phase with the harmonic noise case. In fact, the spectral distributions of these two time-dependent phases can be made comparable as described in section 3.2.2. It is expected that in such a regime both types of noise lead to similar effects on the tunneling rate. In the following section, a static effective potential is analytically calculated. This effective potential can model the dynamics of the condensate in the presence of a time-dependent stochastic potential under certain circumstances.

6.2 Effective potential

The time-dependent phase $\phi(t)$ can be exponentially correlated noise or harmonic noise or even a deterministic one (see section 3.2). Depending on the characteristic parameter of the noise, its correlation time can be small or large compared with the time scale of the system (which is the Bloch period T_{B} in our case). Therefore, the noise can be made to be a slowly varying function or a fast oscillating one, when its correlation time is larger or smaller than T_{B}, respectively (see section 3.2).

In the regime of very fast oscillating noise $\phi(t)$, the particle feels an effective time-independent potential instead of a time-dependent noisy one. Therefore, the time-dependent potential can be replaced by a suitable static effective potential in the limit of a large oscillation frequency of the noise. Such an effective potential is calculated by integrating over all possible phases

$$\begin{aligned}\int_{-\infty}^{\infty} d\phi\ \sin^2\left(\frac{\pi x}{d_{\mathrm{L}}'}+\phi\right)\frac{\exp\left(\frac{-\phi^2}{2\sigma^2}\right)}{\sqrt{2\pi\sigma^2}} \\ = c+\exp\left(-2\sigma^2\right)\sin^2\left(\frac{\pi x}{d_{\mathrm{L}}'}\right),\end{aligned} \tag{6.3}$$

where ϕ is generated by using the Gaussian white noise (see section 3.2). Therefore, the noise ϕ has a zero mean and the variance $\sigma^2=\langle\phi\,(t)^2\rangle$ (see section 3.2). Apart from the constant c on the right hand side of Eq. (6.3), the effect of the fast noise is to renormalize the amplitude of the second lattice with a renormalization factor $\beta=\exp\left(-2\sigma^2\right)$. This renormalization factor β will be determined for each type of noise in sections 6.3 and 6.4. Replacing $V_{\mathrm{dis}}(x,t)$ in Eq. (6.1) by the static effective potential

$$V_{\mathrm{eff}}\,(x)=\alpha V\left\{\sin^2\left(\pi x/d_{\mathrm{L}}\right)+\beta\sin^2\left(\pi x/d_{\mathrm{L}}'\right)\right\}, \tag{6.4}$$

the resulting effective model describes the dynamics of the system in the presence of very fast noise.

The renormalization factor α is introduced to be able to compare the dynamics in the presence of the potential given by Eq. (6.2) to the dynamics of the "reference system" introduced in chapter 5, i.e., the system with the lattice potential given by $V\,(x)=V\sin^2\left(\pi x/d_{\mathrm{L}}\right)$. Eq. (6.4) provides the time-independent effective potential which is used to compute α. The parameter α will be chosen in such a way that the following standard deviations are equal:

$$\sigma\left(V(x)\right)=\sigma\left(V_{\mathrm{eff}}(x)\right). \tag{6.5}$$

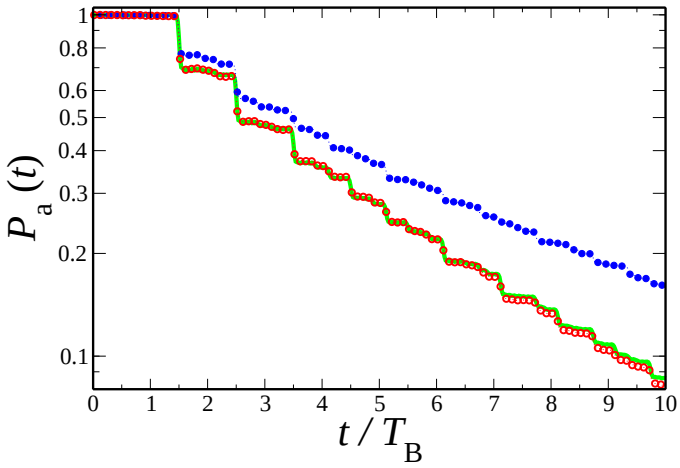

Figure 6.1: Comparison between the effective model and the stochastic system. Shown is the time evolution of the survival probability in the disorder system with $V_0 = 2.5$, $F_0 = 1.5$, and $\alpha \approx 0.85$: with the effective potential of Eq. (6.4) (green solid line), in the presence of a slowly varying noise with correlation time $\tau = 10\,T_{\rm B}$ (blue filled circles) and for a fast noise with $\tau = 0.001\,T_{\rm B}$ (red open circles).

The standard deviation σ of a variable X is defined as $\sqrt{\langle (X - \langle X \rangle)^2 \rangle}$ and the average $\langle \cdot \rangle$ is an integral over space for a sufficiently large length interval L ($\approx 20 d_{\rm L}$ in most calculations), as

$$\langle X \rangle \equiv 1/L \int_{-L/2}^{L/2} X dx. \tag{6.6}$$

Figure 6.1 exhibits a comparison between the results calculated using the effective potential given in Eq. (6.4) and the noisy system. The observable is the survival probability of the condensate to remain in the ground band. In Figure 6.1, one can see the time-evolution of the survival probability $P_{\rm a}(t)$ in the effective model (green solid line), and in the noisy system defined in Eq. (6.1) with a slowly varying phase $\phi(t)$ (blue filled circles) and for the fast oscillating phase (red open circles). The agreement between the survival probabilities shown by the green solid line and the red open circles confirms that the effective potential can predict the effect of the fast noise correctly. In the following sections, the impact of different types of noise on the survival probability of the condensate will be presented. The effective potential is defined for each case and used as a benchmark for our calculations in the regime of fast noise.

6.3 Impact of exponentially correlated noise

The correlated noise can be used as the time-dependent phase $\phi(t)$ for the second lattice. A standard example is the exponentially correlated noise, which is characterized by a single correlation time. Such a noise, as defined in section 3.2.1, has an exponential correlation function and a Lorentzian spectral distribution. Considering the characteristic parameters of the exponentially correlated noise, different regimes of the noise are introduced (see section 3.2.1). In the slowly varying regime, the noise has a large correlation time compared with the time scales of the system (i.e., $\tau \gg T_{\mathrm{B}}$). The regime of fast noise is recovered when $\tau \ll T_{\mathrm{B}}$.

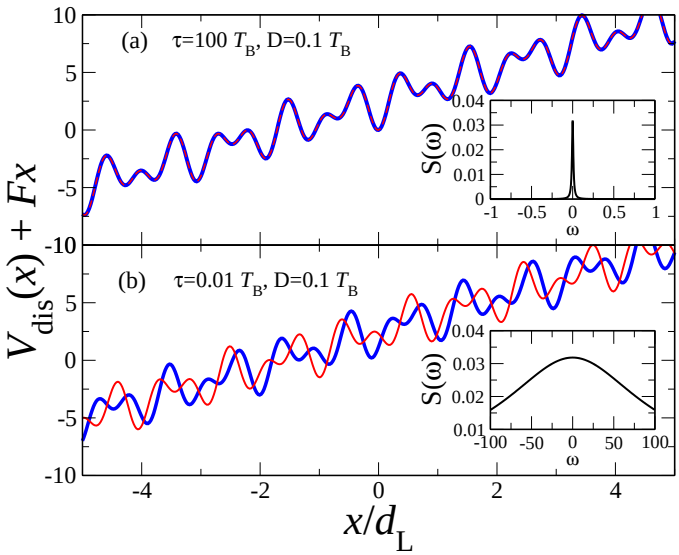

Figure 6.2: The tilted disordered potential $V_{\mathrm{dis}}(x,t)$, with $V_0 = 2.5$ and $F_0 = 1.5$, at time $t = 2T_{\mathrm{B}}$ (blue line) and $t = 6T_{\mathrm{B}}$ (red line) of the evolution. $\phi(t)$ is the exponentially correlated noise with $D = 0.1/T_{\mathrm{B}}$ and (a) $\tau \gg T_{\mathrm{B}}$, and (b) $\tau \ll T_{\mathrm{B}}$. Insets: the corresponding Lorentzian spectral distributions $S(\omega)$.

Figures 6.2(a) and (b) show the tilted disordered potential $V_{\mathrm{dis}}(x,t)$ at two different times $t = 2T_{\mathrm{B}}$ (blue line) and $t = 6T_{\mathrm{B}}$ (red line) of the evolution. In panel (a), for a large correlation time $\tau = 100\ T_{\mathrm{B}}$ of exponentially correlated noise, the spectral distribution is a delta-like function (inset of panel (a)), i.e., the phase is almost constant in time. The shape of the potential with such a constant phase is therefore unchanged in time, while the small $\tau = 0.01\ T_{\mathrm{B}}$ shown in panel (b) results in a broad peak of the spectral distribution (see the inset of panel (b)). The shape of the potential is changing in time since the

phase is changing on a time scale much smaller than the time scale T_{B} of the system.

The energy scale of the noise can be estimated by calculating the width $\Delta\tilde{\omega}$ of the spectral distribution peak. Using the definition of the inflection point for the spectral distribution function $S(\omega)$ (i.e., by solving $d^2S(\omega)/d\omega^2 = 0$) gives the width of the spectral peak: $\Delta\tilde{\omega} \equiv 1/(\sqrt{3}\tau)$. This width $\Delta\tilde{\omega}$ is vanishing for large correlation times and is very broad for small correlation times (see insets in Figure 6.2). The energy induced by the noise can be of the same order as the system's energy scale (given by the band gap ΔE) or can be much larger or smaller. In the following, it is shown how these different regimes can affect the tunneling rate of the condensate.

Two groups of system parameters are considered in the following results: V_0 and F_0 can be chosen to fulfill the condition of resonantly enhanced tunneling (RET) or they can be away from this special condition. Since at RET the transport from the ground band to higher bands is enhanced by energetic degeneracies (see section 2.4.1) and the noise is likely to drive the system out of RET conditions, the Landau–Zener tunneling rate degrades in this case. As will be confirmed by our results shown in Figure 6.4, enhancement induced by the noise is much simpler to be achieved away from RET since then there is no competition between the two effects.

6.3.1 Impact of the correlation time τ on tunneling

Here, we study how the correlation time τ of the exponentially correlated noise can affect the tunneling probability. Figure 6.3 shows the temporal evolution of the survival probability $P_{\mathrm{a}}(t)$ of the condensate in the ground band for various correlation times τ of the noise. The system parameters are $V_0 = 2.5$ (which gives the average band gap $\Delta E \approx 2.5\, E_{\mathrm{rec}}$ between the ground band and the first excited band in the periodic system) and $F_0 = 1.5$. This force leads to the non-RET condition in the reference system. As mentioned in section 6.1 the reference system is defined by Eq. (5.1). The thick black solid line shows the time evolution of the survival probability for this reference system. A nice step structure similar to the one depicted in Figure 5.5(b) is observed in the time evolution of the survival probability.

The other curves shown in Figure 6.3 exhibit the time evolution of the survival probability for the stochastic system defined in Eq. (6.1) with the potential given in Eq. (6.2). The parameter α in $V_{\mathrm{dis}}(x,t)$ is calculated using $\beta = \exp(-2\sigma^2)$ as defined in section 6.2. The phase $\phi(t)$ in $V_{\mathrm{dis}}(x,t)$ is the exponentially correlated noise. The variance of this noise is $\langle\phi(t)\rangle \equiv D/\tau$ (see section 3.2.1). For $D/\tau = 0.25$, which is the value used in Figure 6.3, $\alpha \approx 0.85$ is calculated. The parameters α and D/τ are fixed for all data shown in Fig-

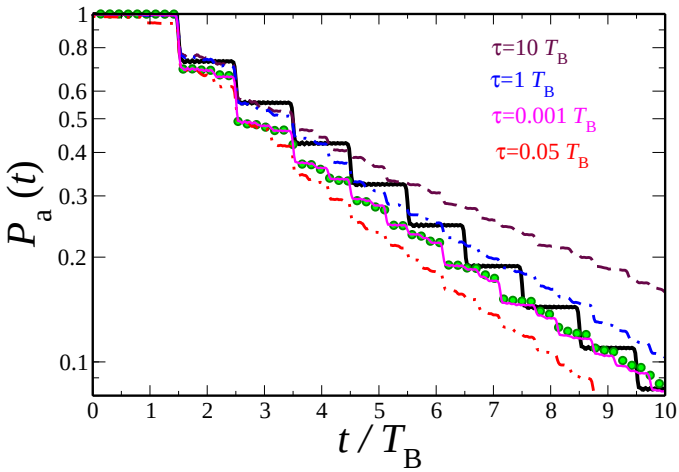

Figure 6.3: Time evolution of the survival probability $P_{\rm a}(t)$ for various τ and fixed $V_0 = 2.5$, $F_0 = 1.5$, and $\alpha \approx 0.85$. The time evolution of the survival probability of the reference system defined by Eq. (5.1) is shown by the thick solid line. For the stochastic system with the exponentially correlated noise with $D/\tau = 0.25$ and correlation times: $\tau = 10\ T_{\rm B}$ (dashed line), $\tau = 1\ T_{\rm B}$ (dot-dashed line), $\tau = 0.05\ T_{\rm B}$ (dot-dot-dashed line), $\tau = 0.001\ T_{\rm B}$ (thin solid line); the result with the effective model of Eq. (6.4) is shown by green filled circles.

ure 6.3. For the temporally disordered system defined in Eq. (6.1), no periodic band structures can be found in the energy spectrum. Therefore, the particle can no longer perform Bloch oscillations (see section 2.3) and hence no step structure is expected to be seen in the time evolution of the survival probability. As seen in Figure 6.3, in the presence of the disordered potential the step structure of the survival probability is washed out.

Large correlation time: In the regime of $\tau \gg T_{\rm B}$, the noise is a slowly varying function (or even constant) in time compared with the time scale of the system. Therefore, the potential is similar to the static bichromatic lattice defined in section 2.2.3, in which the transport of particles is suppressed. The result for a large correlation time $\tau = 10\ T_{\rm B}$ (shown by the dashed line in Figure 6.3) demonstrates that the tunneling probability is suppressed compared with the reference system (thick black solid line). By decreasing the correlation time τ, the rate of tunneling increases but, nevertheless, for $\tau \geq T_{\rm B}$ the noise suppresses the tunneling compared with the reference system (see the data for $\tau = 1\ T_{\rm B}$ shown by the dot-dashed line in Figure 6.3). In this regime of $\tau > T_{\rm B}$, the width $\Delta\tilde{\omega}$ ($\equiv 1/(\sqrt{3}\tau)$) of the peak in the Lorentzian spectral distribution of the noise is very small. Therefore, the energy induced by the noise is much smaller than

ΔE and cannot energetically assist the tunneling.

Small correlation time: For correlation times smaller than T_B (e.g., for $\tau = 0.05\ T_{\mathrm{B}}$), the noise is a fast oscillating stochastic function and the results (dot-dot-dashed line) show the enhancement of the tunneling rate compared with the reference system (thick solid solid line). For this correlation time, the peak in the spectral distribution has a width $\Delta\tilde{\omega} \equiv 1/(\sqrt{3}\tau) \approx 2.75\ E_{\mathrm{rec}}$, which matches the band gap $\Delta E \approx 2.5$ of the system. This coincident is the reason for enhancement of the tunneling probability. A further decrease of the correlation time (e.g., for $\tau = 0.001\ T_{\mathrm{B}}$ depicted by the thin solid line) decreases the tunneling rate of atoms. In the limit of $\tau \ll T_{\mathrm{B}}$, the time-dependent potential can be replaced by the static effective potential given in Eq. (6.4). For the exponentially correlated noise the renormalization factor is given by $\beta = \exp(-2D/\tau)$ in the effective potential. The effective potential defined in Eq. (6.4) describes the dynamics of the tunneling process in the presence of the exponentially correlated noise with $\tau \ll T_{\mathrm{B}}$. As seen in Figure 6.3, the survival probability for a very small $\tau = 0.001\ T_{\mathrm{B}}$ (thin solid line) shows a perfect agreement with the result (filled circles) calculated using the effective model. This agreement confirms that the effective potential can predict the effect of the noise in the regime of small correlation times. In the following, more investigations are done to distinguish the interesting range of parameters for which the tunneling rate is enhanced or suppressed.

Scan over the noise parameter τ

To understand the impact of the noise parameters on the tunneling rate, the decay rate Γ_{a} of the survival probability is calculated for a scan over the correlation time of the noise τ, while $D/\tau = 0.25$ is fixed. The decay rate is calculated by fitting a global exponential curve to the survival probability data. Such decay rates Γ_{a} are shown in Figure 6.4 for the lattice depth $V_0 = 2.5$ (which gives the band gap $\Delta E \approx 2.5 E_{\mathrm{rec}}$) and three different Stark forces $F_0 = 0.95$ (green triangles), 1.25 (blue squares) and 1.5 (red circles). The chosen forces are specified by vertical lines later on in Figure 6.6. Comparing the symbols to colored dashed lines (which specify the decay rate in the corresponding reference system), one realizes that the decay rate is enhanced when the system parameters do *not* fulfill the RET condition, i.e., in Figure 6.4: $F_0 = 0.95$ and $F_0 = 1.5$ (symbols lie above the corresponding dashed lines). For the case of $F_0 = 1.25$ (RET), the tunneling rate in the noisy system is suppressed, and the symbols lie always below the reference line (blue dashed line). The enhancement is pronounced in the range of $\tau \approx 0.005...0.1\ T_{\mathrm{B}}$ corresponding to an energy scale $\Delta\tilde{\omega} \geq 1\ E_{\mathrm{rec}}$ which is of the same order as the energy scale of the system E_{rec} and the band

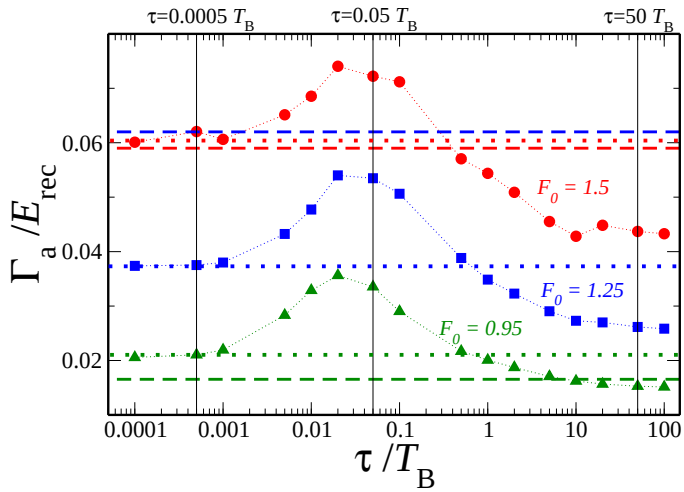

Figure 6.4: Decay rate Γ_a of the survival probability versus τ and fixed $D/\tau = 0.25$, for $V_0 = 2.5$, and $F_0 = 1.5$ (red filled circles); $F_0 = 1.25$ (blue filled squares); $F_0 = 0.95$ (green filled triangles). Results from calculations with the effective model given by Eq. (6.4) (colored dotted lines) and with the reference system given by Eq. (5.1) (colored dashed lines). Vertical lines specify the three τ which are used in Figure 6.6

gap ΔE. For a very small correlation time, the effective model can describe the dynamics of the condensate very well (see the agreement between symbols and colored dotted lines for $\tau < 0.005\ T_B$ in Figure 6.4). This agreement confirms the use of our effective model as a benchmark for the cases in the presence of fast noise (small correlation time). For large values of $\tau > T_B$, the system is in the slowly varying regime of the noise with a narrow peak in its spectral distribution. This peak leads to an energy scale much smaller than the energy scale ΔE of the system (e.g., for $F_0 = 1.5$, and $\tau = 1\,T_B$, $\Delta\tilde{\omega} \approx 0.1\,E_{rec} \ll \Delta E$) and hence does not help to enhance the tunneling of atoms.

Instead of plotting decay rates, we may show the survival probabilities at a specific time t_0 (a few Bloch periods), sufficiently away from zero time of the evolution to avoid initial fluctuations and not during a Landau–Zener step. Figure 6.5 shows the survival probabilities $P_a(t_0)$ at (a) $t_0 = 6\ T_B$ and (b) $t_0 = 10\ T_B$ for the same system with $V_0 = 2.5$ and the same conditions as presented in Figure 6.4, with the only difference that instead of decay rate Γ_a, the survival probability $P_a(t_0)$ is now considered as the observable. As seen the time of realization t_0 does not have any effect on the respond of observable $P_a(t_0)$. The enhancement of tunneling is distinguished by the valley in Figure 6.5 equivalent to the peak appears in decay rates in Figure 6.4. Both figures 6.5 and 6.4 show the same effects and lead to same understandings of the system in

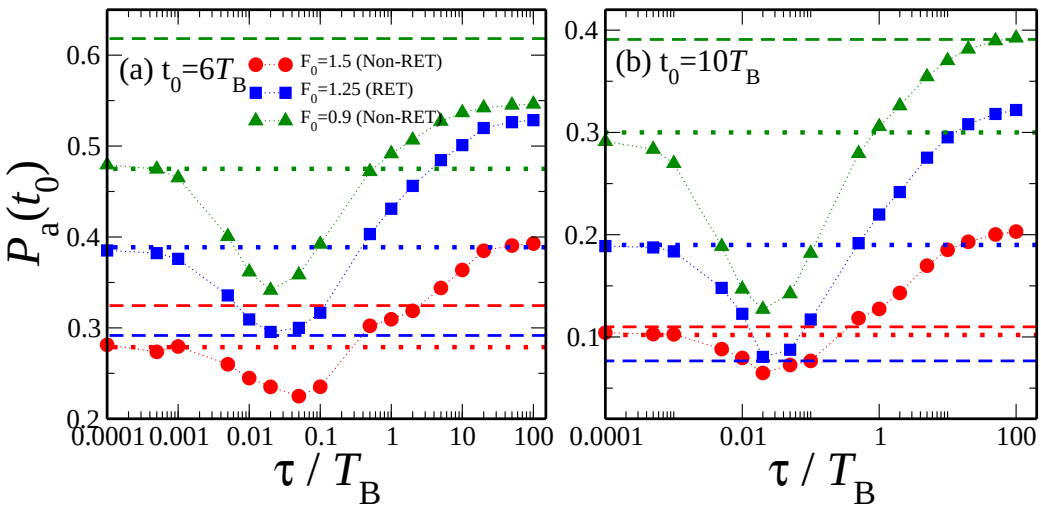

Figure 6.5: The survival probability at time t_0: (a) $t_0 = 6\ T_\mathrm{B}$ and (b) $t_0 = 10\ T_\mathrm{B}$; for $V_0 = 2.5$, $\Delta E \approx 2.5\, E_\mathrm{rec}$ and $D/\tau = 0.25$: scan over τ for $F_0 = 1.5$ (red filled circles) and with the effective potential (orange dot-dashed line); $F_0 = 1.25$ (blue filled squares) and with the effective potential (light blue dot-dashed line); $F_0 = 0.95$ (green filled triangles) and with the effective potential (light green dotted line). The results for corresponding reference systems are shown by colored dashed lines.

the presence of noise.

6.3.2 Impact of the Stark force on tunneling

Keeping the noise parameters constant, we study the decay rate Γ_a of the survival probability of the condensate for various Stark forces F_0. Such decay rates for a scan over the Stark force F_0 are shown in Figure 6.6. The thick solid line depicts the decay rate for the reference system defined in Eq. (5.1). The Landau–Zener exponential prediction for the decay rate (i.e., Eq. (2.37) and section 3.1) is shown by the black dashed line. Comparing the dashed line with the solid line, the RET peaks can be clearly distinguished. The symbols show the decay rate in the system with potential $V_\mathrm{dis}(x,t)$ defined in Eq. (6.2). The results are for three values of correlation time $\tau = 0.0005\ T_\mathrm{B}$ (blue squares), $0.05\ T_\mathrm{B}$ (red circles), and $50\ T_\mathrm{B}$ (green triangles), and $D/\tau = 0.25$ is constant for all the data. These three correlation times are chosen from the left shoulder, the peak point and the right shoulder of the curves shown in Figure 6.4 (shown by vertical solid lines). As seen, the RET peaks in the decay rate (present in the thick solid line of Figure 6.6) are washed out (the data shown by symbols). Since the potential $V_\mathrm{dis}(x,t)$ is no longer periodic, and hence there is no band structure,

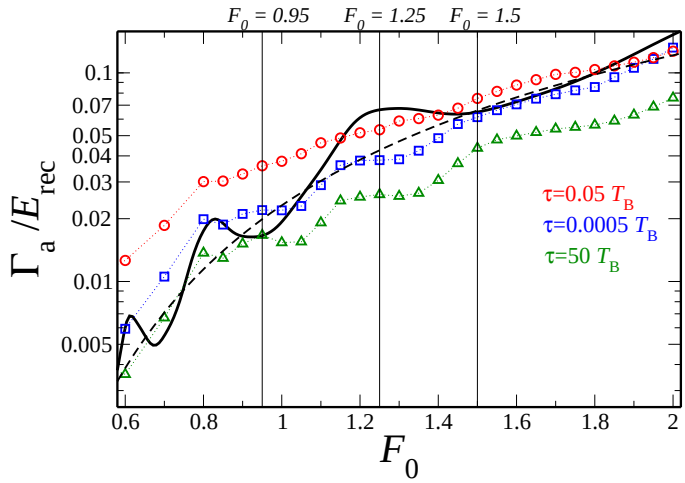

Figure 6.6: The decay rate of the survival probability for $V_0 = 2.5$, and $D/\tau = 0.25$: scan over F_0 for $\tau = 0.0005\ T_{\mathrm{B}}$ (blue open squares), $\tau = 0.05\ T_{\mathrm{B}}$ (red open circles), $\tau = 50\ T_{\mathrm{B}}$ (green open triangles), and for the reference system (solid line); the Landau-Zener exponential prediction for the reference system (dashed line).

and RET looses its meaning and the resonance peaks are washed out for the decay rate in the noisy systems. Dependent on the correlation time of the noise, a suppression or an overall enhancement of the decay rate can be observed in Figure 6.6. For very large and very small values of τ, the decay rate is suppressed compared with the reference system (black solid line), and for $\tau = 0.05\ T_{\mathrm{B}}$ the decay rate is enhanced. For this latter case, the spectral distribution is neither a delta peak, nor a very broad Lorentzian distribution, and the energy scales of the noise and the system are comparable (as discussed also in section 6.3.1). Therefore, the noise assists the tunneling. The noise with a very large τ, has a very small energy scale which typically does not match the system's intrinsic energy scale. As a consequence, it is most likely to perturb the Landau-Zener tunneling process, leading to a suppression of the transport of condensate atoms between the bands.

6.3.3 Impact of the noise parameter D

To distinguish between the effect of τ and D on the tunneling probability of the condensate, here, the noise parameter D is held constant while performing a scan over the other noise parameter τ. By keeping D fixed, the strength of the exponentially correlated noise is constant. Therefore, any effect which is seen results from the correlation time τ of the noise.

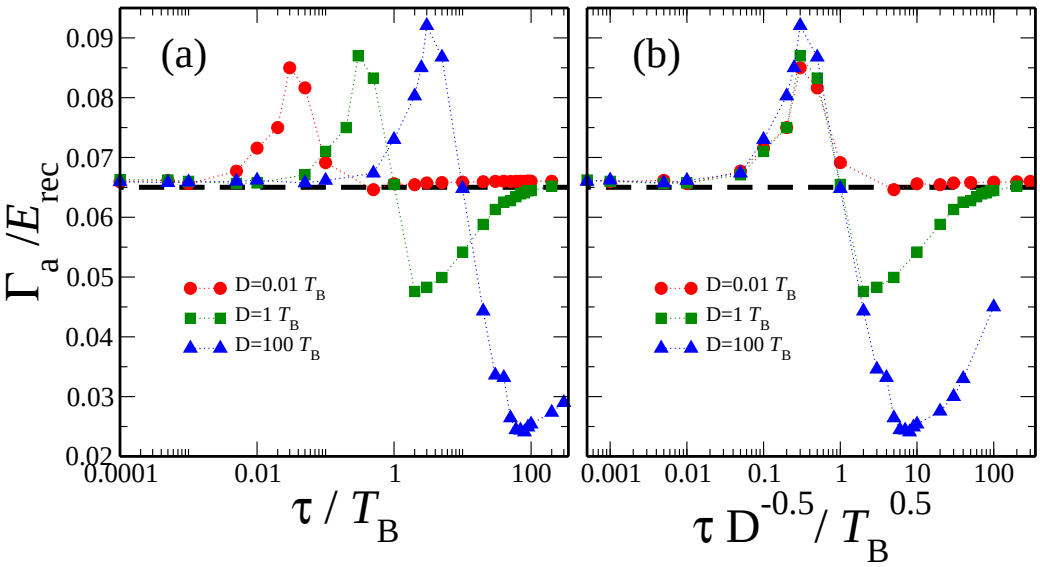

Figure 6.7: Decay rate of the survival probability for the system with $V_0 = 2.5$, $F_0 = 1.5$, and a scan over τ, for $D = 0.01\,T_{\rm B}$ (red filled circles); $D = 1\,T_{\rm B}$ (green filled squares); $D = 100\,T_{\rm B}$ (blue filled triangles). (a) $\Gamma_{\rm a}$ against τ and (b) $\Gamma_{\rm a}$ against versus $\tau/\sqrt{D}$ the rescaled parameter. The result for corresponding reference systems is shown by the black dashed line.

The decay rates of the survival probability in the system with lattice depth $V_0 = 2.5$ and the Stark force $F_0 = 1.5$ (non-RET), for different D and a scan over τ are shown in Figure 6.7. As seen in panel (a), then if D is small (e.g., $D = 0.01\,T_{\rm B}$ shown by red filled circles) the decay rate remains around the decay rate of the reference system (black dashed line) for most of τ value. Only in a range of $0.005\,T_{\rm B} \lesssim \tau \lesssim 0.1\,T_{\rm B}$, the decay rate deviates from the one of the reference system and shows a peak at $\tau \approx 0.05\,T_{\rm B}$. For larger values of D, the peak in decay rates shifts to the right. This peak confirms that for a specific range of τ the noise assists the tunneling. By increasing τ further, the decay rate for $D = 0.01\,T_{\rm B}$ remains again close to the reference system, i.e., the noise does not affect the tunneling rate. For such a small D the amplitude of noise fluctuations is very small, therefore it has less effect on the tunneling. For $D \geq 1\,T_{\rm B}$, a transition happens and the decay rate decreases suddenly and a valley appears as seen in Figure 6.7(a), i.e., for the slowly varying noise with $\tau > T_{\rm B}$, the strong noise suppresses the decay rate. The larger the parameters D is, the deeper the valley in the decay rate. Going further to the right ($\tau > T_{\rm B}$), the fluctuation amplitude $\langle \phi(t)^2 \rangle \equiv D/\tau$ of the noise is decreasing. Since for $D/\tau < 1$ the noise is very weak, the decay rate starts to increase again and approaches the vicinity of the dashed line. The shift in the position of peaks and

valleys seems systematic and depending on D. Therefore, a rescaling of the data should lead to a universal behavior.

Figure 6.7(b) shows the rescaled data of the decay rate versus $\tau/\sqrt{D}$. This value corresponds to the strength of the Gaussian white noise ξ used to generate the noise (According to the definition of the exponentially correlated noise given in section 3.2.1 the phase is given by $\dot{\phi}(t) = \phi/\tau + \frac{\sqrt{2D}}{\tau}\xi(t)$). As seen in Figure 6.7(b), the structure of the decay rates is now the same for all the cases. A universal peak appears at a specific value of $\tau/\sqrt{D}$ where the decay rate is enhanced and then later a transition happens to the regime in which the tunneling is suppressed. For $0.1\,T_{\mathrm{B}}^{-1/2} < \tau/\sqrt{D} < 1\,T_{\mathrm{B}}^{-1/2}$, the decay rate of the survival probability is enhanced with a peak at around $\tau/\sqrt{D} \approx 0.3\,T_{\mathrm{B}}^{-1/2}$. Then at $\tau/\sqrt{D} \approx 1\,T_{\mathrm{B}}^{-1/2}$ a transition to the regime of slowly varying noise happens and the decay rates are suppressed. It is interesting that in all the cases the peak of enhancement happen at this specific value. More investigations are needed to discover the underlying reason of such a behavior.

The usefulness of scaling is the reduction of the parameter dependence of the system. We simplify the investigations by reducing the effective parameters to one (e.g., here $\tau/\sqrt{D}$). In the next section, a more interesting and yet more complicated noise is presented. We show how the rescaling can be helpful to reduce the number of involved parameters of the noise on the tunneling and to understand the effect of the noise on the tunneling probability.

6.4 Impact of harmonic noise

In this section, we present our results for the harmonic noise introduced in section 3.2.2. Using the harmonic noise as the phase in the secondary lattice, the tilted time-dependent disorder potential $V_{\rm dis}\,(x,t)$ is shown at two different times $t = 2\,T_{\rm B}$ and $t = 6\,T_{\rm B}$ for different regimes of noise parameters in Figures 6.8. The corresponding spectral distributions $S(\omega)$ are plotted in the insets. The damping frequency of the harmonic noise is $\Gamma = 5/T_{\rm B}$, for all the four cases. For the noise strength $T = 0.01/T_{\rm B}^2$ and a small oscillation frequency $\omega_0 = 0.05/T_{\rm B}$ compared with both the damping frequency Γ and the frequency scale of the system given by $1/T_{\rm B}$, the shape of the potential is unchanged in time. As seen in the inset of panel (a), the spectral distribution $S(\omega)$ is Lorentzian in this regime with a very narrow peak at zero frequency. Therefore, the phase is almost constant during the time evolution and the potential is essentially a static bichromatic lattice. Keeping ω_0 fixed, $V_{\rm dis}\,(x,t)$ is shown in Figure 6.8(b) at two different times for the noise strength $T = 10/T_{\rm B}^2$. The lattice shape is changing in time for this noise, though ω_0 and Γ are the same as in the previous case. The inset shows the corresponding spectral distribution $S(\omega)$ which is Lorentzian-like similar to the one shown in Figure 6.8(a) however, the height of the peak is 1000 times larger in Figure 6.8(b). In Figure 6.8(c), $\omega_0 = 10/T_{\rm B}$, i.e., the oscillation frequency is larger than the damping frequency, and the noise performs fast oscillations. As seen in the inset, the power spectrum peaks at a finite frequency $\tilde{\omega} = \sqrt{\omega_0^2 - 2\Gamma^2}$ with a finite width $\Delta\tilde{\omega} \approx 2\sqrt{\Gamma\sqrt{\omega_0^2 - \Gamma^2}}$, defined in section 3.2.2. But since the strength T of the noise is small, this noise does not change the potential in time. Increasing T gives rise to a time-dependent change of the lattice structure, as seen in Figure 6.8(d). A Large T leads to a larger peak (in height) but does not change the width of the spectral distribution peak, as seen in insets of Figure 6.8. As long as $T < 1/T_{\rm B}^2$, the noise does not have a significant effect on the shape of the potential. At large T however, as seen in Figure 6.8(b) and (d), the noise affects the shape of the potential temporally. It is expected that this change in the shape and the energy induced by the noise assists the tunneling of the condensate out of the ground band. This energy results from the finite width $\Delta\tilde{\omega}$ of the peak at $\tilde{\omega}$ in the spectral distribution of the noise, and can be compared with the energy scale of the system given by $E_{\rm rec}$ and the band gap ΔE.

6.4.1 Harmonic noise in the exponentially correlated limit

In section 3.2.2, we explained that the harmonic noise in the regime of very large Γ compared with ω_0 can recover the exponentially correlated noise as seen also

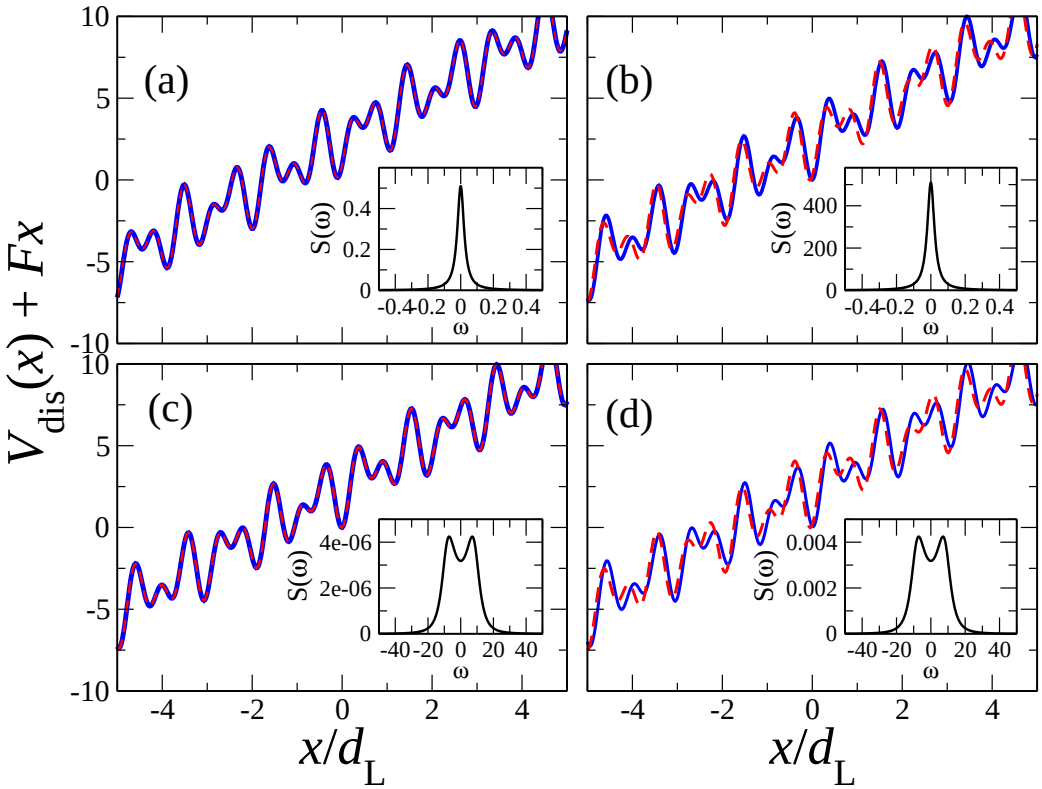

Figure 6.8: The tilted disordered potential $V_{\rm dis}(x,t)$ with $V_0 = 2.5$ and $\alpha = 1$, at $t = 2\,T_{\rm B}$ (blue line) and $t = 6\,T_{\rm B}$ (red dashed line). The phase $\phi(t)$ is given by the harmonic noise with damping frequency $\Gamma = 5/T_{\rm B}$ and (a) $\omega_0 = 0.5/T_{\rm B}$ ($\tau_{\rm HN} > 0$) and $T = 0.01/T_{\rm B}^2$; (b) $\omega_0 = 0.5/T_{\rm B}$ ($\tau_{\rm HN} > 0$) and $T = 10/T_{\rm B}^2$; (c) $\omega_0 = 10/T_{\rm B}$ ($\tau_{\rm HN} < 0$) and $T = 0.01/T_{\rm B}^2$; (d) $\omega_0 = 10/T_{\rm B}$ ($\tau_{\rm HN} < 0$) and $T = 10/T_{\rm B}^2$. The corresponding spectral distributions $S(\omega)$ are shown in the insets.

in the insets of Figure 6.8(a) and (b). The spectral distribution is Lorentzian for both types of noise, and one can calculate τ and D for the corresponding exponentially correlated noise:

$$\begin{aligned} S_{\rm HN}(0) = S_{\rm ECN}(0) \quad &\Rightarrow\ D = \frac{2\Gamma T}{\omega_0^4}, \\ \left\langle \phi(t)^2 \right\rangle_{\rm HN} = \left\langle \phi(t)^2 \right\rangle_{\rm ECN} &\Rightarrow\ \tau = \frac{D\omega_0^2}{T}, \end{aligned} \tag{6.7}$$

where for the harmonic noise $\langle \phi(t)^2 \rangle = T/\omega_0^2$ (see section 3.2.2) and for the exponentially correlated noise $\langle \phi(t)^2 \rangle = D/\tau$ (see section 3.2.1). In this regime, the effect of the harmonic noise and the exponentially correlated noise on the tunneling probability of the condensate should be comparable.

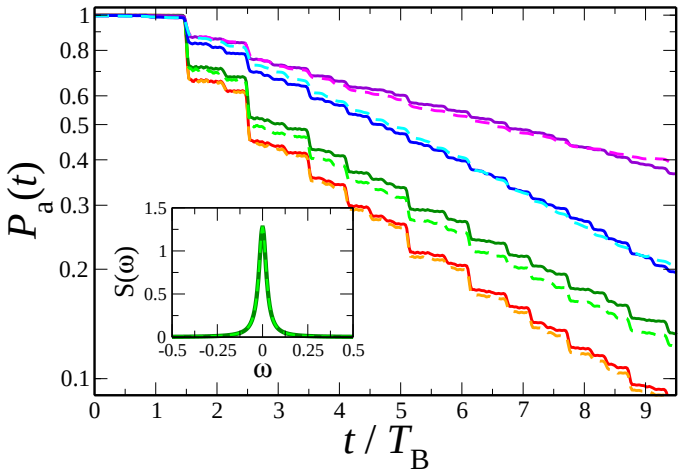

Figure 6.9: A comparison between the time evolution of the survival probability for $V_0 = 2.5$ and $F_0 = 1.5$ in the presence of harmonic noise in the slowly varying regime with $\Gamma = 5/T_\mathrm{B}$ and $\omega_0 = 0.5/T_\mathrm{B}$ (dashed lines) and exponentially correlated noise with $\tau = 40\ T_\mathrm{B}$ (solid lines): for $\langle\phi(t)^2\rangle = 0.01$ (orange dashed and red solid lines), $\langle\phi(t)^2\rangle = 0.1$ (light green dashed and dark green solid lines), $\langle\phi(t)^2\rangle = 1$ (magenta dashed and violet solid lines), and $\langle\phi(t)^2\rangle = 10$ (cyan dashed and blue solid lines). Inset: Spectral distribution $S(\omega)$ for the harmonic noise (light green dashed line), and the exponentially correlated noise (green solid line), for $\langle\phi(t)^2\rangle = 0.1$.

Figure 6.9 shows a comparison between $P_\mathrm{a}(t)$ calculated in the presence of harmonic noise in the slowly varying regime and exponentially correlated noise. The harmonic noise is in the slowly varying regime, (i.e., $2\Gamma^2 > \omega_0^2$) with $\Gamma = 5/T_\mathrm{B}$ and $\omega_0 = 0.5/T_\mathrm{B}$ (dashed lines), and the equivalent exponentially correlated noise has the correlation time $\tau = 40\,T_\mathrm{B}$ (solid lines). Both should have the same $\langle\phi(t)^2\rangle$ in order to be comparable. Four different $\langle\phi(t)^2\rangle = 0.01, 0.1, 1$ and 10 are considered. As seen in the main panel of Figure 6.9, the survival probabilities in the presence of the harmonic noise in the slowly varying regime and the corresponding exponentially correlated noise agree with each other very well and show the same overall decay rate. The inset of Figure 6.9 shows the spectral distribution of harmonic noise (light green dashed line) and of exponentially correlated noise (green solid line), when $\langle\phi(t)^2\rangle = 0.1$. As expected, both spectral distributions are Lorentzian-like and lie on top of each other.

6.4.2 Impact of the oscillation frequency ω_0

Here, the impact of the oscillation frequency ω_0 of the harmonic noise on the tunneling probability is studied. Figure 6.10 shows the time evolution of the

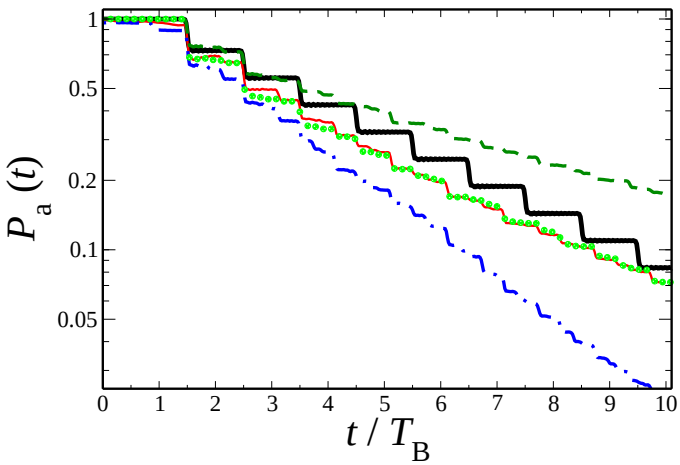

Figure 6.10: Time evolution of the survival probability for $V_0 = 2.5$ (giving $\Delta E \approx 2.5\, E_{\rm rec}$) and $F_0 = 1.5$ and $\alpha \approx 0.85$; in the presence of the harmonic noise with $\Gamma = 1/T_{\rm B}$, $\langle \phi(t)^2 \rangle = 0.25$ and various amounts of the oscillation frequency: $\omega_0 = 0.01/T_{\rm B}$ (green dashed lines); $\omega_0 = 30/T_{\rm B}$ (blue dot-dashed lines); $\omega_0 = 100/T_{\rm B}$ (red thin solid lines). Results for the effective potential are shown by green filled circles. The survival probability in the reference system is shown by the black thick solid line.

survival probability $P_{\rm a}(t)$ for different ω_0, while $\Gamma = 1/T_{\rm B}$ and $\langle \phi(t)^2 \rangle = 0.25$ are fixed. The system is set away from RET condition by choosing $V_0 = 2.5$ and $F_0 = 1.5$. This lattice depth gives rise to an average band gap $\Delta E \approx 2.5\, E_{\rm rec}$ between the ground and the first excited band of the reference system. The Hamiltonian given in Eq. (5.1) defines the reference system. $P_{\rm a}(t)$ of the reference system is shown by the black solid line in Figure 6.10 with its characteristic step-like structure. The harmonic noise tends to wash out these step structure systematically. Moreover, it leads to a strong enhancement of the tunneling rate for $\omega_0 = 30/T_{\rm B}$ (blue dot-dashed line). In this case, the spectral distribution $S(\omega)$ of the harmonic noise peaks around $\tilde{\omega} \approx 30/T_{\rm B}$ with $\Delta\tilde{\omega} \approx 10/T_{\rm B}$. In recoil energy unit, these values correspond to $7.2\, E_{\rm rec}$ and $2.6\, E_{\rm rec}$, respectively. Therefore, the noise leads to a preferred condition for the tunneling, matching the band gap ΔE even for non-RET forces. For a very small $\omega_0 = 0.01/T_{\rm B}$ (green dashed line) the harmonic noise is in the slowly varying regime with the Lorentzian-like spectral distribution which has a very narrow peak at $\omega = 0$. The width of this peak is $\Delta\tilde{\omega} \approx 5 \times 10^{-5}/T_{\rm B} \cong 10^{-5}\, E_{\rm rec}$, which is much smaller than the energy scales of the system given by $E_{\rm rec}$ and the band gap ΔE. Therefore, the noise cannot assists the tunneling in this regime.

The red line in Figure 6.10 shows the survival probability for a large $\omega_0 = 100/T_{\rm B}$. Although the oscillation frequency of the harmonic noise is much larger

than the damping frequency, the noise does not enhance the tunneling strongly.

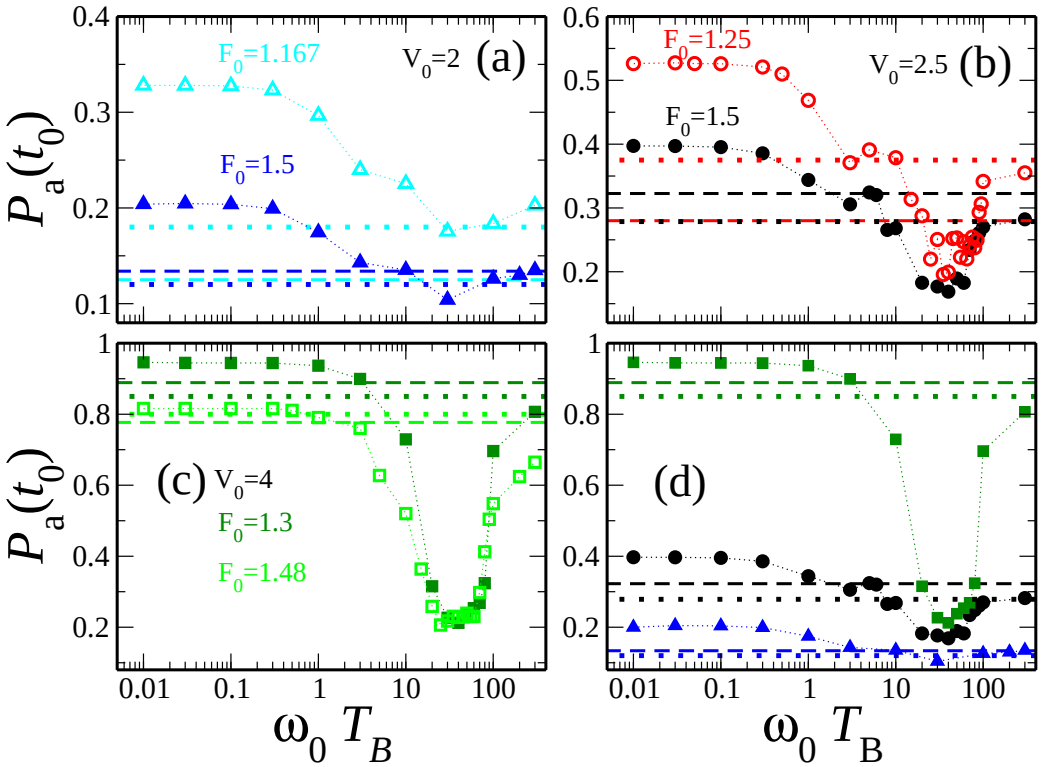

Figure 6.11: The survival probability $P_{\mathrm{a}}(t_0)$ at $t_0 \approx 6\ T_{\mathrm{B}}$ in the presence of harmonic noise with $\Gamma = 1/T_{\mathrm{B}}$, $\langle\phi(t)^2\rangle = 0.25$ and a scan over ω_0. (a) RET: $V_0 = 2$ and $F_0 = 1.167$ (cyan open triangles), non-RET: $V_0 = 2$ and $F_0 = 1.5$ (blue filled triangles); (b) RET: $V_0 = 2.5$ and $F_0 = 1.25$ (red open circles), non-RET: $V_0 = 2.5$ and $F_0 = 1.5$ (black filled circles); (c) RET: $V_0 = 4$ and $F_0 = 1.48$ (light green open squares); non-RET: $V_0 = 4$ and $F_0 = 1.3$ (dark green filled circles); (d) three non-RET cases of (a), (b) and (c) in one panel. Results with the effective potential are shown by colored dotted lines. The survival probabilities of reference systems are shown by colored dashed lines.

The spectral distribution of the noise with $\omega_0 = 100/T_{\mathrm{B}}$ peaks at $\tilde{\omega} \approx 100/T_{\mathrm{B}}$ with $\Delta\tilde{\omega} \approx 20/T_{\mathrm{B}}$, i.e., the energy induced by the noise is very large and does not match the energy scale of the system. To understand the effect of the time-dependent stochastic potential on the system in this regime of very fast oscillating noise ($\omega_0 \gg 1/T_{\mathrm{B}}$), the time-dependent potential can be replaced by a static effective potential. This effective potential $V_{\mathrm{eff}}(x)$ is given in Eq. (6.4) with $\beta = \exp(-2T/\omega_0^2)$ since $\langle\phi(t)^2\rangle = T/\omega_0^2$ for the harmonic noise (see section 3.2.2). Using the equality given in Eq. (6.5) for the parameters above,

one gets $\alpha \approx 0.85$. The time evolution of the survival probability in this effective model is shown by green filled circles in Figure 6.10, which demonstrates a perfect agreement with the result of $\omega = 100/T_{\mathrm{B}}$ (thin red line).

Figure 6.11 exhibits the survival probability $P_{\mathrm{a}}(t_0)$ after about 6 Bloch periods for a complete scan over ω_0, while keeping the damping frequency $\Gamma = 1/T_{\mathrm{B}}$ fixed. To investigate the response of the tunneling process to different system parameters, various V_0 and F_0 are chosen: (a) $V_0 = 2$ (triangle symbols), (b) $V_0 = 2.5$ (circle symbols), and (c) $V_0 = 4$ (square symbols). For each of these values of V_0, calculations were done for two Stark forces: one which fulfill RET condition (open symbols), and one which results in non-RET condition(filled symbold). Figure 6.11(d) shows $P_{\mathrm{a}}(t_0)$ for the three values of V_0 when the system is away from RET condition.

As seen for all the cases in Figure 6.11, $P_{\mathrm{a}}(t_0)$ has a valley in the range of $1/T_{\mathrm{B}} < \omega < 100/T_{\mathrm{B}}$. Therefore, for such oscillation frequencies, the noise increases the tunneling rate. Furthermore, it can be seen that the results of $P_{\mathrm{a}}(t_0)$ are below the one of the reference system (dashed lines) when the system is away from the RET condition. In fact, the energy induced by the noise drives the system out of the resonance condition, and therefore the rate of tunneling decreases.

Large oscillation frequency: The noise starts to affect the tunneling probability when it is in the fast oscillating regime and its spectral distribution peaks at a finite frequency $\tilde{\omega}_0$. Since the variance of the noise $\langle \phi(t)^2 \rangle \equiv T/\omega_0^2$ is constant for all the calculations, the parameter T is increasing by increasing ω_0, and so is the height of the peak in the spectral distribution. At large ω_0, where the noise is very fast, the system can be described by the effective model with $\beta \approx 0.6$ (leads to $\alpha \approx 0.85$) and the results are shown by the colored dotted lines in Figure 6.11. As seen, the symbols lie around the dotted lines at large ω_0, which confirms that the effective model predicts the effect of the noise very well when $100 \leq \omega_0$.

Small oscillation frequency: For small ω_0, as shown and confirmed in Figure 6.9, the harmonic noise recovers the exponentially correlated regime. As seen in Figure 6.11, for $\omega_0 < 1/T_{\mathrm{B}}$ the symbols lie above the reference dashed lines (suppression of tunneling). In this regime of ω_0, the phase $\phi(t)$ is essentially constant, and the potential resembles the bichromatic lattice with a constant random phase. As mentioned in section 3.2, each data point is achieved by averaging over 20 realizations of the noise. This means that even though the phases are random, the possible fluctuations are averaged out. Therefore, $P_{\mathrm{a}}(t_0)$ remains almost constant in the regime of slowly varying noise.

6.4.3 Impact of the damping frequency Γ of harmonic noise

The same calculation as in the previous section can be done for different values of Γ. Figure 6.12 shows $P_{\rm a}(t_0)$ at $t_0 \approx 6\ T_{\rm B}$ for $V_0 = 2.5$ and $F_0 = 1.5$ (non-RET). The phase $\phi(t)$ is given by the harmonic noise with $\langle \phi(t)^2 \rangle = 0.25$. The calculations were done scanning ω_0, for $\Gamma = 0.01/T_{\rm B},\ 1/T_{\rm B}$, and $10/T_{\rm B}$ (shown by different symbols in Figure 6.12).

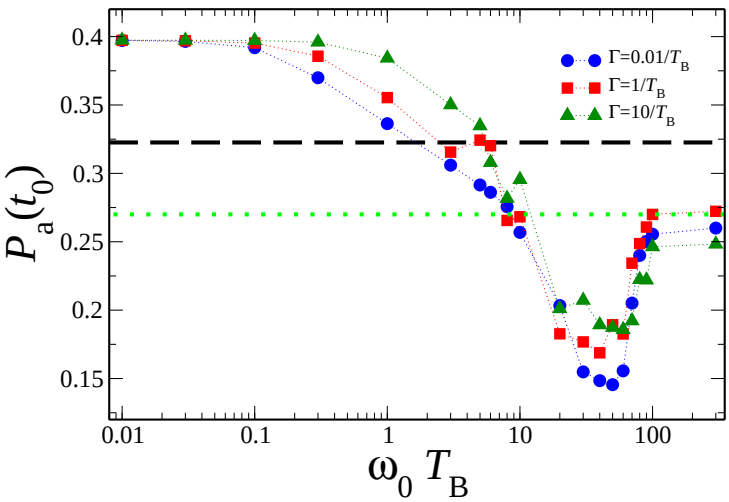

Figure 6.12: The survival probability $P_{\rm a}(t_0)$ at $t_0 \approx 6\ T_{\rm B}$ versus ω_0 for $V_0 = 2.5$ and $F_0 = 1.5$ (non-RET): $\Gamma = 0.01/T_{\rm B}$ (blue circles), $\Gamma = 1/T_{\rm B}$ (red squares), and $\Gamma = 10/T_{\rm B}$ (green triangles). The result from the effective model is shown by the green dotted line. The survival probability of the corresponding reference system is shown by the black dashed line.

As seen, the effect of the noise on $P_{\rm a}(t_0)$ is similar for different Γ. Nevertheless, one can see for larger Γ that the decay of $P_{\rm a}(t_0)$ starts later at larger ω_0. In fact, when Γ is larger, the noise remains in the slowly varying regime (with the Lorentzian-like spectral distribution) for larger ω_0 until the condition $\omega_0^2 > 2\Gamma^2$ is fulfilled (see section 3.2.2). For all the shown data in Figure 6.12, the noise enhances the tunneling probability in comparison with the reference system (black dashed line) in the range of $10/T_{\rm B} \lesssim \omega_0 \lesssim 100/T_{\rm B}$, but the valley is less deep for a larger Γ. At large ω_0, the symbols approach the vicinity of the dotted line which shows the result calculated with effective model.

6.4.4 A scan over the noise parameters Γ and ω_0

Figures 6.13 and 6.14 exhibit a scan over the noise parameters Γ and ω_0 for the same value of $\langle\phi(t)^2\rangle = 0.25$. Figure 6.13 exhibits $P_{\rm a}(t_0)$ after about six Bloch periods in the system with $V_0 = 2.5$ and $F_0 = 1.5$, and Figure 6.14 shows the observable in the system with $V_0 = 4$ and $F_0 = 1.3$. In both cases, the system is set away from the RET condition. There is a clear minimum plateau around the values used in Figure 6.11, i.e., $20/T_{\rm B} \lesssim \omega_0 \lesssim 50/T_{\rm B}$. For such parameters of the noise, the decay is strongly enhanced by the energy matching condition discussed before. There is a less pronounced enhancement for a wide range of larger Γ values. Regions of suppresion of decay exist, especially for small ω_0 (for all Γ) and for large ω_0, if Γ is small. The landscapes shown in Figures 6.13 and 6.14 highlight how the Landau–Zener tunneling can be engineered by choosing noise with specific properties. Since the landscape is rather smooth, the here predicted behavior of the decay is also robust to small experimental uncertainties of the noise parameters. Each figure contains 145 data points (Γ,ω_0), and for each data point, an average over 20 realizations of the noise has been performed.

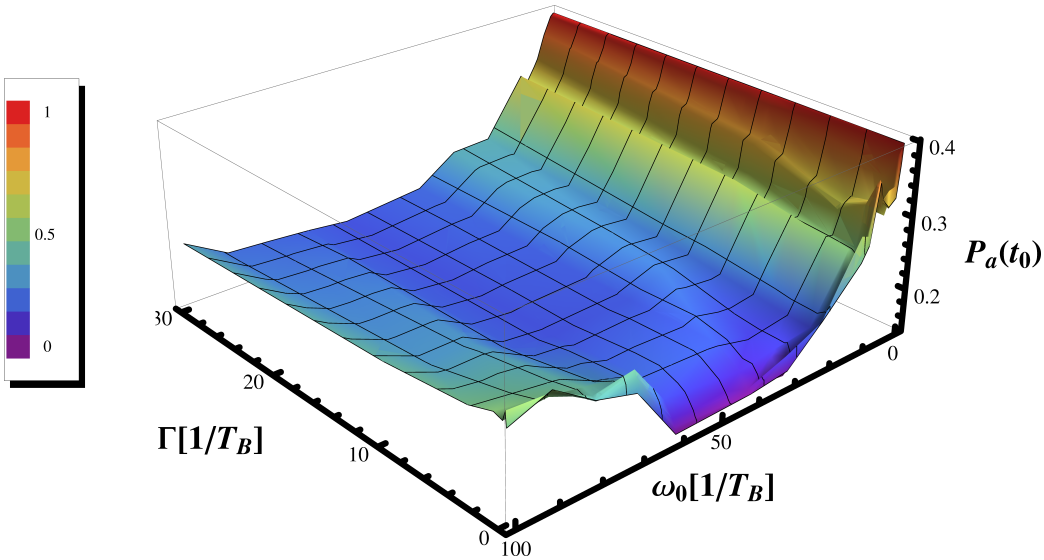

Figure 6.13: The survival probability at $t_0 \approx 6\ T_{\rm B}$ over the plane of the noise parameters (Γ, ω_0) for $V_0 = 2.5$ and $F_0 = 1.5$.

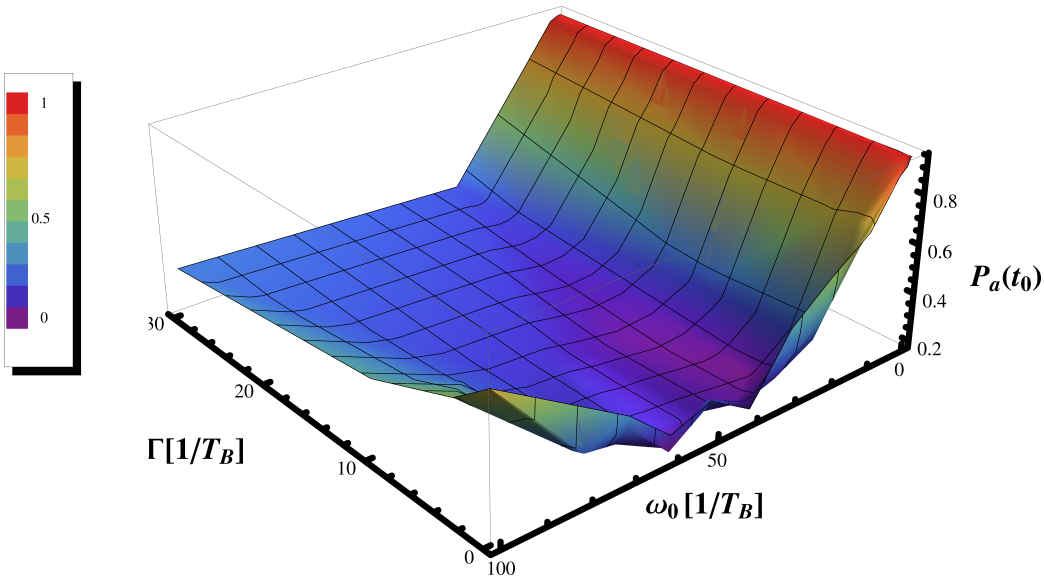

Figure 6.14: The survival probability at $t_0 \approx 6\ T_{\rm B}$ over the plane of the noise parameters $(\Gamma,\ \omega_0)$ for $V_0 = 4$ and $F_0 = 1.3$.

6.4.5 Impact of $\langle\phi(t)^2\rangle$ on tunneling

Up to here, $\langle\phi(t)^2\rangle = T/\omega_0^2$ was constant for all the calculations. It is important to understand how this parameter can affect the tunneling probability. We study the time-evolution of the survival probability for different ratios of T/ω_0^2. Figure 6.15 shows $P_{\rm a}(t_0)$ at $t_0 \approx 6\ T_{\rm B}$ versus ω_0 for two group of system parameters: (a) $V_0 = 2.5$, $F_0 = 1.5$ (non-RET), and (b) $V_0 = 4$, $F_0 = 1.48$ (RET), with $\phi(t)$ given by harmonic noise with damping frequency $\Gamma = 5/T_{\rm B}$ and four different $\langle\phi^2\rangle = 0.01,\ 0.25,\ 1$ and 10.

For $\omega_0 \lesssim 1/T_{\rm B}$, where the noise is in the slowly varying regime, $P_{\rm a}(t_0)$ is larger than in the other regions, i.e., noise suppresses the tunneling probability of the condensate. By increasing the oscillation frequency ω_0 of the harmonic noise, $P_{\rm a}(t_0)$ decreases and a minimum appears where the tunneling rate is strongly enhanced compared with the reference system (thick black solid line). This global minimum moves to smaller ω_0 for larger $\langle\phi(t)^2\rangle$. This means that a larger $\langle\phi(t)^2\rangle$ (stronger noise) leads to an earlier enhancement of the tunneling (see the data for $T/\omega_0^2 = 10$ shown by green open squares). By further increasing ω_0, the harmonic noise enters the regime where the effective model can describe the dynamics of the system. In this regime, the noise oscillates very fast and the value of $P_{\rm a}(t_0)$ in the noisy system lies in the vicinity the corresponding value calculated by implementing the effective potential.

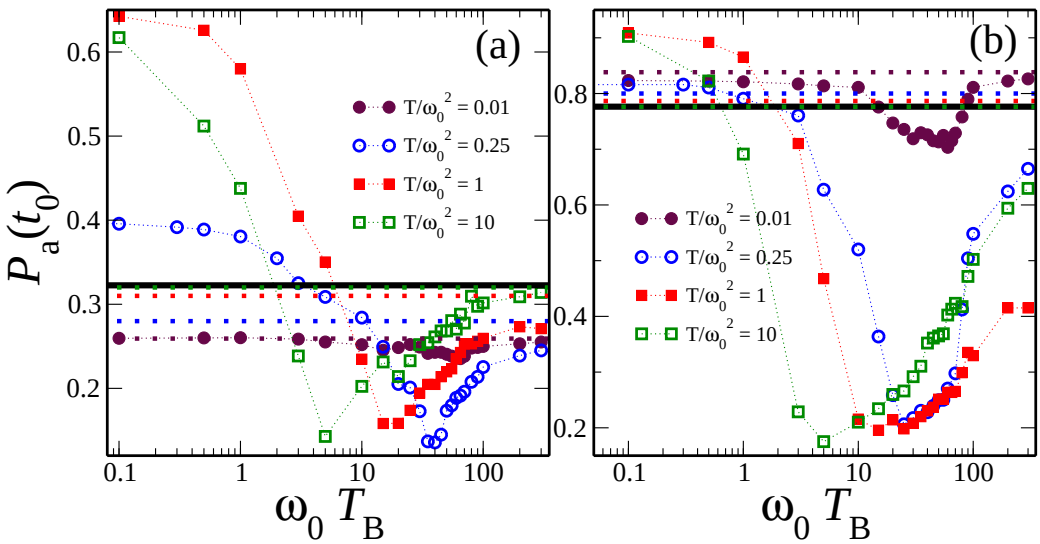

Figure 6.15: The survival probability at $t_0 \approx 6\ T_{\rm B}$ for the system parameters (a) $V_0 = 2.5$ and $F_0 = 1.5$; (b) $V_0 = 4$ and $F_0 = 1.48$. The noise parameter $\Gamma = 5/T_{\rm B}$, the variance of the noise: $\langle \phi(t)^2 \rangle \equiv T/\omega_0^2 = 0.01$ (maroon filled circles), $T/\omega_0^2 = 0.25$ (blue open circles), $T/\omega_0^2 = 1$ (red filled squares) and $T/\omega_0^2 = 10$ (green open squares) and a scan over ω_0. Results from the effective potential are shown by colored dotted lines. The survival probability of the corresponding reference system is shown by black solid lines.

The effect of noise on the tunneling probability shown in Figure 6.15 seems systematic and remains the same for any group of (V_0,F_0). The shifts in the minimum of $P_{\rm a}(t_0)$ depend on T/ω_0^2, which is essentially the variance of the harmonic noise and specify the strength of noise fluctuations. This ratio is used to calculated the amplitude (given by $\beta = \exp(-T/\omega_0^2)$) of the second lattice in the effective potential. Moreover, β is a benchmark for the results, that is, when $\beta \to 1$ (for $T/\omega_0^2 < 1$) the results remain in the vicinity of the effective model prediction, while when $\beta \to 0$ (for $T/\omega_0^2 \leq 1$), there is less agreement between the data shown by symbols and the effective model (dotted lines). Therefore, we rescale the results by $\sqrt{T/\omega_0^2}$ as the rescaling parameter. Figure 6.16 shows the rescaled $P_{\rm a}(t_0)$ in the same system and for the same noise parameters as in Figure 6.15. As seen in Figure 6.16, a transition happens at around $\sqrt{T} \approx 1/T_{\rm B}$ from the regime of slowly varying noise to the regime of fast changing noise. For $\sqrt{T} < 1/T_{\rm B}$, the noise does not assist the tunneling, especially the larger the ratio T/ω_0^2 is (note: $\beta \to 0$). Moving to the right ($\sqrt{T} > 1/T_{\rm B}$), the noise enhances the tunneling rate and the minimum valley of all the data sets lies in the same range of the rescaled parameter on the horizontal axis (i.e., at around

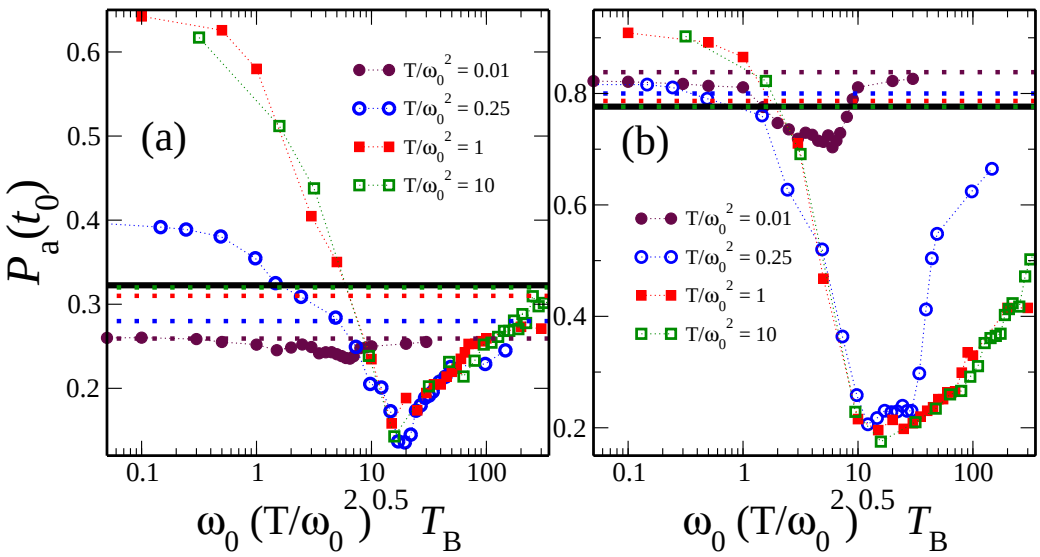

Figure 6.16: The rescaled survival probability $P_a(t_0)$ at $t_0 \approx 6\ T_B$ versus the $\omega_0\sqrt{T/\omega_0^2}$ for the same parameters as in Figure 6.15: (a) $V_0 = 2.5$ and $F_0 = 1.5$; (b) $V_0 = 4$ and $F_0 = 1.48$.

$\sqrt{T} \approx 10/T_B$). For small $\langle\phi(t)^2\rangle$ ($\beta \to 1$), however, the oscillation amplitude of the noise is small, and therefore, the noise does not enhance the tunneling strongly, but only remains close to effective model's result. As a result, the minimum is shifted upwards, i.e., less tunneling of the condensate atoms for smaller $\langle\phi(t)^2\rangle$. This can be seen clearly in the system with $V_0 = 4\ E_{rec}$ shown in Figure 6.16(b). The results in this figure confirm that the tunneling rate depends also on T.

6.4.6 Impact of T on the tunneling rate

To investigate the effect of the parameter T, calculations can be done for a fixed T while running a scan over the oscillation frequency ω_0. Figure 6.17 shows the survival probability $P_a(t_0)$ at time $t_0 \approx 6\ T_B$ for the three sets of system parameters as presented in Figure 6.11: (a) and (b) $V_0 = 2.5$, $F_0 = 1.25$ (RET); (c) and (d) $V_0 = 2.5$, $F_0 = 1.5$ (non-RET); (e) and (f) $V_0 = 4$ and $F_0 = 1.48$ (RET). Choosing different sets of system parameters helps to understand the possible interplay between the impact of the noise and the system's characteristic parameters. The calculations were done for $\Gamma = 5/T_B$ and different values of $T = 0.01/T_B^2,\ 0.1/T_B^2,\ 1/T_B^2$, and $10/T_B^2$. The left panels show the survival probability $P_a(t_0)$ against oscillation frequency ω_0 of the noise and the right panels exhibit the rescaled data of $P_a(t_0)$ against ω_0^2/T.

Small ω_0: As seen in Figure 6.17, the data shown in the left panels depict a step-like structure with respect to ω_0. For small ω_0 (slowly varying regime of the noise) $P_{\rm a}(t_0)$ is constant and the data shown by symbols, for cases with $T \leq 1/T_{\rm B}^2$, are well above the reference system (black dashed line), while for $T = 100/T_{\rm B}^2$, the survival probability $P_{\rm a}(t_0)$ lies below the one of the reference system. Increasing the oscillation frequency of the noise, a transition happens at some ω_0 and $P_{\rm a}(t_0)$ starts to decrease. It can be seen in the left panels of Figure 6.17 that these transition points are shifted depending on the value of T. For example, for $T = 0.001/T_{\rm B}^2$ (black filled circles), the survival probability $P_{\rm a}(t_0)$ starts to decrease at around $\omega_0 \approx 0.05/T_{\rm B}$, while for $T = 1/T_{\rm B}^2$ it happens around $\omega_0 \approx 1/T_{\rm B}$. One can understand from these quantities that the transition actually happens when $\omega_0 \approx \sqrt{T}$.

Large ω_0: By further increasing the oscillation frequency ω_0, $P_{\rm a}(t_0)$ saturates around a value gained using the effective model (shown by dotted line). Since in this regime, $T/\omega_0^2 \ll 1$, then in the effective model $\beta \equiv \exp(-2T/\omega_0^2) \to 1$. For $T \geq 1/T_{\rm B}^2$, the step-like structure is somewhat different and for $T = 100/T_{\rm B}^2$, the survival probability $P_{\rm a}(t_0)$ (violet open triangles) is below the dashed line (the reference system) and then it rises up at around $\omega_0 \approx 10/T_{\rm B}$. For large values of ω_0, it lies in the vicinity of the magenta dotted line which is calculated using the effective model. The reason of such a behavior is that for $\omega_0 \leq 1$, if $T > 1/T_{\rm B}^2$, the ratio $T/\omega_0^2 \gg 1$ while it is $T/\omega_0^2 \ll 1$ for the cases with $T < 1/T_{\rm B}^2$. For $T/\omega_0^2 \gg 1$, the noise is very strong and the amplitude of its oscillations is very large and therefore, it leads to a larger tunneling probability. As shown in Figure 6.8, for a large $T > 1$, even the slowly varying noise is strong enough to change the potential and therefore, enhances the tunneling.

From the discussion above and the data shown in Figure 6.17, one realizes that the transition point depends on T/ω_0^2. This parameter being smaller or larger than 1 distinguishes two regimes in the system which result in different rates of tunneling (hence the step structure in Figure 6.17). One regime is the slowly varying noise regime (small ω_0) where the phase is constant. The other regime is the fast oscillating regime. The results in the fast oscillating regime (large ω_0) can be described by the effective model (shown by dotted line) for $T/\omega_0^2 \ll 1$ which gives $\beta \equiv \exp(-2T/\omega_0^2) \to 1$.

Scaling: To confirm the above discussion, the data are rescaled by the variance $\langle \phi(t)^2 \rangle \equiv T/\omega_0^2$ of the harmonic noise and shown in the right panels of Figure 6.17. As seen, the horizontal axis is now ω_0^2/T, which is the characteristic ratio to calculate β. All the results with $T \leq 1/T_{\rm B}^2$ lie on top of each other. For all the cases, $P_{\rm a}(t_0)$ starts to decrease (or increases for the case of $T = 100/T_{\rm B}^2$) at $\omega_0^2/T \approx 1$, and it continues falling down (rising up) until $\omega_0^2/T \approx 100$. Here is the regime, where the effective model is valid.

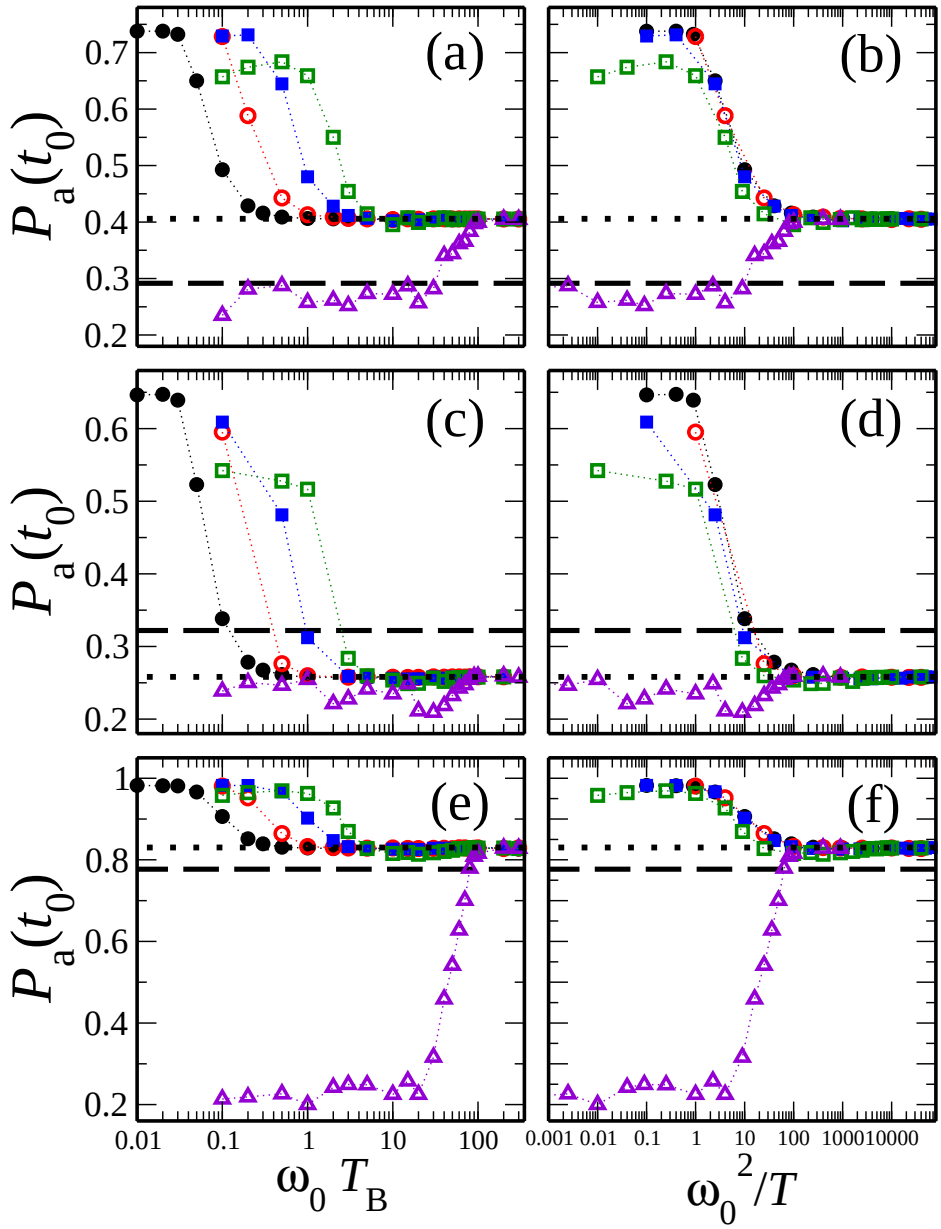

Figure 6.17: The survival probability at $t_0 \approx 6\ T_B$ for the system parameters (a) and (b) $V_0 = 2.5$ and $F_0 = 1.25$; (c) and (d) $V_0 = 2.5$ and $F_0 = 1.5$; (e) and (f) $V_0 = 4$ and $F_0 = 1.48$. A scan over the noise parameter ω_0, while $\Gamma = 5/T_B$, and $T = 0.001/T_B^2$ (black filled circles), $T = 0.01/T_B^2$ (red open circles), $T = 0.1/T_B^2$ (blue filled squares), $T = 1/T_B^2$ (green open squares), and $T = 100/T_B^2$ (violet open triangles). $P_a(t_0)$ of the corresponding reference system is shown by black solid lines and for the effective model with $\beta = 1$ by dotted line.

The value of $\beta \equiv \exp(-T/\omega_0^2)$ used in the effective model depends also on the rescaling parameter. Two regimes are distinguished: (i) $T/\omega_0^2 > 1$ which gives $\beta \to 0$, and (ii) $T/\omega_0^2 < 1$ which gives $\beta \to 1$. For the regime (i), the noise is slowly varying and results deviate from the one from the effective model, while for (ii) the noise is fast and the results agree with the one of the effective model. Therefore, for $\omega_0^2/T > 100$, all $P_{\rm a}(t_0)$ lie around a value (shown by the dotted line in each panel) which is calculated using the effective model with $\beta = 1$ (for the reason see the discussion above). For the system parameters which fulfill the RET condition this value lies above the reference dashed line, whilst in the non-RET case this value is below the reference dashed line, i.e., we get an enhancement of the tunneling rate in comparison with the reference system in the non-RET case.

Impact of α:

From Eq. (6.5), α is calculated for the amplitude αV of the lattices, as defined in Eq. (6.2). Therfore, the value of α has a crucial effect on the tunneling probability. Since $\beta \equiv \exp(-2T/\omega_0^2)$ is different for each data point in Figure 6.17, α also gains different values. To check the impact of α, the same calculations as in Figure 6.17 are done keeping $\alpha = 1$. The survival probability $P_{\rm a}(t_0)$ at $t_0 \approx 6\,T_{\rm B}$ are shown in Figure 6.18 for two groups of system parameters: (a) and (b) $V_0 = 2.5$, $F_0 = 1.25$ (RET); (c) and (d) $V_0 = 2.5$, $F_0 = 1.5$ (non-RET). The system with $V_0 = 4$ and $F_0 = 1.48$ (RET), as seen in Figure 6.17(e) and (f), shows in principle the same behavior as $V_0 = 2.5$, $F_0 = 1.25$ (RET). Therefore, it is not shown any more in Figure 6.18.

$T < 1/T_{\rm B}^2$: For small T, the survival probability $P_{\rm a}(t_0)$ remains very close to the prediction from the effective model (dashed line) almost independent from the value of ω_0 (see the inset in Figure 6.18(a)). In this regime, the noise is not strong enough to affect the system and $\beta \equiv \exp(-2T/\omega_0^2) \to 1$. Therefore symbols lie close to the dashed line for all ω_0.

$T \geq 1/T_{\rm B}^2$: For $T \geq 1/T_{\rm B}^2$, the noise is strong and T/ω_0^2 is larger than in the case above, and the results show a different behavior. The survival probability agree with the effective model for a large oscillation frequency $\omega_0 \gtrsim 100$, while it decreases by decreasing ω_0. For $\omega_0 < 100$, the effective model is not valid any more and all $P_{\rm a}(t_0)$ fall below the dashed line (see Figure 6.18(a) and (c)). In fact, by further decreasing the parameter ω_0 (or ω_0^2/T), the noise recovers the slowly varying regime, and for a very small ω_0 (e.g., $\omega_0 \lesssim 1/T_{\rm B}$), the phase $\phi(t)$ is essentially a constant random number for long times, where averaging over 20 realizations of this random number gives a constant $P_{\rm a}(t_0)$.

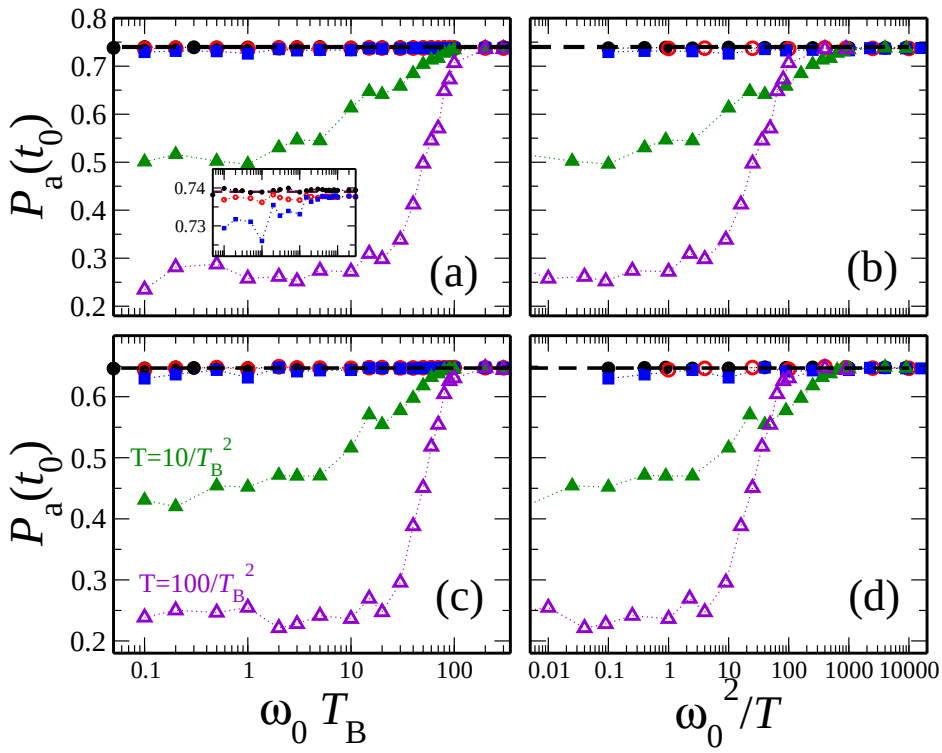

Figure 6.18: The survival probability at $t_0 \approx 6\ T_{\rm B}$ for the system with $\alpha = 1$ and parameters (a) and (b) $V_0 = 2.5$, $F_0 = 1.25$; (c) and (d) $V_0 = 2.5$, $F_0 = 1.5$. A scan over the noise parameter ω_0, while $\Gamma = 5/T_{\rm B}$, and $T = 0.001/T_{\rm B}^2$ (black filled circles), $T = 0.01/T_{\rm B}^2$ (red open circles), $T = 0.1/T_{\rm B}^2$ (blue filled squares), $T = 1/T_{\rm B}^2$ (light green open squares), $T = 10/T_{\rm B}^2$ (green filled triangles) and $T = 100/T_{\rm B}^2$ (violet open triangles). $P_{\rm a}(t_0)$ of the corresponding effective potential with $\beta = 1$ is shown by the dashed line. Inset in (a): a close up view of symbold for the first three T.

6.4.7 Summary of the results

The results shown in this section confirm that the tunneling rate of the condensate atoms in the time-dependent disordered lattices with the phase $\phi(t)$ given by the harmonic noise can be manipulated by changing the noise parameters. In summary:

- The noise, which is the phase for the second lattice, effectively normalizes the amplitude of the second lattice and affects the tunneling probability. This was confirmed by our effective model defined in Eq. (6.4) which gives a perfect prediction by renormalizing the amplitude of the second lattice for the limit of fast noise ($\omega_0 \geq 100/T_{\rm B}$).

- For small ω_0, the noise recovers the exponentially correlated noise with a large correlation time. In this limit ($\omega_0 \ll 1/T_{\mathrm{B}}$), the noise is almost constant during the time scale of the system and the potential is similar to the bichromatic lattice with a constant phase. In most of the cases, the noise suppresses the tunneling in this ragime, unless for large strength T of the noise.

- Between these two regimes, the tunneling rate can increase (see Figures 6.11 and 6.15). A valley appears in a range of $10/T_{\mathrm{B}} < \omega_0 < 100/T_{\mathrm{B}}$. Comparing the energy induced by the noise (given by $\Delta\tilde{\omega}$) to the energy scale of the system (given by ΔE in E_{rec} unit), it turned out that these two energies are comparable in this parameter regime.

- The results in Figure 6.15 showed that the variance $\langle\phi(t)^2\rangle$ is involved effecting the tunneling probability. This value specifies the amplitude of the noise fluctuations and equals T/ω_0^2. The results in Figure 6.15 showed that the minimum is at smaller ω_0 for larger T/ω_0^2 (the valley was shifted to the left). For a small variance (e.g., $\langle\phi(t)^2\rangle = 0.01$) of the noise, $\beta \equiv \exp(-T/\omega_0^2) \to 1$ and the results remain close to the corresponding value from the effective model.

- The latter led us to rescale our results and thereby reduces the parameter dependence of the system. The rescaling parameter turned out to be related to $\langle\phi(t)^2\rangle \equiv T/\omega_0^2$. In Figure 6.15, the data were rescaled by $\sqrt{T/\omega_0^2}$ which resulted in a universal behavior of $P_{\mathrm{a}}(t_0)$. This means that the effective parameter on the tunneling is actually the strength of the noise which is given by T. This led us to study the impact of T independently.

- Keeping T constant and scanning over ω_0 showed that the transition between the slowly varying regime (where the phase is constant) and the fast noise regime (where the effective model is valid) happens at the same T/ω_0^2. For $\omega_0^2/T < 1$ ($\beta \to 1$), the noise is constant and suppresses the tunneling (except for the very strong noise with a large T). For $\omega_0^2/T > 100$, the noise is fast and can be predicted by our effective model (see Figure 6.17).

- Keeping the amplitude of the potential constant (by keeping $\alpha = 1$ fixed), the results in Figure 6.18 showed that T and $T/\omega_0^2 \equiv \langle\phi(t)^2\rangle$ are the effective parameters on the tunneling probability. It was demonstrated that for larger values of these parameters the tunneling rate systematically increases.

6.5 Incommensurable Lattices with a time-dependent deterministic phase

Here we study the effect of the deterministic time-dependent phase. It was presented in section 3.2.3 that the time–dependent phase $\phi(t)$ can be given by a sinusoidal function (see Eq. (3.37)). The spectral distribution of this function is a delta function and this delta function in the numerical calculation has a finite width and height. The idea is that this spectral distribution resembles the one for harmonic noise with a peak at $\tilde{\omega}$. Therefore, the deterministic phase can be another benchmark for our calculations in the presence of harmonic noise, when their spectral distribution are comparable and $\tilde{\omega} \approx \omega_{\mathrm{d}}$ (see the end of section 3.2.3). The time-dependent disorder potential is now written as

$$V(x,t) = \alpha V \left[\sin^2\left(\frac{\pi x}{d_{\mathrm{L}}}\right) + \sin^2\left(\frac{\pi x}{d'_{\mathrm{L}}} + A_{\mathrm{d}} \cos(\omega_{\mathrm{d}} t + \varphi)\right)\right]. \tag{6.8}$$

Both lattices have the same amplitude αV and incommensurable lattice constants d_{L} and d'_{L}. The phase is defined by a cosine function with amplitude A_{d} and a period of oscillations $2\pi/\omega_{\mathrm{d}}$. There is also a random phase φ in this oscillatory function, which is picked from a flat distribution. Therefore, we should average our results over this phase drawn randomly in $[0, 2\pi]$.

6.5.1 Effective model

For a large oscillation frequency ω_{d} compared with the inverse Bloch period $1/T_{\mathrm{B}}$, the phase is a fast oscillating function. By averaging over one period $2\pi/\omega_{\mathrm{d}}$ of oscillations, it is possible to calculate a static effective potential which can model the effect of the time-dependent oscillatory phase in the regime of large ω_{d}, just as it was done in section 6.2. This static effective potential is calculated as follows

$$\begin{aligned} V_{\mathrm{eff}}(x) &= \frac{\omega_{\mathrm{d}}}{2\pi} \int_0^{\frac{2\pi}{\omega_{\mathrm{d}}}} V(x,t)\, dt \\ &= \frac{\alpha V \omega_{\mathrm{d}}}{2\pi} \left[\frac{2\pi}{\omega_{\mathrm{d}}} \sin^2\left(\frac{\pi x}{d_{\mathrm{L}}}\right) + \int_0^{\frac{2\pi}{\omega_{\mathrm{d}}}} \sin^2\left(\frac{\pi x}{d'_{\mathrm{L}}} + A_{\mathrm{d}} \cos(\omega_{\mathrm{d}} t + \varphi)\right) dt \right] \\ &= \alpha V \left[\sin^2\left(\frac{\pi x}{d_{\mathrm{L}}}\right) + J_0(2A_{\mathrm{d}}) \sin^2\left(\frac{\pi x}{d'_{\mathrm{L}}}\right)\right]. \end{aligned} \tag{6.9}$$

Therefore, the time-dependent oscillatory phase is effectively renormalizing the amplitude of the second lattice, and results in a static effective potential. According to our calculation in Eq. (6.9), the amplitude of the second term in the

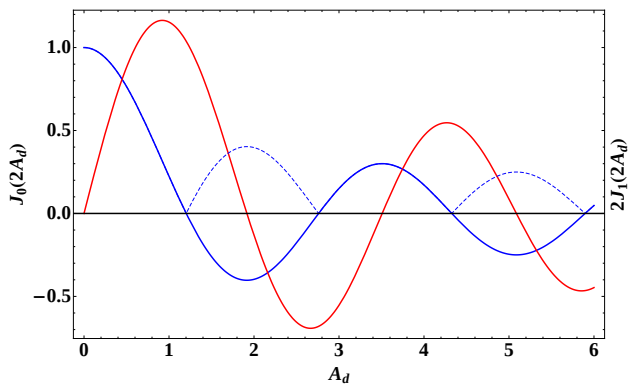

Figure 6.19: The Bessel function of the first kind $J_0(2A_\mathrm{d})$ (blue curve) and its first derivative $2J_1(2A_\mathrm{d})$ (red curve). The blue dashed line show the absolute value of the Bessel function $|J_0(2A_\mathrm{d})|$

effective potential $V_\mathrm{eff}(x)$ is now given by the zero-th order Bessel function of the first kind $J_0\left(2A_\mathrm{d}\right)$. The argument of this Bessel function depends only on the amplitude A_d of the cosine function given in Eq. (6.8).

the plot of $J_0\left(2A_\mathrm{d}\right)$ as a function of A_d is shown by the blue solid line in Figure 6.19. One sees that this function equals zero for some values of A_d. Therefore, the amplitude of the second term in the effective potential, defined in Eq. (6.9), is zero for these values of A_d. For such cases, the second lattice is effectively vanishing and the potential recovers the reference system potential, i.e., $\alpha V \sin^2\left(\pi x/d_\mathrm{L}\right)$.

For $A_\mathrm{d} = 0$, it is $J_0\left(2A_\mathrm{d}\right) = 1$, and the amplitude of the second lattice in the static effective potential $V_\mathrm{eff}(x)$ has its maximum value. For non-zero A_d, the extremum points of $J_0\left(2A_\mathrm{d}\right)$ can be specified finding the zeros of its derivative. The derivative of the Bessel function of the first kind is $J_0'\left(2A_\mathrm{d}\right) = 2J_1\left(2A_\mathrm{d}\right)$ and is shown by the red solid line in Figure 6.19. For the values of A_d, where $J_1\left(2A_\mathrm{d}\right) = 0$, the zero-th order Bessel function $J_0\left(2A_\mathrm{d}\right)$ possesses a local maximum or minimum, and the amplitude of the second lattice is larger than in the other cases (except of the case $A_\mathrm{d} = 0$), and hence the second lattice has its maximum contribution in the effective potential.

Figure 6.20 shows a comparison between the results gained by integrating the real Hamiltonian with the potential defined by Eq. (6.8) and the results calculated by using the effective model defined in Eq. (6.9). Panel (a) shows our observable $P_\mathrm{a}(t_0)$ versus the amplitude A_d. As seen, the results of both calculation show perfect agreement with each other. For values of A_d where $J_0\left(2A_\mathrm{d}\right) = 0$, the results of the effective model lie on the dashed line ($P_\mathrm{a}(t_0)$ for the reference sys-

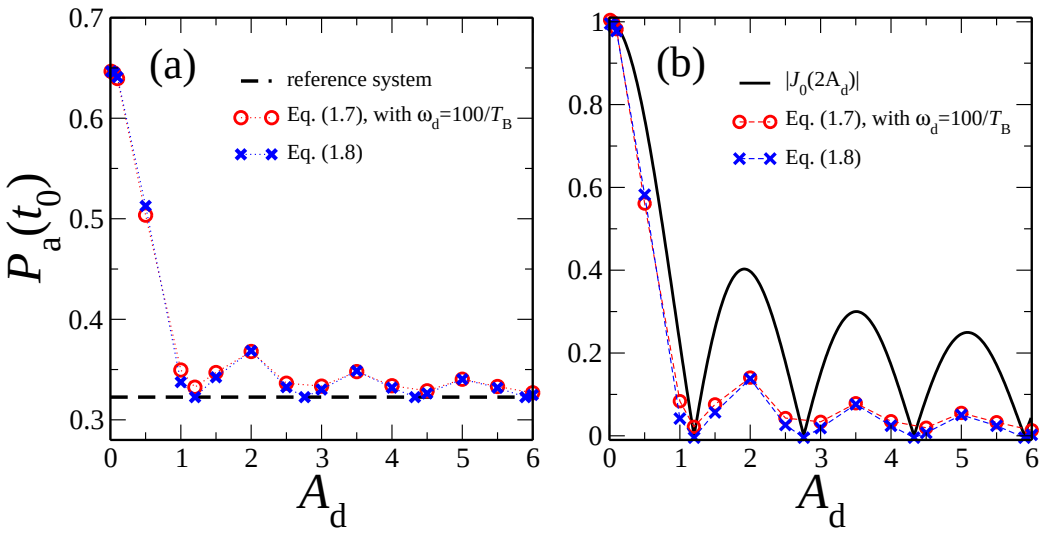

Figure 6.20: A comparison between the effective model and the real system defined by Eq. (6.8). The survival probability at $t_0 \approx 6\ T_{\rm B}$ for the system with $V_0 = 2.5$, $F_0 = 1.5$ and $\alpha = 1$. A scan over the amplitude $A_{\rm d}$ of the phase, for (a) results of integrating Hamiltonian with the potential defined by Eq. (6.8) with a large $\omega_{\rm d} = 100/T_{\rm B}$ (red circles). $P_{\rm a}(t_0)$ for the reference system is shown by black dashed line. (b) The absolute value of the Bessel function $|J_0\,(2A_{\rm d})|$ (black solid line). $P_{\rm a}(t_0)$ in the effective model defined in Eq. (6.9) is shown by blue crosses.

tem), and this agreement nicely confirms the above discussion. In panel (b), the results shown in panel (a) are rescaled and compared to the absolute value of the Bessel function $|J_0\,(2A_{\rm d})|$ (black solid line). Symbols and the black curve, show hills and valleys at the same values of $A_{\rm d}$. Our observable resembles qualitatively a behavior that is essentially determined by the Bessel function.

6.5.2 Impact of the oscillation frequency $\omega_{\rm d}$ and the amplitude $A_{\rm d}$ on the tunneling

To study the impact of a time-dependent potential with a deterministic phase on the tunneling probability of the condensate atoms, the time-resolved survival probability is calculated. Figure 6.21 shows the survival probability at $t \approx 6T_{\rm B}$ in the presence of the time-dependent potential versus the amplitude $A_{\rm d}$ of the oscillatory phase. The shown data points are the results of averaging over 20 realizations of the phase φ (which is picked from a flat distribution). Different symbols correspond to different values of the oscillation frequency $\omega_{\rm d} = 0.1/T_{\rm B}$

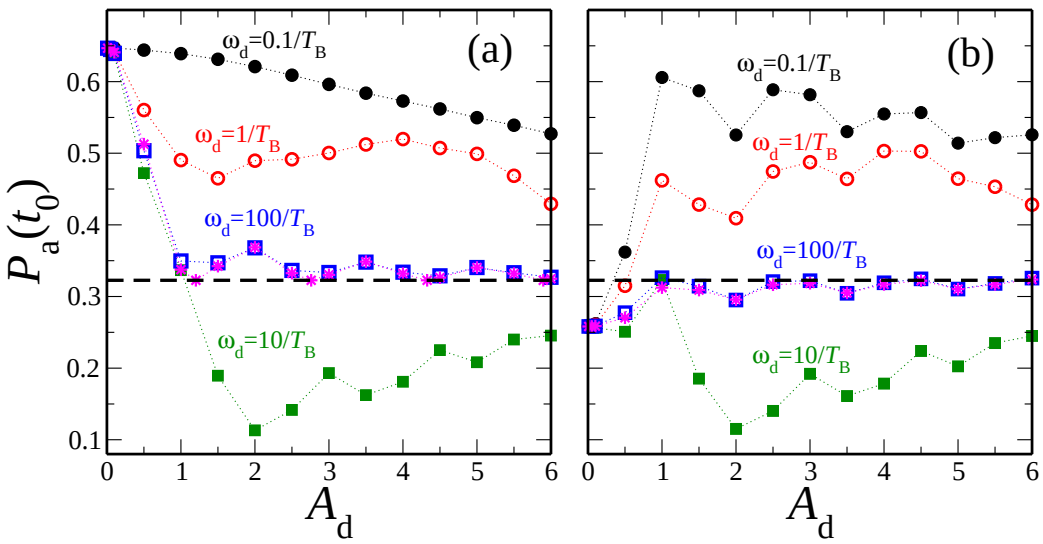

Figure 6.21: The survival probability at $t_0 \approx 6\ T_{\rm B}$ for the system with $V_0 = 2.5$, $F_0 = 1.5$ and (a) $\alpha = 1$, and (b) $\alpha \neq 1$. A scan over the amplitude $A_{\rm d}$ of the phase, for $\omega_{\rm d} = 0.1/T_{\rm B}$ (black filled circles), $\omega_{\rm d} = 1/T_{\rm B}$ (red open circles), $\omega_{\rm d} = 10/T_{\rm B}$ (green filled squares), $\omega_{\rm d} = 100/T_{\rm B}$ (blue open squares). $P_{\rm a}(t_0)$ of the correspondence effective potential given by Eq. (6.9) is shown by magenta stars, and $P_{\rm a}(t_0)$ for the reference system is shown by black dashed line

(black filled circles), $1/T_{\rm B}$ (red open circles), $10/T_{\rm B}$ (green filled squares), and $100/T_{\rm B}$ (blue open squares). All the results shown in Figure 6.21(a) were calculated for $\alpha = 1$, $V_0 = 2.5$, and $F_0 = 1.5$. For small $\omega_{\rm d}$ (e.g., $\omega_{\rm d} = 0.1/T_{\rm B}$ shown by black filled circles), when the phase is a slowly oscillating function with a oscillation period larger than the time scale $T_{\rm B}$ of the system, the survival probability $P_{\rm a}(t_0)$ shows less decay compared with the other cases. By increasing the oscillation frequency $\omega_{\rm d}$ (faster oscillation of the phase), $P_{\rm a}(t_0)$ decays faster. The rate of decay is faster for small values of $A_{\rm d}$ ($A_{\rm d} \lesssim 2$) and then shows only some fluctuations for even larger value of $A_{\rm d}$. The tunneling probability is enhanced for $\omega_{\rm d} = 10/T_{\rm B}$ (green filled squares) compared with the other values of $\omega_{\rm d}$. However, for a very fast oscillation of the phase (i.e., for $\omega_{\rm d} = 100/T_{\rm B}$ shown by blue open squares), the survival probability $P_{\rm a}(t_0)$ increases and symbols lie close to the black dashed line (reference system). For such large oscillation frequency the system is in the limit that the definition of the static effective potential given in in Eq. (6.9) is valid. As seen, the results (magenta stars) from the effective model lie on top of the results obtained from the time-dependent system with the potential given in Eq. (6.8) and with $\omega_{\rm d} = 100/T_{\rm B}$. This means, in the very fast oscillating regime of the phase, the effect of the time-dependent phase is similar

to the Bessel function $J_0\left(2A_\mathrm{d}\right)$ rescaling the amplitude of the second lattice. As shown in Figure 6.19, the Bessel function can be zero for specific values of A_d and for these values of A_d the amplitude of the second lattice vanishes and the decay rate of the survival probability should be the same as in the reference system. The results shown by blue and magenta symbols confirm this idea when for some values of A_d, they lie close to the dashed line (reference system).

The same calculations can be done for $\alpha \neq 1$. Using $\beta = J_0(2A_\mathrm{d})$, α can be calculated from Eq. (6.5). Results are shown in Figure 6.21(b) and as seen the data show the same behavior as the the case with $\alpha = 1$. The difference in starting points arises because of the different values of α for these points compared with $\alpha = 1$. In fact, for these points, β has its largest values and hence results in a smaller α and a higher tunneling probability. Therefore, for $A_\mathrm{d} < 1$, $P_\mathrm{a}(t_0)$ in panel (b) is smaller than the one in panel (a). The effective model gives the data points shown by magenta stars. These data points demonstrate a perfect agreement with the results gained using the potential given in Eq. (6.8) with a large oscillation frequency, $\omega_\mathrm{d} = 100\ /T_\mathrm{B}$ of the phase, as in panel (a).

6.5.3 One tilted lattice with a time-dependent deterministic phase

To study the impact of the phase directly on the effective amplitude of the lattice and the tunneling rate of the condensate atoms from the ground band, here a system with a single periodic lattice with a time-dependent deterministic phase is considered. The potential is defined as

$$V_\mathrm{dis}\left(x,t\right) = V_0 \sin^2\left(\frac{\pi x}{d'_\mathrm{L}} + A_\mathrm{d}\cos(\omega_\mathrm{d} t + \varphi)\right). \tag{6.10}$$

Since the system is periodic, the step structures of the survival probability are preserved. Such step structures are depicted in Figure 6.22. This Figure shows the time evolution of the survival probability in the system with lattice depth $V_0 = 2.5$ and the force $F_0 = 1.5$ for fixed $A_\mathrm{d} = 2$ and different ω_d of the time-dependent phase. The length of the steps corresponds to the Bloch period $T'_\mathrm{B} \equiv 2\pi\hbar/(F d'_\mathrm{L})$, while the time scale on the horizontal axis was kept to the original T_B that has been considered up to now. As seen in Figure 6.22, the survival probability for $\omega_\mathrm{d} = 100/T_\mathrm{B}$ (blue open squares) lies perfectly on top of the survival probability calculated in the effective system. The effective potential is defined as

$$V_\mathrm{eff}\left(x\right) = \beta V \sin^2\left(\frac{\pi x}{d'_\mathrm{L}}\right), \tag{6.11}$$

where $\beta = J_0\left(2A_\mathrm{d}\right)$ as calculated in Eq. (6.9).

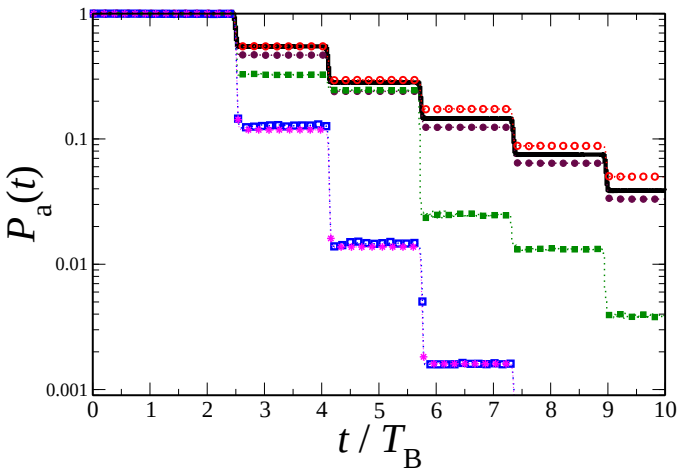

Figure 6.22: Time evolution of the survival probability in the system defined by the potential given in Eq. (6.10) with $V_0 = 2.5$, $F_0 = 1.5$. For $A_d = 2$, and different oscillation frequencies: $\omega_d = 0.1/T_B$ (maroon filled circles), $\omega_d = 1/T_B$ (red open circles), $\omega_d = 10/T_B$ (green filled squares), $\omega_d = 100/T_B$ (blue open squares). $P_a(t_0)$ of the corresponding effective potential given by Eq. (6.11) is shown by magenta stars, and $P_a(t_0)$ for the reference system is shown by black dashed line.

Figures 6.23(a) and (b) show the survival probability $P_a(t_0)$ at $t = 6\ T_B$ for the same system and a scan over the amplitude A_d. The survival probability $P_a(t_0)$ is calculated for different oscillation frequencies ω_d (specified with different symbols). Figure 6.23(a) exhibits the observable on the linear scale for $\omega_d = 0.1/T_B$ (maroon filled circles), $\omega_d = 1/T_B$ (red open circles), $\omega_d = 10/T_B$ (green filled squares), since they are not visible on the logarithmic scale in Figure 6.23(b). For a small ω_d, the phase is almost constant and hence time-independent. Therefore, the potential given in Eq. (6.10) is similar to the reference system. As seen, the values of $P_a(t_0)$ fluctuate close to the one of the reference system (dashed line) for the small $\omega_d = 0.1/T_B$. The larger the oscillation frequency of the phase is, the further the results are away from the reference system.

Using the static potential given in Eq. (6.11), one can calculate $P_a(t_0)$ for the effective model. The results of this calculation are shown by magenta stars in Figure 6.23(b). For the fast oscillating phase, it is expected to see an agreement between the results from the effective calculation (magenta stars) and the ones calculated in the presence of the time-dependent phase (blue open squares), for a large $\omega_d = 100/T_B$. The results in Figure 6.23(b) show a very good agreement for the values of A_d for which $J_0(2A_d) \neq 0$. But for those values of A_d where $\beta \equiv J_0(2A_d) = 0$, the effective potential vanishes, and therefore the survival

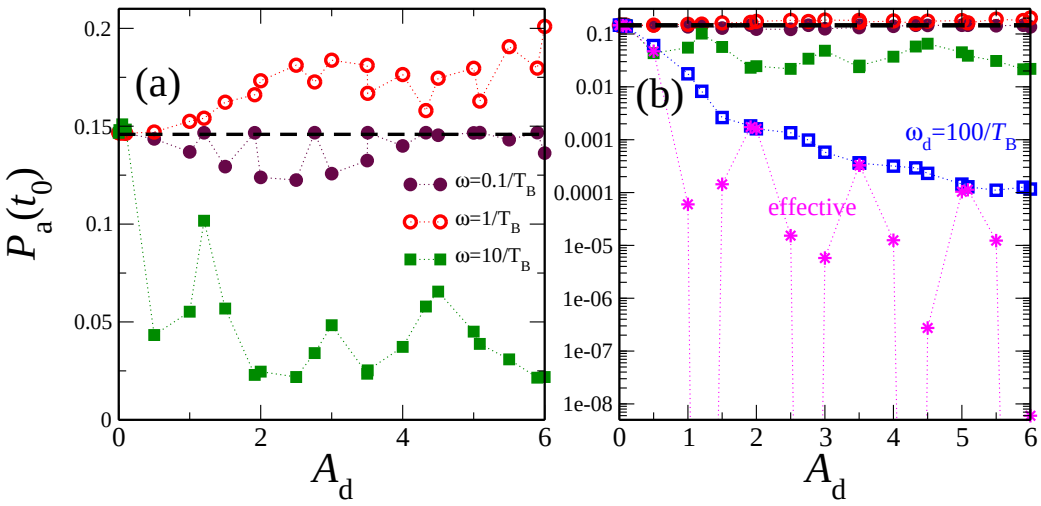

Figure 6.23: Survival probability at $t_0 \approx 6\ T_{\rm B}$ versus the amplitude $A_{\rm d}$ of the phase. The system is defined by the potential given in Eq. (6.10) with $V_0 = 2.5$, $F_0 = 1.5$. For different oscillation frequency of the phase: $\omega_{\rm d} = 0.1/T_{\rm B}$ (maroon filled circles), $\omega_{\rm d} = 1/T_{\rm B}$ (red open circles), $\omega_{\rm d} = 10/T_{\rm B}$ (green filled squares), $\omega_{\rm d} = 100/T_{\rm B}$ (blue open squares). (a) In the linear scale for the first three $\omega_{\rm d}$ mentioned above; (b) In logarithmic scale for all the cases. $P_{\rm a}(t_0)$ of the corresponding effective potential given by Eq. (6.11) is shown by magenta stars, and $P_{\rm a}(t_0)$ for the reference system is shown by black dashed line.

probability drops to zero abruptly (the free particle problem). As seen in Figure 6.23(b) by magenta stars, $P_{\rm a}(t_0)$ from the effective model is very small or zero, which does not agree with the results calculated in the system with the potential given in Eq. (6.10). Essentially, no matter how fast the oscillations of the phase are, the potential given by Eq. (6.10) is never exactly zero, and the lattice amplitude is always finite. This explains the discrepancy between data shown by magenta stars and the ones by blue open squares in Figure 6.23(b). A next-order correction should be considered in the calculation of the effective potential in Eq. (6.9) in order to have a better effective model.

The Hamiltonian of the system presented in Eq. (6.10) is equivalent to the Hamiltonian with a time-dependent driving force as defined in Eq. (2.31). By using gauge transformations in the Kramers–Henneberger frame (see the appendix), one can transform the Hamiltonian with a time-dependent driving force to the Hamiltonian for the periodic lattice with a deterministic time-dependent phase. This means that in such a way the noise can resemble the effect of the driving force as in Eq. (2.31).

The deterministic time-dependent phase has a delta function spectral distri-

bution with a peak at ω_{d}. This peak has a finite height and width due to the finite time steps of the numerical calculations (see section 3.2.3). This deterministic noise defines another benchmark for the harmonic noise in the limit of fast noise, if their spectral distributions are comparable. For that, the harmonic noise spectral-peak frequency $\tilde{\omega}$ should be approximately equal to the frequency ω_{d} of the deterministic phase. Furthermore, the area under the peak of the spectral distributions should be approximately equal, i.e., $A_{\mathrm{d}} \approx T/\omega_0^2$ (see section 3.2.3). For such a condition, the effect of both types of noise are comparable. In the presented sections we calculated analytically an effective model which can be used as a benchmark to describe our results in the regime of fast oscillating noise. By introducing these benchmarks in different limits of noise, and by scaling the parameters which reduces the parameter dependence of the system, it is possible understand the effect of the stochastic potentials. This latter achievement together with the summary presented in section 6.4 gives a fairly conclusive picture for all the linear (non-interacting) cases. Our results showed that the time-dependent noise in bichromatic lattice provide a further handle to control the tunneling probability.

Chapter 7

Conclusions and perspectives

7.1 Conclusion

Ultracold atoms in optical lattices provide an ideal model system for time-resolved studies of Landau–Zener tunneling. The results of our studies which were presented in this thesis show that it is possible to engineer the Landau–Zener tunneling probability of the ultracold atoms. Our numerical calculation together with the experimental results from the group of Ennio Arimondo in Pisa, all presented in chapter 5, confirmed that the tunneling from the ground band in tilted optical lattices can be controlled. This control is possible by changing the system parameters such as the lattice depth and the Stark force, or by changing the initial condition which is given by the initial width of the momentum distribution of the Bose–Einstein condensate. Moreover, for small values of lattice depth and Stark forces compared with the energy scale of the system, the two by two Landau-Zener model describes our system very well. However, to resolve the resonances in the long time decay rate, one must consider at least three energy bands. All of the mentioned parameters can be easily tuned experimentally [42, 43]. Furthermore, our calculations showed that atom-atom interactions affect the Landau–Zener tunneling probability and a repulsive interaction that typically leads to an enhancement of the Landau–Zener tunneling of the ultracold atoms from the ground band, confirming earlier results of Professor Ennio Arimondo's experimental group in Pisa [36, 37, 38].

Also, by projecting the state of the system onto different bases, it is possible to calculate the Landau–Zener tunneling probability in the adiabatic and diabatic basis, respectively. Our results confirm the existence of a finite temporal width for the transition in both bases and of strong oscillations of the survival probability in the diabatic basis. Our numerical results nicely agree with the experimental results from Pisa group [43]. The complete control over the parameters of the

lattice makes it possible to measure the tunneling dynamics in different bases by using different experimental measurement protocols [43].

The concept of the tunneling time was discussed in chapter 5 and a comparison was done to Vitanov analytical predictions [40]. Our studies showed that the tunneling time depends very much on the definition and also on the basis with which the calculations are performed. Our findings pave the way towards more quantitative studies of the tunneling time for Landau–Zener transitions, which are of current interest in the context of optimal quantum control [133]. Also, it should be possible to measure the tunneling dynamics in arbitrary bases by inducing a rotation of the 2×2 Landau–Zener matrix through variations in the lattice depth during the transition. With an appropriate choice of this variation one could then, for instance, realize the super-adiabatic basis proposed by M. Berry [112].

In chapter 6, we proposed a new way to control the tunneling probability of ultracold atoms. We presented our new results – yet to be tested in experiments – on the tunneling probability in time-dependent stochastic potentials. To that respect, we studied the impact of different types of colored noise on the tunneling probability. Our results demonstrate that it is possible to engineer the tunneling by adding noise to the system. By changing the noise parameters, the tunneling probability can be enhanced or suppressed. The noise can particularly enhance the tunneling probability when the system parameters are chosen far from the RET condition. More importantly, we calculated analytically an effective model as a benchmark to describe our results in the regime of fast oscillating noise. Furthermore, we found a scaling for our results which turned out to be very useful to reduce the parameter-dependence of the system. This leaded us to a better understanding of noise effects on the tunneling probability. We also introduced a deterministic type of phase given by an oscillating function and study the impact of such a time-dependent phase on the tunneling. This case acts as a further benchmark of generally noise-driven dynamics. All these new predictions await experimental verification.

7.2 Open questions

Many open questions have remained which allow for further studies. During the last three years of our studies, we have tried to understand several observables and problems some of which are not presented in the body of this thesis. For instance, calculating the width Δt of the survival probability step for different initial width Δp of the condensate was one of these results which was published in 2009 in our Physical Review Letter [42]. The idea is: this width can reflect the tunneling time in the Landau–Zener transition [42]. We expanded this study

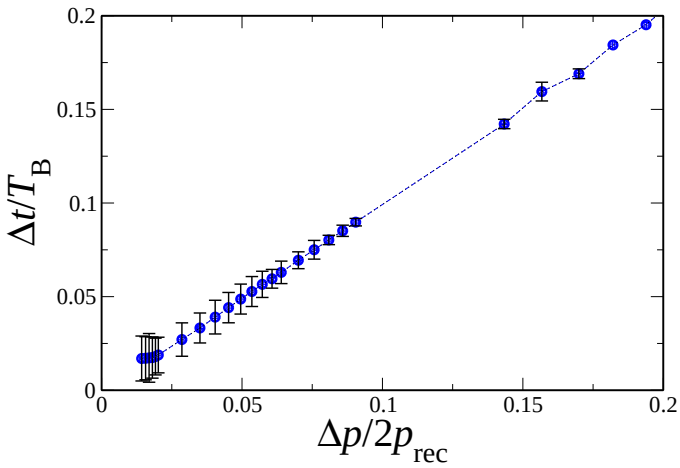

Figure 7.1: The step width Δt for several Δp (filled circles). For $V_0 = 1.5$ and $F_0 = 1.197$. the step width Δt is rescaled by the factor 0.42 which arises from the definition of the error function with respect to our sigmoid function defining Δt according to Eq. (5.11).

numerically to very narrow initial widths of the condensate for different system parameters. Figure 7.1 shows one of the cases for $V_0 = 1.5$ and $F_0 = 1.197$. As one can see, the width of the step saturates for very narrow initial widths of the condensate. However, it turned out the error of our numerical simulations grows by decreasing the initial width and it is become very difficult to extract the width of the step due to the oscillations appearing in the survival probability [43]. This error is of order $(10^{-2}\,T_{\rm B})$ which is crucial in that regime.

Another observable which we studied was time-resolved expansion $\sigma_x(t)$ of the condensate. The time dependence of the condensate width is defined as

$$\sigma_x(t) \equiv \sqrt{\langle (x(t) - \langle x(t)\rangle)^2\rangle}, \tag{7.1}$$

where $\langle x(t)\rangle = \langle \psi(x,t)|x(t)|\psi(x,t)\rangle$ gives the mean position of the wave packet. The measured expansion rate $d\sigma_x(t)/dt$ of the condensate width $\sigma_x(t)$ along with the lattice direction is to a good approximation proportional to the hopping element which effectively describes nearest-neighbor tunneling [134]. Figure 7.2 shows the time evolution of the condensate width $\sigma_x(t)$ for the reference system defined by the Wannier–Stark Hamiltonian and also for the system with the time-dependent potential defined in Eq. (6.2) with $\phi(t)$ given by harmonic noise.

As seen in Figure 7.2, after a few Bloch periods the rate of expansion for the case with $\omega_0 = 30/T_{\rm B}$ (red squares) slows down, while according to our

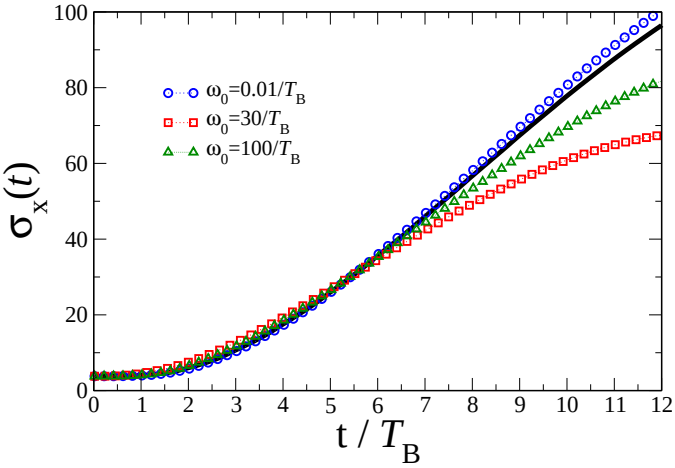

Figure 7.2: The time-resolved expansion of the Bose–Einstein condensate in the time-dependent stochastic potential for $V_0 = 2.5$, $F_0 = 1.5$ and $\phi(t)$ given by harmonic noise with fixed $\Gamma = 1/T_{\rm B}$, $T/\omega_)^2 = 0.25$ and: $\omega_0 = 0.01/T_{\rm B}$ (blue circles), $\omega_0 = 30/T_{\rm B}$ (red squares), and $\omega_0 = 100/T_{\rm B}$ (green triangles) (see Figure 6.10).

results shown in Figure 6.10, for $\omega_0 = 30/T_{\rm B}$ the rate of tunneling is enhanced. For fast noise with $\omega_0 = 100/T_{\rm B}$ (green triangles) the rate of expansion of the condensate is higher and for very slowly varying noise this rate is highest even compared with the reference system's expansion rate. These results are surprising because one expects the condensate to expand more when the tunneling is enhanced. For the periodic system, as explained above it is clear that due to tunnelings the condensate width is increasing and its rate gives a measure for the tunneling rate to the neighboring site [134]. In the noisy system where no band structure can be defined, it is not clear how this function should be analyzed. This is still an open question for further investigations.

Another open question concerning what we presented in this thesis is related to the tunneling probability of the condensate in the presence of exponentially correlated noise explained in section 6.3.3. To describe the results in Figure 6.7, we introduced a scaling which resulted to a universal behavior of the observable $\Gamma_{\rm a}$. But it is not obvious why the decay rate of the survival probability, as seen in Figure 6.7, shows a peak at $\tau/\sqrt{D} \approx 0.3\sqrt{T_{\rm B}}$. Further investigations are needed to explain this resonance-like peak in the decay rate. Finding an analytical estimate to describe the effect of the time-dependent stochastic potential in a very broad range of parameters is desirable.

7.3 Future outlook

Our findings certainly stimulate many further questions and several problems have been left unsolved. Concerning the noisy systems, it is interesting to study the effect of the noise on the Landau–Zener model and calculate how the band-gap is renormalized by the presence of the noise. Some relevant works have been done by V. L. Pokrovsky and his co-workers in [135], where they study the influence of fast noise on Landau-Zener transitions. They also analyze the influence of colored classical Gaussian noise on Landau-Zener transitions during a two-level crossing in a time-dependent regular external field. How such simplified models are connected to our system studied in chapter 6 should be investigated.

Another problem to be considered would be to include the atom-atom interactions in the system. The idea is to investigate the possible interplay between nonlinearity and the time-dependent stochastic potential and their simultaneous impact on the tunneling probability. Some preliminary studies have been done by our Bachelor student, Anton I. Ivanov. His results prove that there is an interplay between interaction and time-dependent disorder. But the effect of nonlinearity is typically very small and more investigations in proper regime of parameters should be performed. V. L. Pokrovsky and his co-workers have done some studies on weakly interacting Bose gas in a random environment [136]. They show that for weak enough interactions, the particles fill deep potential wells of the random potential whose radius and depth depend on the characteristics of the random potential and the interacting gas. A future study investigating these possibilities with ultracold atoms would be very interesting, also in view of new experiments.

Appendix A

Gauge transformation

In section 2.2.4, a Hamiltonian was introduced by Eq. (2.31) which can describe the dynamics of a particle in a driven lattices. This Hamiltonian is equivalent to the Hamiltonian which is constructed by using our disorder potential defined in Eq. (6.10). Here, we demonstrate this equivalence by using unitary transformations as follows The transformation is done in two-steps. Starting from the Hamiltonian given in Eq. (2.31)

$$H_1(x,t) = \frac{p^2}{2M} + V_0 \sin^2(k_L x) + Fx\cos(\omega t), \tag{A.1}$$

with $p = (\hbar/i)d/dx$. This Hamiltonian describes a particle driven by a monochromatic force of frequency ω and strength F that is coupled to the particle in the "length gauge". One can transform the wave functions $\psi_1(x,t)$ which corresponds to $H_1(x,t)$ according to

$$\psi_1(x,t) = e^{-\frac{i}{\hbar}\frac{Fx}{\omega}\sin(\omega t)}\psi_2(x,t). \tag{A.2}$$

Implementing $\psi_1(x,t)$ in the Schroödinger equation $i\hbar\partial_t\psi_1(x,t) = H_1\psi_1(x,t)$, one finds that the dynamics of the new wave functions $\psi_2(x,t)$ are determined by

$$H_2(x,t) = \frac{\left(p - F/\omega\sin(\omega t)\right)^2}{2M} + V_0\sin^2(k_L x). \tag{A.3}$$

This is actually the Hamiltonian which was presented in section 5.1 by Eq. (5.4) and describes the dynamics in the "velocity gauge". In the second step, one has to perform a further transformation [137]. The wave functions $\psi_2(x,t)$ corresponding to $H_2(x,t)$ can be transformed by

$$\begin{aligned}\psi_2(x,t) &= e^{-\frac{i}{\hbar}\int_0^t dt'\left(\frac{Fp}{M\omega}\sin(\omega t') + \frac{F^2}{2M\omega^2}\sin^2(\omega t')\right)}\psi_3(x,t)\\ &= e^{-\frac{i}{\hbar}\frac{Fp}{M\omega^2}\cos(\omega t) + \frac{i}{8\hbar}\frac{F^2}{M\omega^3}\sin(2\omega t)}\psi_3(x,t).\end{aligned} \tag{A.4}$$

In addition $x \to x + F/M\omega^2 \cos(\omega t)$. Therefore, the Hamiltonian to describe the dynamics of this Hamiltonian yields

$$H_3(x,t) = \frac{p^2}{2M} + V_0 \sin^2(k_L(x + F/M\omega^2 \cos(\omega t))) + \frac{F}{4M\omega^2}. \tag{A.5}$$

The term $F/4M\omega^2$ is exactly the "ponderomotive energy" of the particle, i.e., the mean kinetic energy associated with its quiver motion due to the oscillating force. This new Hamiltonian $H_3(x,t)$ with its oscillating potential describes the dynamics in the Kramers–Henneberger frame [138]. Our Hamiltonian in section 3.2.3, which described the dynamics of a particle in a periodic lattice with a deterministic time-dependent phase, is similar to this latter Hamiltonian $H_3(x,t)$.

Bibliography

[1] M. Razavy, Quantum Theory of Tunneling, World Scientific, Singapore (2003).

[2] L. S. Schulman, Lect. Notes Phys. **72**, 99 (2002); ibid. **734**, 107 (2007).

[3] L. D. Landau, Phys. Z. Sowjetunion **2**, 46 (1932).

[4] C. Zener, Proc. R. Soc. A **137**, 696 (1932).

[5] E. C. G. Stückelberg, Helv. Phys. Acta **5**, 369 (1932).

[6] E. Majorana, Nuovo Cimento **9**, 43 (1932).

[7] J. R. Rubbmark M. M. Kash, M. G. Littman, and D. Kleppner, Phys. Rev. A **23**, 3107 (1981).

[8] W. Wernsdorfer and R. Sessoli, Science **284**, 133 (1999).

[9] A. Sibille, J. F. Palmier, and F. Laruelle, Phys. Rev. Lett. **80**, 4506 (1998).

[10] K. Mullen, E. Ben-Jacob, and Z. Schuss, Phys. Rev. Lett. **60**, 1097 (1988); K. Mullen, Y. Gefen and E. Ben-Jacob, Physica B **152**, 172 (1988).

[11] W. D. Oliver, Y. Yu, J. C. Lee, K. K. Berggren, L. S. Levitov and T. P. Orlando, Science **310**, 1653 (2005).

[12] R. Khomeriki and S. Ruffo, Phys. Rev. Lett. **94**, 113904 (2005).

[13] S. Longhi, J. Opt. B: Quantum Semiclassical Opt. **7**, L9 (2005).

[14] F. Dreisow, A. Szameit, M. Heinrich, S. Nolte1, and A. Tünnermann, Phys. Rev. A **79**, 055802 (2009).

[15] Y. Chen, S. D. Huber, S. Trotzky, I. Bloch, and E. Altman, Nature **1801**, 1 (2010).

[16] L. A. Khalfin, Sov. Phys. JETP **6**, 1053 (1958); R. G. Winter, Phys. Rev. **123**, 1503 (1961).

[17] S. R. Wilkinson, C. F. Bharucha, M. C. Fischer, K. W. Madison, P. R. Morrow, Q. Niu, B. Sundaram, and M. G. Raizen, Nature (London) **387**, 575 (1997); see also P. T. Greenland, Nature (London) **387**, 548 (1997).

[18] G.E. Santoro, R. Martoňák, E. Tosatti, and R. Car, Science **295**, 2427 (2002).

[19] K. Leo, P. H. Bolivar, F. Brüggemann, R. Schwedler, and K. Köhler, Solid State Comm. **84**, 943 (1992); C. Waschke, H. G. Roskos, R. Schwedler, K. Leo, H. Kurz, and K. Köhler, Phys. Rev. Lett. **70**, 3319 (1993).

[20] J. Feldmann, K. Leo, J. Shah, D. Miller, J. Cunningham, T. Meier, G. von Plessen, A. Schulze, P. Thomas, and S. Schmitt-Rink, Phys. Rev. B **46**, 7252 (1992).

[21] M. Ben Dahan, E. Peik, J. Reichel, Y. Castin, and C. Salomon, Phys. Rev. Lett. **76**, 4508 (1996).

[22] C. F. Bharucha, K. W. Madison, P. R. Morrow, S. R. Wilkinson, B. Sundaram, and M. G. Raizen, Phys. Rev. A **55**, R857 (1997); K. W. Madison, C. F. Bharucha, P. R. Morrow, S. R. Wilkinson, Q. Niu, B. Sundaram, and M. G. Raizen, Appl. Phys. B: Lasers Opt. **B65**, 693 (1997).

[23] B. Anderson and M. Kasevich, Science **282**, 1686 (1998).

[24] N. V. Vitanov and B. M. Garraway, Phys. Rev. A **53**, 4288 (1996); ibid. **54**, 5458(E) (1996).

[25] M. Glück, A. R. Kolovsky and H. J. Korsch, Phys. Rep. **366**, 103 (2002).

[26] J. R. Anglin and W. Ketterle, Nature **416**, 211 (2002).

[27] O. Morsch, M. Oberthaler, Rev. Mod. Phys. **78**, 179 (2006).

[28] R. P. Feynman, Int. J. Theor. Phys. **21**, 467 (1982).

[29] T. Schulte, S. Drenkelforth, G. Kleine Büning, W. Ertmer, J. Arlt, M. Lewenstein, and L. Santos, Phys. Rev. A **77**, 023610 (2008).

[30] T. Salger. S. Kling, T. Hecking, C. Geckeler, L. Morales-Molina, M. Weitz, Science **326**, 1241 (2009).

[31] J. Billy, V. Josse, Z. Zuo, A. Bernard, B. Hambrecht, P. Lugan, D. Clément, L. Sanchez-Palencia, P. Bouyer, and A. Aspect, Nature **453**, 891 (2008); G. Roati, C. DErrico, L. Fallani, M. Fattori, C. Fort, M. Zaccanti, G. Modugno, M. Modugno, and M. Inguscio, Nature **453**, 895 (2008).

[32] R. T. Scalettar, G. G. Batrouni, and G. T. Zimanyi, Phys. Rev. Lett. **66**, 3144 (1991).

[33] R. Fallani,J. E. Lye, V. Guarrera, C. Fort, and M. Inguscio, Phys. Rev. Lett. **98**, 130404 (2007).

[34] G. Roux, T. Barthel, I. P. McCulloch, C. Kollath, U. Schollwöck, and T. Giamarchi, Phys. Rev. A **78**, 023628 (2008).

[35] O. Morsch, J. H. Müller, M. Cristiani, D. Ciampini, and E. Arimondo, Phys. Rev. Lett. **87**, 140402 (2001).

[36] S. Wimberger, R. Mannella, O. Morsch, E. Arimondo, A. R. Kolovsky, and A. Buchleitner, Phys. Rev. A **72**, 063610 (2005).

[37] C. Sias, A. Zenesini, H. Lignier, S. Wimberger, D. Ciampini, O. Morsch, and E. Arimondo, Phys. Rev. Lett **98**, 120403 (2007).

[38] A. Zenesini, C. Sias, H. Lignier, Y. Singh, D. Ciampini, O. Morsch, R. Mannella, E. Arimondo, A. Tomadin and S. Wimberger, New J. Phys. **10**, 053038 (2008).

[39] D. I. Choi and Q. Niu, Phys. Rev. Lett. **82**, 2022 (1999).

[40] N. V. Vitanov, Phys. Rev. A **59**, 988 (1999).

[41] M. Holthaus, J. Opt. B: Quantum Semiclassical Opt. **2**, 589 (2000).

[42] A. Zenesini, H. Lignier, G. Tayebirad,J. Radogostowicz, D. Ciampini, R. Mannella, S. Wimberger, O. Morsch, and E. Arimondo, Phys. Rev. Lett **103**, 090403 (2009).

[43] G. Tayebirad, A. Zenesini, D. Ciampini, R. Mannella, O. Morsch, E. Arimondo, N. Lörch, and S. Wimberger, Phys. Rev. A **82**, 013633 (2010).

[44] G. Tayebirad, R. Mannella, S. Wimberger, arXiv:1010.1671, submitted in Appl. Phys. B (2010).

[45] S. N. Bose, Z. Phys. **26**, 178 (1924).

[46] A. Einstein, Sitzungsberichte der Preussischen Akademie der Wissenschaften, Physikalisch-mathematische Klasse p. 261 (1924); p. 3 (1925).

[47] M. H. Anderson, J. R. Ensher, M. R. Matthews, C. E. Wieman, and E. A. Cornell, Science **269**, 198 (1995).

[48] K. B. Davis, M.-O. Mewes, M. R. Andrews, N. J. van Druten, D. S. Durfee, D. M. Kurn, and W. Ketterle, Phys. Rev. Lett. **75**, 3969 (1995).

[49] C. C. Bradley, C. A. Sackett, J. J. Tollett, and R. G. Hulet, Phys. Rev. Lett. **75**, 1687 (1995); C. C. Bradley, C. A. Sackett, and R. G. Hulet, Phys. Rev. Lett. **78**, 985 (1997).

[50] C. J. Pethick and H. Smith, BoseEinstein Condensation in Dilute Gases, Cambridge University Press, Cambridge, (2001).

[51] H. Feshbach, Ann. Phys. **5**, 357 (1958).

[52] E. P. Gross, Nuovo. Cimento. **20**, 454 (1961); L. P. Pitaevskii, Zh. Eksp. Teor. Fiz. **40**, 646 (1961); Sov. Phys. JETP **13**, 451 (1961).

[53] L. D. Carr, Charles W. Clark, and W. P. Reinhardt, Phys. Rev. A, **62**, 063610 (2000).

[54] F. Dalfovo, C. Minniti, S. Stringari, and L. Pitaevskii, Phys. Lett. A **227**, 259 (1997).

[55] P. Lebedev, Ann. Phys. **32**, 411 (1910); O. Frish, Z. Phys. **88**, 42 (1933).

[56] A. F. Bernhardt, D. E. Duerre, J. R. Simpson, and L. L. Wood, Appl. Phys. Lett. **25**, 617 (1974); E. Arimondo, H. Lew, and T. Oka, Phys. Rev. Lett. **43**, 753 (1979).

[57] J. E. Bjorkholm, R. E. Freeman, A. Ashkin, and D. B. Pearson, Phys. Rev. Lett. **41**, 1361 (1978); Steven Chu, J.E. Bjorkholm, A. Ashkin, and A. Cable, Phys. Rev. Lett. **57** 314, (1986).

[58] P. C. M. Planken, M. C. Nuss, I. Brener, K. W. Goossen, M. S. C. Luo, S. Lien Chuang and Loren Pfeiffer, Phys. Rev. Lett. **69**, 3800 (1992).

[59] E. E. Mendez, G. Bastard, Phys. Today **46**, 34 (1993).

[60] M. Greiner, O. Mandel, T. Esslinger, T. W. Hänsch, and I. Bloch, Nature **415**, 39 (2002); ibid, **419**, 51 (2002).

[61] I. Bloch, Nature, **1**, 23 (2005).

[62] C. Cohen-Tannoudji, J. Dupont-Roc, G. Grynberg, Atom-Photon Interactions, Wiley and Sons, New York, **206**, 209 (1992).

[63] M. C. Fischer, M. G. Raizen, Lect. Notes Phys. **789**, 205 (2009).

[64] R. Graham, M. Schlautmann, P. Zoller, Phys. Rev. A **45**, R19 (1992).

[65] R. Grimm, M. Weidemüller, and Y. B. Ovchinnikov, Advances in Atomic, Molecular and Optic Physics, **42**, 95, (2000).

[66] Y. Nagaoka and H. Fukuyama (ed), Anderson Localization, Springer Series in Solid State Sciences **39**, (1982); T. Ando and H. Fukuyama (ed), Anderson Localization, Springer Proceedings in Physics **28**, (1988).

[67] P. W. Anderson, Phys. Rev. **109**, 1492 (1958).

[68] P. Horak, J-Y. Courtois and G. Grynberg, Phys. Rev. A **58** 3953 (1998); G. Grynberg, P. Horak and C. Mennerat-Robilliard, Eur. phys. Lett. **49**, 424 (2000).

[69] J. E. Lye, L. Fallani, M. Modugno, D. Wiersma, C. Fort, and M. Inguscio Phys. Rev. Lett. **95**, 070401 (2005).

[70] R. Roth and K. Burnett, J. Opt. B: Quantum Semiclass. Opt. **5**, S50 (2003).

[71] B. Damski, J. Zakrzewski, L. Santos, P. Zoller, and M. Lewenstein, Phys. Rev. Lett. **91**, 080403 (2003).

[72] U. Gavish and Y. Castin, Phys. Rev. Lett. **95**, 020401 (2005).

[73] H. Gimperlein, S. Wessel, J. Schmiedmayer, and L. Santos, Phys. Rev. Lett. **95**, 170401 (2005).

[74] L. Guidoni, C. Triché, P. Verkerk, and G. Grynberg, Phys. Rev. Lett. **79**, 3363 (1997); L. Guidoni and P. Verkerk, Phys. Rev. A **57**, R1501 (1998).

[75] L. Sanchez-Palencia and L. Santos, Phys. Rev. A **72**, 053607 (2005).

[76] N. F. Mott and W. D. Twose, Adv. Phys. **10**, 107 (1961); N.F. Mott, Rev. Mod. Phys. **40**, 677 (1968).

[77] R. E. Borland, Proc. R. Soc. London Ser. A **274**, 529 (1963).

[78] S. Drenkelforth, G. Kleine Büning, J. Will, T. Schulte, N. Murray, W. Ertmer, L. Santos, and J. J. Arlt, New J. Phys. **10**, 045027 (2008).

[79] S. Kraft A. Güther, H. Ott, D. Wharam, C. Zimmermann, and J. Fortágh, J. Phys. B **35**, L469 (2002); A. E. Leanhardt, Y. Shin, A. P. Chikkatur, D. Kielpinski, W. Ketterle, and D. E. Pritchard, Phys. Rev. Lett. **90**, 100404 (2003); J. Estève, C. Aussibal, T. Schumm, C. Figl, D. Mailly, I. Bouchoule, C. I. Westbrook, and A. Aspect, Phys. Rev. A **70**, 043629 (2004); D. W. Wang, M. D. Lukin, and E. Demler, Phys. Rev. Lett. **92**, 076802 (2004).

[80] J. Fortágh, H. Ott, S. Kraft, A. Gnther, and C. Zimmermann, Phys. Rev. A **66**, 041604(R) (2002).

[81] S. Aubry and G. André, Ann. Israel Phys. Soc. **3**, 133 (1980).

[82] F. Gerbier, A. Widera, S. Fölling, O. Mandel, T. Gericke, and I. Bloch, Phys. Rev. A **72**, 053606 (2005).

[83] F. Grossmann, T. Dittrich, P. Jung, and P. Hänggi, Phys. Rev. Lett. **67**, 516 (1991).

[84] O. Morsch, D. Ciampini and E. Arimondo, Europhys. News **41**, 21 (2010).

[85] F. Bloch, Zeitschrift für Physik, **52**, 555 (1928).

[86] C. Zener, Proc. Roy. Soc. London Ser., **145**, 523 (1934).

[87] L. Esaki, R. Tsu, IBM J. of Research and Development, **14**, 61 (1970).

[88] C. Bersch, G. Onishchukuv, U. Peschel, Opt. Lett. **34**, 2372 (2009).

[89] S. Longhi, Phys. Rev. B **81**, 195118 (2010).

[90] G. H. Wannier, Phys. Rev. **117**, 432 (1960); Rev. Mod. Phys. **34**, 645 (1962).

[91] T. Hartmann, F. Keck, H. J. Korsch, S. Mossmann, New J. Phys. **6**, 2 (2004).

[92] G. H. Wannier, Phys. Rev. **117**, 432 (1960); Rev. Mod. Phys. **34**, 645 (1962); Phys. Rev. **181**, 1364 (1969).

[93] J. E. Avron, J. Zak, A. Grossmann, and L. Gunther, J. Math. Phys. **18**, 918 (1977).

[94] J. B. Krieger and G. J. Iafrate, Phys. Rev. B **33**, 5494 (1986); ibid., **38**, 6324 (1988).

[95] G. Nenciu, Rev. Mod. Phys. **63**, 91 (1991).

[96] M. Luban, A. Bouchard, Phys. Rev. B **47**, 6815 (1993).

[97] P. Voisin, J. Bleuse, C. Bouche, S. Gaillard, C. Alibert, and A. Regreny, Phys. Rev. Lett. **61**, 1639 (1988); E. E. Mendez, F. Agull-Rueda, and J. M. Hong, Phys. Rev. Lett. **60**, 2426 (1988) .

[98] M. Glück, A. R. Kolovsky, and H. J. Korsch, Phys. Rev. Lett. **83**, 891 (1999).

[99] N. Moiseyev and H. J. Korsch, Phys. Rev. A **41**, 498 (1990); M. Glück, A. R. Kolovsky, H. J. Korsch, and N. Moiseyev, Eur. Phys. J. D **4**, 239 (1998).

[100] S. Glutsch and F. Bechstedt, Phys. Rev. B **60**, 16 584 (1999).

[101] M. Glück, A. R. Kolovsky, and H. J. Korsch, Phys. Rev. Lett. **83**, 891 (1999).

[102] B. Rosam, D. Meinhold, F. Löser, V. G. Lyssenko, S. Glutsch, F. Bechstedt, F. Rossi, K. Köhler, and K. Leo, Phys. Rev. Lett. **86**, 1307 (2001).

[103] H. Schneider, H. T. Grahn, K. v. Klitzing, and K. Ploog, Phys. Rev. Lett. **65**, 2720 (1990).

[104] R. Till, H. Kümmel, A. Philipp, G. Böhm, and G. Weimann, Superlattices Microstruct. **24**, 227 (1998).

[105] S. R. Wilkinson, C. F. Bharucha, K. W. Madison, Qian Niu, and M. G. Raizen, Phys. Rev. Lett **76**, 4512 (1996).

[106] M. Cristiani, O. Morsch, J. H. Müller, D. Ciampini, and E. Arimondo, Phys. Rev. A **65**, 063612 (2002).

[107] B. Wu and Q. Niu, Phys. Rev. A **61**, 023402 (2000); J. Liu, L. Fu, B. Qu, S. Chen, D. Choi, B Wu, and Q. Niu, ibid. **66**, 023404 (2002).

[108] O. Zobay and B. M. Garraway, Phys. Rev. A **61**, 033603 (2000).

[109] A. Sibille, J.F. Palmier, and F. Laruelle, Phys. Rev. Lett. **80**, 4506 (1998).

[110] A. V. Shytov, D. A. Ivanov and M. V. Feigelman, Eur. J. Phys. B **36**, 263 (2003); M. D. LaHaye, J. Suh, P. M. Echternach, K. C. Schwab, and M. L. Roukes, Nature **459**, 960 (2009).

[111] D. M. Berns, M. S. Rudner, S. O. Valenzuela, K. K. Berggren, W. D. Oliver, L. S. Levitov and T. P. Orlando, Nature (London) **455**, 51 (2008).

[112] M. V. Berry, Proc. R. Soc. A, **429**, 61 (1990); R. Lim and M. V. Berry, J. Phys. A **24**, 3255 (1991).

[113] R. Mannella, A gentle introduction to the integration of stochastic differential equations, Lecture Notes in Physics, **557**, Springer, Heidelberg (2000).

[114] A. Einstein, Ann. Phys. **17**, 549 (1905).

[115] M. von Smoluchowski, Ann. Phys. **21**, 756 (1906).

[116] N. G. Van Kampen, Stochastic Processes in Physics and Chemistry, revised and enlarged edition, North-Holland, Amsterdam (1992); R. F. Fox, Phys. Rep. **48**, 179 (1978).

[117] H. Grabert, P. Talkner, and P. Hänggi, Z. Phys. B **26**, 389 (1977); P. Hänggi, Phys. Lett. A **83**, 196 (1981); P. Hänggi, T. J. Mroczkowski, F. Moss, and P. V. E. McClintock, Phys. Rev. A **32**, 695 (1985); P. Hänggi, and P. Jung, Adv. Chem. Phys. **89**, 239 (1995).

[118] G. E. Uhlenbeck and L. S. Ornstein, Phys. Rev. **36**, 823 (1930).

[119] L. Schimansky-Geier and Ch. Zülicke. Z. Phys. B **79**, 452 (1990).

[120] S. Chandrasekhar, Rev. Mod. Physics **15**, 1 (1943).

[121] M. C. Wang, G. Uhlenbeck, Rev. Mod. Phys. **17**, 323 (1945).

[122] J. Masoliver, L. Garrido, and J. Llosa, J. Stat. Phys., **46**, 233 (1987).

[123] H. Nyquist, Trans. AIEE, **47**, 617 (1928); C. E. Shannon, Proc. Institute of Radio Engineers, **37**, 10 (1949).

[124] W. H. Press, S. A. Teukolsky, W. T. Vetterling und B. P. Flannery, Numerical Recipes, Cambridge University Press, Cambridge (2002).

[125] W. A. Ames, Numerical Methods for Partial Differential Equation, Academic Press, New York (1977).

[126] M. L. Chiofalo, S. Succi, und M. P. Tosi, Phys. Rev. E **62**, 7438 (2000).

[127] E. Cerboneschi, R. Manella, E. Arimondo und L. Salasnich, Phys. Lett. A **249**, 495 (1998).

[128] M. Jona-Lasinio, O. Morsch, M. Cristiani, N. Malossi, J. H. Mller, E. Courtade, M. Anderlini, and E. Arimondo, Phys. Rev. Lett. **91**, 230406 (2003); ibid. **93**, 119903(E) (2004).

[129] S. Wimberger, P. Schlagheck, and R. Mannella, J. Phys. B: At. Mol. Opt. Phys. **39**, 729 (2006).

[130] G. Roati, E. de Mirandes, F. Ferlaino, H. Ott, G. Modugno, and M. Inguscio, Phys. Rev. Lett. **92**, 230402 (2004).

[131] M. Gustavsson, E. Haller, M. J. Mark, J. G. Danzl, G. Rojas-Kopeinig, and H.-C. Nägerl, Phys. Rev. Lett. **100**, 080404 (2008).

[132] M. Modugno, C. Tozzo, and F. Dalfovo, Phys. Rev. A **70**, 043625 (2004).

[133] V. Giovannetti, S. Lloyd, and L. Maccone, Phys. Rev. A **67**, 052109 (2003); M. Sillanpää, T. Lehtinen, A. Paila, Y. Makhlin, and P. Hakonen, Phys. Rev. Lett. **96**, 187002 (2006); T. Caneva, M. Murphy, T. Calarco, R. Fazio, S. Montangero, V. Giovannetti, and G. E. Santoro, ibid. **103**, 240501 (2009).

[134] H. Lignier, C. Sias, D. Ciampini, Y. Singh, A. Zenesini, O. Morsch, and E. Arimondo, Phys. Rev. Lett. **99**, 220403 (2007).

[135] V. L. Pokrovsky and N. A. Sinitsyn, Phys. Rev. B **67**, 144303 (2003); V. L. Pokrovsky, and S. Scheidl, ibid. **70**, 014416 (2004); V. L. Pokrovsky and D. Sun, ibid. **76**, 024310 (2007).

[136] G. M. Falco, T. Nattermann, and V. L. Pokrovsky, Phys. Rev. B **80**, 104515 (2009).

[137] M. Gavrila, in Coliision Theory for Atoms and Molecules, NATO ASI Series B, edited by F. A. Gianturco, **196**, 139, Plenum Press, New York (1989).

[138] W. C. Henneberger, Phys. Rev. Lett. **21**, 838 (1968).